

ULTRAFAST PROTEIN DYNAMICS IN AQUEOUS AND CONFINED
ENVIRONMENTS PROBED BY 2D-IR SPECTROSCOPY

A DISSERTATION

SUBMITTED TO THE DEPARTMENT OF CHEMISTRY

AND THE COMMITTEE ON GRADUATE STUDIES

OF STANFORD UNIVERSITY

IN PARTIAL FULFILLMENT OF THE REQUIREMENTS FOR THE DEGREE OF

DOCTOR OF PHILOSOPHY

Ilya Joseph Finkelstein

January 2007

UMI Number: 3253481

INFORMATION TO USERS

The quality of this reproduction is dependent upon the quality of the copy submitted. Broken or indistinct print, colored or poor quality illustrations and photographs, print bleed-through, substandard margins, and improper alignment can adversely affect reproduction.

In the unlikely event that the author did not send a complete manuscript and there are missing pages, these will be noted. Also, if unauthorized copyright material had to be removed, a note will indicate the deletion.

UMI[®]

UMI Microform 3253481

Copyright 2007 by ProQuest Information and Learning Company.

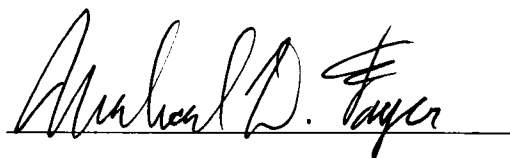
All rights reserved. This microform edition is protected against unauthorized copying under Title 17, United States Code.

ProQuest Information and Learning Company
300 North Zeeb Road
P.O. Box 1346
Ann Arbor, MI 48106-1346

© Copyright by Ilya Joseph Finkelstein 2007

All Rights Reserved

I certify that I have read this dissertation and that in my opinion it is fully adequate, in scope and quality, as dissertation for the degree of Doctor of Philosophy.

A handwritten signature in black ink, appearing to read "Michael D. Fayer", written over a horizontal line.

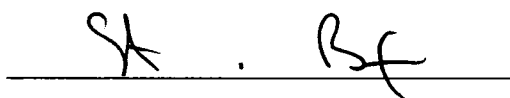
(Michael D. Fayer) Principal Advisor

I certify that I have read this dissertation and that in my opinion it is fully adequate, in scope and quality, as dissertation for the degree of Doctor of Philosophy.

A handwritten signature in black ink, appearing to read "Vijay S. Pande", written over a horizontal line.

(Vijay S. Pande)

I certify that I have read this dissertation and that in my opinion it is fully adequate, in scope and quality, as dissertation for the degree of Doctor of Philosophy.

A handwritten signature in black ink, appearing to read "Steven G. Boxer", written over a horizontal line.

(Steven G. Boxer)

Approved for the University Committee on Graduate Studies

ABSTRACT

Protein structural fluctuations play a pivotal role in biological function, but have remained largely unexamined on the fastest timescales in thermal equilibrium. In this work, ultrafast 2D-IR vibrational echo methods are developed and used to study the dynamics of several proteins in both aqueous and confined environments, as well as when bound to small organic molecule substrates. 2D-IR spectroscopy is capable of accessing protein fluctuations on timescales ~ 6 -10 orders of magnitude faster than 2D NMR. In addition, the relatively low energy mid-IR laser pulses used in this study probe the relevant nuclear degrees of freedom without significantly perturbing the protein structure or dynamics.

The vibrational dynamics of carbon monoxide (CO) bound to the active site of both myoglobin (MbCO) and a distal histidine mutant are examined via 2D-IR experiments and molecular dynamics (MD) simulations. A quantitative model for coupling experimental observables and classical simulations is presented. The complimentary spectroscopic experiments and molecular simulations are used to examine the contributions of key residues to the overall structural fluctuations, as sensed by the CO. Studies on several mutants of cytochrome c_{552} reveal that the 2D-IR method is sensitive to minute changes in the hydrogen bonding network of the protein active site.

Nature has learned to function in a crowded intracellular environment. To probe the effect of molecular confinement on protein fluctuations, 2D-IR experiments were used to interrogate the dynamics of several heme proteins in a room temperature sugar glass, as a function of viscosity, and in nanoscopic water pools. In addition, the dynamics of hemoglobin in human erythrocytes were examined. MD simulations were employed to gain an atomic level picture of how confinement affects protein structural fluctuations. It was found that proteins retain significant mobility even when confined in a glass at room temperature. Studies on protein encapsulated in

nanoscopic sol-gel water pools revealed that only a few hydration layers of water are necessary to reactivate the unconfined dynamics.

Enzyme structural fluctuations play a pivotal role in substrate binding and biological function. The dynamics of horseradish peroxidase (HRP) in the free form and when ligated to a variety of small organic molecule substrates was studied using 2D-IR vibrational echo spectroscopy. Carbon monoxide bound at the heme active site of HRP serves as a spectroscopic marker that is sensitive to the structural dynamics of the protein. In the free form, HRP assumes two distinct spectroscopic conformations that undergo fluctuations on the tens of picoseconds timescale. Upon substrate binding, HRP is locked into a single conformation that exhibits reduced amplitudes and slower timescale dynamics. The decrease in structural fluctuations is attributed to reduced dynamic freedom of the distal histidine and the distal arginine, which are key residues in modulating substrate binding affinity. It is suggested that dynamic quenching caused by substrate binding can cause the protein to become locked into a conformation suitable for downstream steps in the enzymatic cycle of HRP.

ACKNOWLEDGMENTS

Nature and Nature's laws lay hid in night,
God said: "Let Newton be!", and all was light.

— *Alexander Pope*

The journey towards obtaining a Ph. D. can be a daunting and challenging, but ultimately a rewarding enterprise. Throughout my tenure at Stanford, I have benefited immensely from interactions with colleagues, peers, and friends too numerous to list individually. I conclude my studies here in full confidence that the connections, both scientific and social, that I have made over these last years will remain with me forever. It is difficult to imagine a place that is better suited for pursuing a graduate education than Stanford University.

Michael Fayer, my scientific advisor and mentor, took me in as a young and green graduate student. His unflagging enthusiasm for science and unmatched experimental knowledge has made coming to lab a fun and fruitful activity. Under Mike's tutelage, I learned to be an engineer, programmer, plumber, electrician, and ultimately, a strong physical chemist.

I am also indebted to several key individuals that helped me develop throughout my scientific tenure in the Fayer Lab. David Thompson and Kusai Merchant taught me how to handle the lasers with finesse. Brian McClain and Aaron Massari were my excellent co-workers who helped shape my scientific thinking and made the science fun. Ivan Piletic, Alexei Goun, Jie Li, Hu Cang, and the rest of Fayer lab informed and invigorated much of my work here. The newest generations of the lab will continue our cohesive and exciting scientific atmosphere.

None of this work could have ever come to fruition without the blessing of my wonderful family. Mom and Dad, thanks for supporting my bid to become a doctor,

albeit a "fake" one. Your love and encouragement have given me the strength to pursue my interests, no matter how useless they may be! Henry, you're the best brother I could have ever hoped for. Thanks for sticking around and reminding me every so often to stop being all grown up.

Boris and Zina, thank you for sheltering yet another homeless Ph. D. these last few months. The warmth of your hearth and hearts helped me remain sane as the deadlines loomed. Alex, thanks for talking me through that roller coaster we call academia from my first undergraduate classes to my first grants and beyond. Paul, without you I'd never make it out to that little festival in the desert and I know that a little bit of your mellow attitude has rubbed off on me.

The best reward of my graduate career was to meet my greatest love and source of inspiration, Julie Sarah Glasser. The trials and tribulations of my time at Stanford pale in comparison to the joy of meeting you. For years, your companionship has illuminated every aspect of my life. All of those rough patches seem surmountable when we approach them together. We make the best team I could imagine.

So Long, and Thanks for All the Fish.

TABLE OF CONTENTS

Abstract	iv
Acknowledgments	vi
Table of Contents	viii
List of Figures	xi
List of Tables	xv
Chapter 1: Introduction	1
1.1 Protein Dynamics	1
1.2 2D-IR Vibrational Echo Spectroscopy.....	3
1.3 References	6
Chapter 2: Experimental Apparatus and Theoretical Formalism	9
2.1 Introduction	9
2.2 Experimental Apparatus.....	10
2.2.1 Generation of Tunable mid-IR Light	10
2.2.2 2D-IR Interferometer	16
2.3 Theoretical Formalism	21
2.4 The 2D-IR Vibrational Echo Experiment	26
2.4.1 A Qualitative Description of the Vibrational Echo	26
2.4.2 Calculation of the 2D-IR Spectra	29
2.5 Transient Grating and Pump-Probe Experiments	34
2.6 References	36
Chapter 3: Aqueous Protein Dynamics	38

3.1	Introduction	38
3.2	Materials and Methods	41
3.2.1	Protein Preparation.....	41
3.2.2	Sample Preparation for Vibrational Echo Spectroscopy.....	41
3.2.3	Molecular Dynamics Simulations of H64V	42
3.2.4	FFCF Extraction From Vibrational Echo Data	43
3.3	Illustration of the Technique – Myoglobin-CO	45
3.3.1	Homodyne Detected Vibrational Echo Spectroscopy.....	45
3.3.2	Heterodyne Detected 2D-IR Echo Spectroscopy	48
3.3.3	The Frequency-Frequency Correlation Function	53
3.4	Dynamics of Myoglobin Without the Distal Histidine	57
3.4.1	Vibrational Echo Spectroscopy.....	57
3.4.2	MD Simulations of the H64V Dynamics.....	61
3.5	Cytochrome c_{552} Active Site Mutants	67
3.5.1	Linear IR spectroscopy	67
3.5.2	Stimulated Vibrational Echo Spectroscopy	69
3.6	Concluding Remarks	76
3.7	References	77
Chapter 4: Dynamics in Confined Environments.....		81
4.1	Introduction	81
4.2	Materials and Methods	84
4.2.1	Preparation of Trehalose Glasses	84
4.2.2	Preparation of Variable Viscosity Fructose Solutions	84
4.2.3	Preparation of Sol-Gel Encapsulated Proteins	85
4.2.4	Preparation of CO-saturated Erythrocytes	86
4.2.5	Determining FFCFs.....	87
4.2.6	Computational Methods	87
4.3	Dynamics in a Trehalose Glass	89
4.3.1	Linear Spectroscopy.....	89

4.3.2	Vibrational Echo Spectroscopy in a Trehalose Glass	91
4.3.3	MD Simulations of H64V in Glassy Water Solvents.....	99
4.4	Viscosity Dependent Protein Dynamics.....	108
4.4.1	Linear and Stimulated Vibrational Echo Spectroscopy	108
4.4.2	Viscoelastic Model.....	114
4.5	Dynamics in a Nanoscopic Water Pool.....	124
4.5.1	Vibrational Echo Experiments	124
4.6	Hemoglobin in Human Erythrocytes	133
4.6.1	Strategy for Removing Scattered Light.....	134
4.6.2	Hemoglobin Dynamics in an Erythrocyte.....	136
4.7	Concluding Remarks	140
4.8	References	142
Chapter 5: Protein-Substrate Interactions.....		147
5.1	Introduction	147
5.2	Materials and Methods	149
5.3	Dynamics of HRP in the free and substrate-bound states	149
5.3.1	Linear Spectra	149
5.3.2	2D-IR Spectroscopy	152
5.3.3	Underlying Protein Dynamics.....	156
5.4	Concluding Remarks	161
5.5	References	162

LIST OF FIGURES

Figure 2.1 A block diagram of the laser system.....	10
Figure 2.2 Ray-trace schematic of stretcher operation.....	12
Figure 2.3 A schematic of the regenerative amplifier laser cavity.....	13
Figure 2.4 Ray-trace diagram of a pulse compressor.....	15
Figure 2.5 A schematic of the experimental geometry	17
Figure 2.6 A simplifier schematic of the 2D-IR interferometer.....	18
Figure 2.7 A diagram depicting the changes that occur to an isolated harmonic oscillator upon immersion in a dynamic bath	24
Figure 2.8 A depiction of the interdependence between frequency fluctuations and the frequency-frequency correlation function.....	26
Figure 2.9 A schematic of the pump-probe setup	35
Figure 3.1 The x-ray crystal structure of MbCO.....	39
Figure 3.2 The active site structures of <i>Ht</i> -cyt <i>c</i> ₅₅₂ mutants M61A/Q64N and M61A, as determined by 2D NMR	41
Figure 3.3 The FT-IR absorption spectrum of wild type MbCO	45
Figure 3.4 Homodyne detected 2D-IR vibrational spectra of wild type MbCO	47
Figure 3.5 An illustration of the heterodyne detected 2D-IR spectrum	49
Figure 3.6 A series of 2D-IR spectra for MbCO as a function of increasing T_w	51
Figure 3.7 Normalized diagonal slice through the 2D-IR data for MbCO	53
Figure 3.8 A schematic illustration of the dynamic Stark effect.....	55
Figure 3.9 The time dependent Stark frequency shift taken from a segment of an MD simulation of MbCO	56
Figure 3.10 The linear absorption spectrum of the CO stretch of H64V	57
Figure 3.11 The vibrational echo decay curves of H64V	58
Figure 3.12 The 2D-IR echo decay curves of H64V compared to MbCO	59
Figure 3.13 A comparison of the experimental H64V data and a fit	60

Figure 3.14 A comparison of the measured and simulated linear and vibrational echo decays for H64V	61
Figure 3.15 A comparison of the vibrational echo peak shifts from experiment and MD simulations for H64V	63
Figure 3.16 A decomposition of the FFCF calculated from an MD simulation of H64V	65
Figure 3.17 Normalized FT-IR spectra of the CO stretching mode bound to <i>Ht</i> -M61A and <i>Ht</i> -M61A/Q64N.....	69
Figure 3.18 Spectrally-resolved vibrational echo decays for <i>Ht</i> -M61A and <i>Ht</i> -M61A/Q64N	70
Figure 3.19 Vibrational echo peak shifts as a function of T_w for <i>Ht</i> -M61A and <i>Ht</i> -M61A/Q64N	71
Figure 3.20 Comparison of the spectroscopic observables and best fit for <i>Ht</i> -M61A	72
Figure 3.21 A comparison of the vibrational echo decays for the three states of MbCO.....	74
Figure 4.1 Scanning electron micrograph images of an active and anhydrobiotic water bear (tardigrade)	82
Figure 4.2 Normalized FT-IR spectra for H64V, <i>Ht</i> -M61A, and HbCO in aqueous and glassy trehalose environments.....	90
Figure 4.3 Vibrational echo decays for H64V, <i>Ht</i> -M61A, and HbCO in aqueous and glassy trehalose environments.....	92
Figure 4.4 Spectral diffusion as a function of T_w for H64V in aqueous solution and in a trehalose glass.....	95
Figure 4.5 Comparison of experimental data and best fit for H64V in trehalose	96
Figure 4.6 Comparison of normalized FFCFs extracted from measured vibrational echo data for H64V, <i>Ht</i> -M61A, and HbCO	97
Figure 4.7 $C(t)$ calculated from MD simulations of H64V in dynamic and static water	100

Figure 4.8 $C_{ii}(t)$ for several shells computed from a simulation of H64V	103
Figure 4.9 Contribution to the total frequency fluctuations of the different shells for H64V	104
Figure 4.10 The cross-correlation functions of the contributions to the fluctuating CO frequency of several shells in H64V.....	106
Figure 4.11 Viscosity dependent FT-IR spectra of four heme proteins.....	108
Figure 4.12 Echo decays as a function of viscosity for H64V.....	110
Figure 4.13 The vibrational echo peak shift as a function of T_w for H64V	113
Figure 4.14 The vibrational echo peak shift as a function of viscosity for several proteins.....	114
Figure 4.15 Logarithmic plot of the reduced correlation time as a function of viscosity measured for the A_1 state of MbCO.....	119
Figure 4.16 Logarithmic plots of the reduced correlation time for M61A, HbCO and H64V	120
Figure 4.17 The viscosity dependent contribution to the FFCF for HbCO, H64V, and M61A.....	123
Figure 4.18 Vibrational echo decays for aqueous and sol-gel encapsulated MbCO ..	126
Figure 4.19 Vibrational echo decays for aqueous and sol-gel encapsulated HbCO ..	127
Figure 4.20 Vibrational echo peak shifts as a function of T_w for MbCO and HbCO in aqueous and sol-gel encapsulated environments.....	128
Figure 4.21 A comparison of high viscosity aqueous and sol-gel encapsulated dynamics in MbCO	130
Figure 4.22 Vibrational echo decays from HbCO in erythrocytes.....	135
Figure 4.23 Extrapolation of the approximate viscosity found in human red blood cells	137
Figure 4.24 Vibrational echo decays of aqueous HbCO and intracellular HbCO	139
Figure 5.1 FT-IR spectra of HRP in the free form and when complexed to several small molecule effectors	150
Figure 5.2 Crystal structure of the active site of free HRP	152

Figure 5.3 2D-IR spectra of free HRP as a function of increasing T_w	153
Figure 5.4 T_w dependent eccentricities of HRP in free and substrate bound states....	155
Figure 5.5 A comparison of the eccentricities of MbCO, H64V, and HRP	160

LIST OF TABLES

Table 4.1 Volumes of components mixed to prepare sol-gel encapsulated protein samples and their corresponding R-values.....	86
Table 4.2 FT-IR peak centers, linewidths, vibrational lifetimes (T_1), and the FFCFs for H64V, <i>Ht</i> -M61A, and HbCO	91
Table 5.1 Fits of linear spectra of free and substrate bound HRP.....	151
Table 5.2 FFCFs derived from linear and 2D-IR experimental data for HRP	158

CHAPTER 1: INTRODUCTION

1.1 PROTEIN DYNAMICS

Proteins are complex molecules that sample a rugged energy landscape on timescales that range from femtoseconds to seconds and longer. The importance of enzyme dynamics in facilitating catalysis,^{1,2} allostery,³ and substrate binding^{4,5} have been realized for decades. Molecular dynamics (MD) simulations have revealed that proteins sample an astonishing number of structural conformations within a short time.^{6,7} These rapid motions give rise to the slower processes associated with protein function. Understanding these fastest protein dynamics provides an important link between static protein structures, simulations, and other slower timescale experimental techniques.

Despite decades of continued research, probing the relevant mechanical degrees of freedom in a protein at thermal equilibrium remains a significant challenge for the experimentalist. The work presented in this thesis was undertaken with the goal of developing a novel ultrafast two dimensional infrared (2D-IR) spectroscopic method (see Section 1.2) and applying it to study the dynamics of several protein systems in aqueous and confined environments. Nonlinear femtosecond spectroscopic techniques, such as the 2D-IR vibrational echo, can probe ultrafast (100 fs to hundreds of ps) protein conformational fluctuations in order to relate these dynamics to the protein's physiological function and structure.⁸⁻¹⁴ Infrared spectroscopy probes the mechanical degrees of freedom associated with the motion of nuclei that comprise a local or normal mode of the molecule of interest. In the case of a chromophore embedded in a dynamic bath (such as a protein), the spectroscopic observables can report the timescales and amplitudes of the bath fluctuations. Non-linear spectroscopic methods, such as the 2D-IR vibrational echo introduced in Section 1.2, are particularly suited to probing the time-dependence of these protein fluctuations.

Much of our knowledge of the interdependence between dynamic fluctuations and protein function is illustrated by myoglobin, a ~17 kDa globular protein with the primary biological task of reversibly binding and transporting O₂ in muscle tissue. The

ability of myoglobin to bind O₂, and other biologically relevant diatomic ligands such as CO or NO is facilitated by a prosthetic iron heme group, which is tethered in a protein “pocket” to a proximal histidine. The static X-ray crystal structure of myoglobin does not reveal any channels through which the diatomic ligands may enter the protein pocket.^{15,16} A wealth of experimental data has established that ligands must traverse the protein to the active site via transient “channels” that are dynamically created as a result of the rapid protein structural fluctuations.¹⁷⁻¹⁹ Thus, in myoglobin, protein function is intimately tied to structural dynamics.

In Chapter 3 of this work, the dynamics of myoglobin and a distal histidine mutant are studied via 2D-IR spectroscopy and MD simulations. The application of complementary spectroscopic and computational studies can provide a detailed and self-consistent picture of protein structure, dynamics, and function.^{10,12,20-23} The dynamics of myoglobin are modeled well by a quantitative theory that relates the spectroscopic observables to minute fluctuations of the protein structure. An analysis of the simulations, in conjunction with the experimental data, highlights the importance of several key residues in modulating the protein dynamics, as sensed by carbon monoxide (CO) bound to the heme active site. In addition, 2D-IR spectroscopy is used to probe the dynamics of several cytochromes with mutations that introduce an additional hydrogen bond into the active site pocket. The 2D-IR method is shown to be sensitive to the changes in fluctuations that accompany the formation of hydrogen bond within the active site.

Chapter 4 presents several studies of protein structural dynamics in molecular confinement. Enzymes must function in crowded and relatively viscous intracellular milieu. Molecular confinement is known to significantly alter protein structure and function. For example, confinement of proteins in nanoscopic water pools such as the pores of a sol-gel glass or reverse micelles increases protein stability towards denaturation²⁴⁻²⁶ and can increase the enzymatic turnover.²⁷ Proteins in non-aqueous solvents are known to exhibit significantly modified substrate specificity and reaction rates.^{28,29} In Chapter 4, the dynamics of myoglobin and hemoglobin are studied in several confined environments such as a room temperature sugar glass, in nanoscopic

sol-gel pores, and as a function of viscosity. In addition, the dynamics of hemoglobin in human red blood cells are reported.

Chapter 5 presents studies of the effects of substrate binding on protein structural fluctuations. The dynamics of horseradish peroxidase (HRP) are probed in the free form and when ligated to several small substrates with varying binding affinities for the protein active site. HRP is a type III peroxidase family glycoprotein that oxidizes a variety of organic molecules in the presence of hydrogen peroxide as the oxidizing agent.³⁰ The active site of horseradish peroxidase is comprised of a relatively large cavity that contains a prosthetic heme group. Carbon monoxide bound to the heme active site serves as the spectroscopic probe for protein structural fluctuations. Protein dynamics are found to be significantly quenched in the substrate bound form. The observation that substrate binding, in addition to facilitating structural rearrangement, also significantly alters protein fluctuations suggests that ligand binding may play a crucial role in reorganizing the conformational dynamics of an enzyme to facilitate downstream enzymatic events.

1.2 2D-IR VIBRATIONAL ECHO SPECTROSCOPY

In 1950, the NMR “spin echo”³¹ ushered in the last half century of the development of coherent spectroscopic methods. The spin echo became the basis for the diverse range of pulsed NMR experiments, including multidimensional experiments, that are in use in fields of research from medicine to geology.^{32,33} In 1964, the basic concepts inherent in the spin echo were extended to visible spectroscopy using the earliest pulsed lasers to perform “photon echo” experiments on electronic excited states.^{34,35} Photon echoes have been widely used to study electronic excited state dynamics in systems such as low temperature crystals³⁶⁻⁴⁰ and glasses,⁴¹⁻⁴⁴ proteins,⁴⁵⁻⁴⁷ and photosynthetic chromophore clusters.^{48,49} The advent of short pulse infrared (IR) sources made it possible to perform “vibrational echo” experiments on the vibrations of condensed matter systems such as liquids, glasses and proteins beginning in the early 1990’s.⁵⁰⁻⁵⁴ These first one-dimensional two pulse vibrational echo experiments were conducted with an IR free electron laser.⁵⁰ However, rapid advances in laser technology now make it possible to conduct far more sophisticated

vibrational echo experiments, particularly two-dimensional (2D) vibrational echoes, using table top laser systems.

Ultrafast 2D-IR vibrational echo spectroscopy is an ultrafast IR analog of 2D NMR, but it operates on molecular vibrations instead of spins. Vibrations are the structural degrees of freedom of molecules. The ability to directly probe the dynamics of molecular structure and intermolecular interactions on ultrafast time scales makes 2D vibrational echo spectroscopy a powerful tool that is becoming increasingly useful as the methodology develops.

The 2D-IR vibrational echo signal is generated by a sequence of three ultrashort IR pulses tuned to the vibrational transitions of interest. The pulse sequence induces and then probes the coherent evolution of excitations (i.e. vibrations) of a molecular system. The first pulse in the sequence causes vibrational modes of an ensemble of molecules to “oscillate” initially all with the identical phase. The later pulses generate observable signals that are sensitive to changes in environments of individual molecules during the experiment, even if the aggregate populations in distinct environments do not change. For example, the structural fluctuations of a protein or the formation and dissociation of molecular complexes under thermal equilibrium conditions can be observed. The 2D-IR vibrational echo spectrum can also display intramolecular interactions and dynamics that are not observable in a linear IR vibrational absorption experiment because they are masked by the inhomogeneous broadening that, in general, dominates a linear absorption spectral line shape in complex condensed matter molecular systems. A critical difference between the 2D-IR and NMR variants is that the IR pulse sequence is sensitive to dynamics on timescales 6 to 10 orders of magnitude faster than NMR.

2D-IR vibrational echo spectroscopy has several characteristics that make it a useful tool to study problems involving rapid dynamics under thermal equilibrium conditions in condensed phases. Such problems are ubiquitous in nature and difficult to study by other means. 2D-IR vibrational echo experiments have temporal resolution of <100 fs, which is sufficiently fast to study the fastest chemical and biophysical processes. In contrast to electronic excitation, the vibrational excitation

associated with the 2D-IR experiments produces a negligible perturbation of a molecular system, and does not change the chemical properties of the samples. 2D-IR experiments can also be useful as a tool for chemical structural analysis by revealing the relationship among different mechanical degrees of freedom of a molecular system. 2D-IR vibrational echo experiments have been successfully applied to study fast chemical exchange reactions, solution dynamics,⁵⁵⁻⁵⁷ and protein structural dynamics.^{12,58,59}

Since the first fast condensed matter vibrational echo experiments in 1993,⁵⁰ the field has advanced a great deal. The first experiments were one-dimensional with a time resolution of ~1 ps. Today, multi-dimensional phase resolved vibrational echoes have become almost routine, greatly increasing the types of information that can be obtained. Furthermore, tabletop laser systems now provide sub 50 fs IR pulses, making 2D-IR vibrational echo spectroscopy increasingly available to a wide range of researchers. As the methodology and instrumentation continues to evolve, 2D-IR spectroscopy will increasingly become an indispensable tool in probing the fastest dynamics in complex condensed phase systems.

1.3 REFERENCES

- (1) Eisenmesser, E. Z.; Bosco, D. A.; Akke, M.; Kern, D. *Science* **2002**, *295*, 1520.
- (2) Kern, D.; Zuiderweg, E. R. *Curr Opin Struct Biol* **2003**, *13*, 748.
- (3) Berendsen, H.; Hayward, S. *Curr Opin Struct Biol* **2000**, *10*, 165.
- (4) Jimenez, R.; Salazar, G.; Yin, J.; Joo, T.; Romesberg, F. E. *Proc. Natl. Acad. Sci. USA* **2004**, *101*, 3803.
- (5) Ma, B.; Shatsky, M.; Wolfson, H. J.; Nussinov, R. *Protein Sci.* **2002**, *11*, 184.
- (6) Elber, R.; Karplus, M. *Science* **1987**, *235*, 318.
- (7) Vitkup, D.; Ringe, D.; Petsko, G. A.; Karplus, M. *Nature Struct. Bio.* **2000**, *7*, 34.
- (8) Jackson, T. A.; Lim, M.; Anfinrud, P. A. *Chemical Physics* **1994**, *180*, 131.
- (9) Lim, M.; Jackson, T. A.; Anfinrud, P. A. *J. Am. Chem. Soc.* **2004**, *126*, 7946.
- (10) Hummer, G.; Schotte, F.; Anfinrud, P. A. *Proc. Natl. Acad. Sci. USA* **2004**, *101*, 15330.
- (11) Brunori, M.; Cutruzzola, F.; Savino, C.; Travaglini-Allocatelli, C.; Vallone, B.; Gibson, Q. *Trends in Biochemical Sciences* **1999**, *24*, 253.
- (12) Merchant, K. A.; Noid, W. G.; Akiyama, R.; Finkelstein, I.; Goun, A.; McClain, B. L.; Loring, R. F.; Fayer, M. D. *J. Am. Chem. Soc.* **2003**, *125*, 13804.
- (13) McClain, B. L.; Finkelstein, I. J.; Fayer, M. D. *Chem. Phys. Lett.* **2004**, *392*, 324.
- (14) McClain, B. L.; Finkelstein, I. J.; Fayer, M. D. *J. Am. Chem. Soc.* **2004**, *126*, 15702.
- (15) Kendrew, J. C.; Dickerson, R. E.; Strandberg, B. E.; Hart, R. G.; Davies, D. R.; Phillips, D. C.; Shore, V. C. *Nature* **1960**, *185*, 422.
- (16) Kendrew, J. C. *Acta Cryst.* **1948**, *1*, 336.
- (17) Ansari, A.; Berendzen, J.; Braunstein, D.; Cowen, B. R.; Frauenfelder, H.; Hong, M. K.; Iben, I. E. T.; Johnson, J. B.; Ormos, P.; Sauke, T. B.; Scholl, R.; Schulte, A.; Steinbach, P. J.; Vittitow, J.; Young, R. D. *Biophys. Chem.* **1987**, *26*, 337.
- (18) Austin, R. H.; Beeson, K.; Eisenstein, L.; Frauenfelder, H.; Gunsalus, I. C.; Marshal, V. P. *Phys. Rev. Lett.* **1974**, *32*, 403.
- (19) Schotte, F.; Lim, M. H.; Jackson, T. A.; Smirnov, A. V.; Soman, J.; Olson, J. S.; Phillips, G. N.; Wulff, M.; Anfinrud, P. A. *Science* **2003**, *300*, 1944.
- (20) Merchant, K. A.; Noid, W. G.; Thompson, D. E.; Akiyama, R.; Loring, R. F.; Fayer, M. D. *J. Phys. Chem. B* **2003**, *107*, 4.
- (21) Merchant, K. A. *Ultrafast Multidimensional Vibrational Spectroscopy: Theoretical and Experimental Studies on Proteins and Model Compounds*, Stanford Univeristy, 2003.
- (22) Merchant, K. A.; Thompson, D. E.; Xu, Q.-H.; Williams, R. B.; Loring, R. F.; Fayer, M. D. *Biophys. J.* **2002**, *82*, 3277.
- (23) Williams, R. B.; Loring, R. F.; Fayer, M. D. *J. Phys. Chem. B* **2001**, *105*, 4068.

- (24) Das, T. K.; Khan, I.; Rousseau, D. L.; Friedman, J. M. *Journal of the American Chemical Society* **1998**, *120*, 10268.
- (25) Khan, I.; Shannon, C. F.; Dantsker, D.; Friedman, A. J.; Perez-Gonzalez-de-Apodaca, J.; Friedman, J. M. *Biochemistry* **2000**, *39*, 16099.
- (26) Yamanaka, S. A.; Nishida, F.; Ellerby, L. M.; Nishida, C. R.; Dunn, B.; Valentine, J. S.; Zink, J. I. *Chem. Mater.* **1992**, *4*, 495.
- (27) Martinek, K.; Levashov, A. V.; Klyachko, N.; Khmel'nitski, Y. L.; Berezin, I. V. *Eur. J. Biochem.* **1986**, *155*, 453.
- (28) Halling, P. J. *Curr. Opin. Chem. Biol.* **2000**, *4*, 74.
- (29) Klivanov, A. M. *Nature* **2001**, *409*, 241.
- (30) Veitch, N. C. *Phytochemistry* **2004**, *65*, 249.
- (31) Hahn, E. L. *Phys. Rev.* **1950**, *80*, 580.
- (32) Brown, M. A.; Semelka, R. C. *MRI: Basic Principles and Applications*; Wiley-Liss, 1999.
- (33) Dunn, K. J.; Bergman, D. J.; LaTorraca, G. A. *Nuclear Magnetic Resonance (Handbook of Geophysical Exploration: Seismic Exploration)*, 2002.
- (34) Kurnit, N. A.; Abella, I. D.; Hartmann, S. R. *Phys. Rev. Lett.* **1964**, *13*, 567.
- (35) Abella, I. D.; Kurnit, N. A.; Hartmann, S. R. *Phys. Rev.* **1966**, *141*, 391.
- (36) Aartsma, T. J.; Wiersma, D. A. *Chem. Phys. Lett.* **1978**, *54*, 415.
- (37) Hesselink, W. H.; Wiersma, D. A. *Phys. Rev. Lett.* **1979**, *43*, 1991.
- (38) Cooper, D. E.; Olson, R. W.; Wieting, R. D.; Fayer, M. D. *Chem. Phys. Lett.* **1979**, *67*, 41.
- (39) Olson, R. W.; Lee, H. W. H.; Patterson, F. G.; Fayer, M. D. *J. Chem. Phys.* **1982**, *76*, 31.
- (40) Gulotty, R. J.; Walsh, C. A.; Patterson, F. G.; Wilson, W. L.; Fayer, M. D. *Chem. Phys. Lett.* **1986**, *125*, 507.
- (41) Molenkamp, L. W.; Wiersma, D. A. *J. Chem. Phys.* **1985**, *83*, 1.
- (42) Berg, M.; Walsh, C. A.; Narasimhan, L. R.; Littau, K. A.; Fayer, M. D. *J. Chem. Phys.* **1988**, *88*, 1564.
- (43) Walsh, C. A.; Berg, M.; Narasimhan, L. R.; Fayer, M. D. *J. Chem. Phys.* **1987**, *86*, 77.
- (44) Walsh, C. A.; Berg, M.; Narasimhan, L. R.; Fayer, M. D. *Chem. Phys. Lett.* **1986**, *130*, 6.
- (45) Leeson, D. T.; Wiersma, D. A. *Phys. Rev. Lett.* **1995**, *74*, 2138.
- (46) Leeson, D. T.; Wiersma, D. A.; Fritsch, K.; Friedrich, J. *J. Phys. Chem. B.* **1997**, *101*, 6331.
- (47) Jordanides, X. J.; Lang, M. J.; Song, X.; Fleming, G. R. *J. Phys. Chem. B.* **1999**, *103*, 7995.
- (48) Jonas, D. M.; Lang, M. J.; Nagasawa, Y.; Joo, T.; Fleming, G. R. *J. Phys. Chem.* **1996**, *100*, 12660.
- (49) Zigmantas, D.; Read, E. L.; Mancal, T.; Brixner, T.; Gardiner, A. T.; Cogdell, R. J.; Fleming, G. R. *Proc. Natl. Acad. Sci.* **2006**, *103*, 12672.
- (50) Zimdars, D.; Tokmakoff, A.; Chen, S.; Greenfield, S. R.; Fayer, M. D.; Smith, T. I.; Schwettman, H. A. *Phys. Rev. Lett.* **1993**, *70*, 2718.

- (51) Rella, C. W.; Kwok, A.; Rector, K. D.; Hill, J. R.; Schwettmann, H. A.; Dlott, D. D.; Fayer, M. D. *Phys. Rev. Lett.* **1996**, *77*, 1648.
- (52) Rella, C. W.; Rector, K. D.; Kwok, A. S.; Hill, J. R.; Schwettman, H. A.; Dlott, D. D.; Fayer, M. D. *J. Phys. Chem.* **1996**, *100*, 15620.
- (53) Tokmakoff, A.; Zimdars, D.; Urdahl, R. S.; Francis, R. S.; Kwok, A. S.; Fayer, M. D. *J. Phys. Chem.* **1995**, *99*, 13310.
- (54) Tokmakoff, A.; Fayer, M. D. *Accounts of Chemical Research* **1995**, *28*, 437.
- (55) Zheng, J. R.; Kwak, K.; Asbury, J.; Chen, X.; Piletic, I. R.; Fayer, M. D. *Science* **2005**, *309*, 1338.
- (56) Kim, Y. S.; Wang, J.; Hochstrasser, R. M. *J. Phys. Chem. B* **2005**, *109*, 7511.
- (57) Zheng, J.; Kwak, K.; Xie, J.; Fayer, M. D. *Science* **2006**, 1951.
- (58) Rector, K. D.; Rella, C. W.; Kwok, A. S.; Hill, J. R.; Sligar, S. G.; Chien, E. Y. P.; Dlott, D. D.; Fayer, M. D. *J. Phys. Chem. B.* **1997**, *101*, 1468.
- (59) Zanni, M. T.; Hochstrasser, R. M. *Curr Opin Struct Biol* **2001**, *11*, 516.

CHAPTER 2: EXPERIMENTAL APPARATUS AND THEORETICAL FORMALISM

2.1 INTRODUCTION

The development of ultrafast mode-locked lasers has transformed and re-invigorated the field of physical chemistry. Regeneratively amplified lasers routinely deliver sub 50 fs pulses of light at terawatt peak power levels.^{1,2} Availability of high peak-power light sources has fueled the subsequent growth of ultrafast non-linear spectroscopic methods for probing the interaction of light with matter. Non-linear spectroscopies can probe a set of chromophores to “see” the time-evolution of the material of interest beyond the time and ensemble averaging that is inherent in linear spectroscopy. The first non-linear experiments employed visible pulses to probe the electronic degrees of freedom in dilute gases or cold crystalline systems. Advances in optical and laser technologies extended the range of these experiments to the mid- and far-infrared (IR) spectral regions, offering improved time resolution, and enabling the study of nuclear degrees of freedom in room temperature liquids.

Generation of ultrafast tunable mid-IR sources still poses a considerable challenge. Section 2.2 outlines the experimental apparatus that was used to generate the mid-IR pulses and to detect the resulting 2D-IR signal with complete frequency and phase information. The system consists of a modified commercial Ti:Sapphire regeneratively amplified laser that pumps an optical parametric amplifier (OPA). The OPA produces pulses in the near-IR that are subsequently down-mixed to generate tunable (3-8 μm) mid-IR femtosecond pulses. Section 2.2 outlines a versatile home-built mid-IR interferometer that was used to interrogate protein dynamics via 2D-IR vibrational echo spectroscopy and several other non-linear experiments.

Powerful theoretical formalisms have been developed to describe the growing family of non-linear laser experiments.³⁻⁶ Section 2.3 presents an overview of the stimulated photon echo experiment in the context of a semi-classical response function formalism developed by Mukamel and co-workers.⁶ Many excellent descriptions of this formalism can be found in the literature,⁶⁻⁸ and this section aims to present an

intuitive introduction to the topic. The discussion concludes with a description of the relationship between the theoretical formalism and spectroscopic observables via the frequency-frequency correlation function (FFCF) and how the FFCF is extracted from various experimental observables.

2.2 EXPERIMENTAL APPARATUS

2.2.1 Generation of Tunable mid-IR Light

The relatively weak non-linear signals generated in this study required the construction of a mid-IR light source with femtosecond time resolution, millijoules of energy per laser pulse, and excellent stability over a data acquisition time period of up to several days. The laser setup employed to generate the prerequisite mid-IR pulses is presented as a block diagram in Figure 2.1.

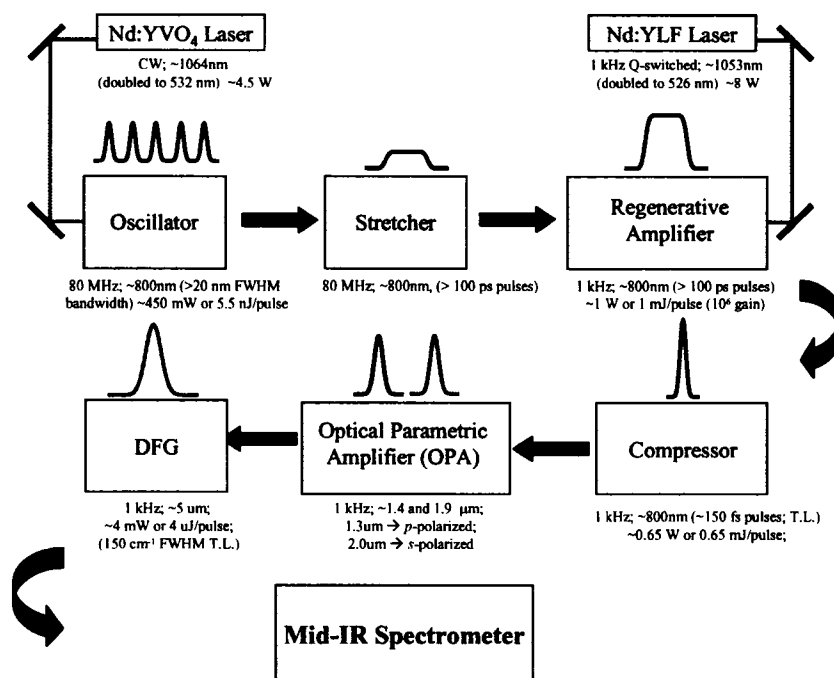


Figure 2.1 A block diagram of the laser system used to generate tunable ultrafast mid-IR laser pulses

A commercial (Spectra Physics Tsunami) Ti:Sapphire oscillator is at the heart of the light generation sequence used in all the mid-IR experiments described below. The Titanium-doped sapphire lasing medium affords broad lasing bandwidth and can produce extremely short (< 20 fs) pulses.^{1,2} In the commercial system employed for these studies, the typical pulse bandwidth was ~ 150 cm^{-1} . Since its inception nearly 15 years ago,^{9,10} the femtosecond mode-locked Ti:Sapphire laser has rapidly supplanted most other light sources for most ultrafast spectroscopy applications. Several detailed reviews offer a thorough description of the Ti:Sapphire oscillator,¹¹⁻¹⁴ and a brief overview will be provided below.

The oscillator is pumped by an intra-cavity doubled, continuous wave (cw), single mode Nd:YVO₄ (vanadate) diode laser. Typically, ~ 4.5 W of cw green light (532 nm) pump the oscillator. The Ti:Sapphire laser produces ~ 100 fs, nanojoule laser pulses at a frequency of ~ 86 Mhz with an average power of 450 mW (10% light conversion efficiency). The laser achieves passive mode-locking by generating a Kerr lens in the Ti:Sapphire rod that couples the temporal and spatial cavity modes.^{12,13} The optical Kerr-lens generation is a non-linear process in the sense that the refractive index changes non-linearly with the laser beam intensity. As the lensing increases, the index changes further, a self-focusing process that can ultimately lead to optical damage if unchecked. In the mode-locked Ti:Sapphire laser, this process is exploited to favor mode-locked (pulsed) lasing over cw emission.

The Spectra-Physics Tsunami laser uses a system of four prisms and spectral mask in the cavity to allow for chirp compensation and emission frequency selection. Two of the prisms compensate the group velocity dispersion (GVD) that is generated by transmission of the fs pulses through the Ti:Sapphire rod. The remaining two prisms and a spatial mask disperse the pulse frequencies spatially and select the desired emission wavelengths. The laser is tunable from ~ 750 - 850 nm, and during typical operation is set to the Ti:Sapphire emission maximum at ~ 800 nm.

The output of the Ti:Sapphire oscillator is directed into a commercial regenerative amplifier (Spectra Physics Spitfire) that reduces the repetition rate from 86 Mhz to 1 kHz and amplifies the power of each pulse by $\sim 10^6$. The regenerative

amplifier (regen) system consists of three discrete elements: a pulse stretcher, amplifier laser cavity, and pulse compressor. Amplification occurs in the regen laser cavity, but the large circulating power is sufficient to damage the cavity crystals and other intracavity optics. The stretcher reduces the peak circulating power by broadening the 800nm laser pulses temporally to > 100 ps before they are amplified and the compressor reverses this manipulation. Each is discussed in more detail below.

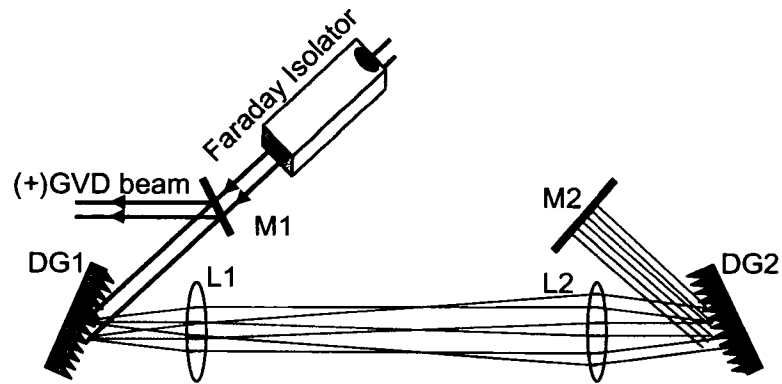


Figure 2.2 Ray-trace schematic of stretcher operation. In practice, the stretcher uses a single grating and a large curved mirror to fold the cavity and reduce the number of optics.

After ejection from the Ti:Sapphire oscillator, the 86 Mhz pulse train of nanojoule laser pulses is sent through a Faraday isolator and injected into the stretcher (see Figure 2.2). The Faraday isolator is necessary to reject back-propagating pulses that result from the amplifier injection scheme. Figure 2.2 presents an illustrative schematic of the pulse stretcher that utilizes two diffraction gratings and two lenses. The incoming laser beam passes between two mirrors in a roof-mirror configuration (M1) and diffracts from the first diffraction grating (DG1). The diffraction grating DG1 separates the pulse into a stripe of spectral components (shown as red, green, and blue rays) that pass through two lenses in a 1:1 telescope configuration. Diffraction from DG2 and reflection from roof mirror M2 guarantees that the red frequencies traverse the shortest pathlength relative to the blue frequencies. The roof mirror M2 reflects the stripe of frequencies back through DG2, L2 and L1, and finally onto DG1 to reverse the spatial (but not temporal) spread in frequencies. After a second

diffraction from DG1, the pulse is spatially reconstituted, but has significant linear positive group velocity dispersion (GVD or chirp). The reconstituted pulse is reflected from the roof mirror M1 and out of the stretcher. Typically, a ~ 100 fs pulse is stretched to > 100 ps before subsequent amplification and re-compression.

The stretcher design presented in Figure 2.2 is one of several schemes for adding positive GVD. Alternate designs utilize a pair of prisms or a combination of curved mirrors and diffraction gratings to minimize introduction of non-linear chirp that occurs with transmissive optics. The Spectra-Physics Spitfire regenerative amplifier replaces the two gratings and two lenses of Figure 2.2 with a single 1200 grooves/mm grating and a large curved mirror to minimize the number of optics and to fold the beam path into a smaller volume. The reduction in the number of optics necessitates multi-passing of the beam through the single diffraction grating and curved mirror, thereby increasing the alignment complexity.

The chirped ~ 86 Mhz pulse train propagates into an amplifier laser cavity shown below (Figure 2.3). The pulses reflect from the front face of a Ti:Sapphire rod cut at Brewster's Angle and are directed toward mirror M4. The pulse propagate through a $\lambda/4$ plate (PL1) and the first (injection) Pockels cell PC1. The Pockels cell is an optical crystal that acts as a switchable $\lambda/4$ plate when a ~ 3 kV electric field is placed across the two crystal faces. The beam transmits through an iris (I2) and is reflected from the cavity end-mirror M3 back through PC1 and PL1.

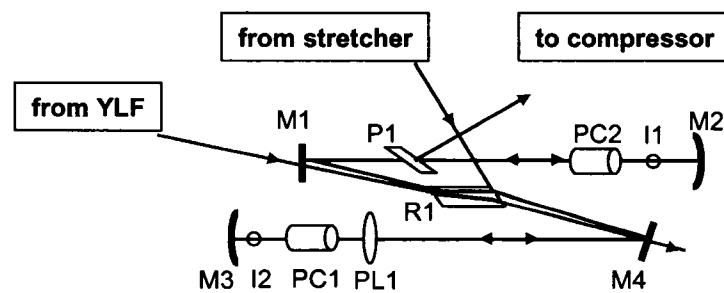


Figure 2.3 A schematic of the regenerative amplifier laser cavity.

The two polarization optics PC1 and PL1 form the basis of reducing the repetition rate of the pulse train from 86 MHz to 1 kHz. The majority of pulses pass through PC1 when it is acting as a $\lambda/4$ plate, thereby getting their polarization rotated by $\lambda/2$ on the first pass through PL1 and PC1 and immediately again by $\lambda/2$ after reflection from M3 (overall polarization unchanged). These pulses are back-reflected from the Brewster face of the Ti:Sapphire rod (R1) back into the stretcher cavity, where they are subsequently blocked by the Faraday isolator.

Pockels cell PC1 switches at 1 kHz, guaranteeing that one pulse per millisecond gets rotated by a total of $\lambda/2$ after being transmitted twice through both PC1 and PL1. This pulse has the necessary polarization to transmit through the Ti:Sapphire rod R1 and will be amplified by multiple passes through the laser cavity. It is reflected by M1 through a thin-film polarizer P1 and Pockels cell PC2 (ejection cell). The iris I1 and curved mirror M2 complete the laser cavity. After sufficient amplification, the pulse is ejected from the laser cavity by PC2. When PC2 fires, it rotates the trapped pulse polarization by $\lambda/4$ twice (double passed), which causes the beam to be ejected via a reflection from the front face of thin-film polarizer P1. The irises I1 and I2 are used to assure lasing in the TEM₀₀ mode.

Amplification power comes from an intra-cavity doubled, Q-switched Nd:YLF laser that produces nanosecond laser pulses with a repetition rate of 1 kHz. In practice, the firing of this laser is synchronized via fast digital electronics to the ~86 MHz pulse train from the Ti:Sapphire oscillator and the firing times of Pockels cells PC1 and PC2. The green beam is focused, and passed through mirror M1 to overlap with the cavity mode in the Ti:Sapphire crystal. It is dumped from the cavity through the dichroic mirror M4. Typical output after amplification is a 1 kHz pulse train with an average power of 1-1.3 W (1-1.3 mJ/pulse).

After amplification, the pulse is compressed in a manner analogous to the stretcher design described above. Figure 2.4 presents a schematic ray-trace diagram of a typical pulse compressor. In practice, the pulse is passed multiple times through a single diffraction grating that reverses the positive GVD to create a maximally

compressed, ~150-200 fs pulse. Four diffractions from a single grating that is 90% efficient give a typical operating efficiency of ~65%.

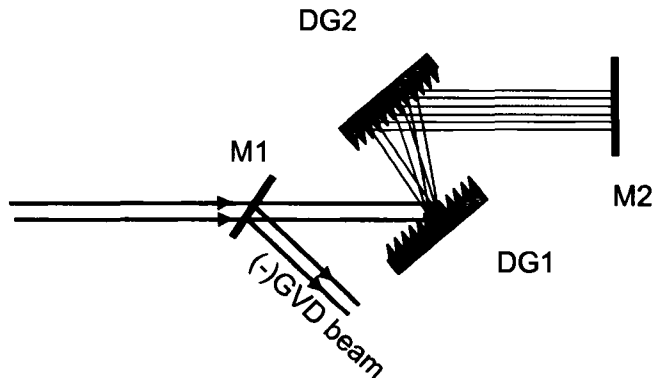


Figure 2.4 Ray-trace diagram of a pulse compressor. In practice, the laser beam is diffracted multiple times off a single diffraction grating.

The compressed 800 nm pulse is injected into a commercial (Spectra-Physics OPA 800) optical parametric amplifier (OPA). The OPA utilizes multiple non-linear optical crystals and $\chi^{(2)}$ parametric processes to down-convert the 800 nm light into a tunable, femtosecond 3-8 μm mid-IR pulse. A detailed description of the OPA has been presented elsewhere¹⁵ and only a brief overview will be provided below.

A small percentage (~3%) of the compressed and amplified 800 nm light is rotated by $\lambda/2$ and focused onto a Sapphire window to generate a white light supercontinuum. The rest of the red light is split into a weak (~10%) and strong beam that are subsequently passed through an angle tuned 3 mm type II BBO crystal. The weak 800 nm pulse (pre-amplifier) is overlapped with the white light in the BBO to generate a small amount of 1.3 μm (signal) and 2.0 μm (idler). The remaining strong 800 nm pulse (pump) is then overlapped with the idler light to amplify the 2.0 μm beam and generate more 1.3 μm light (signal). Excellent spatial and temporal overlap between the pulses in each of these non-linear processes is guaranteed by independent aiming and manual delay stages between the pump and white light pulses.

The near-IR signal and idler are separated from the residual 800 nm light by a dichroic mirror and are recombined in an angle tuned 0.5 mm type II AgGaS₂ crystal.

Spatial and temporal overlap is guaranteed by a manual re-timing stage and independent pointing control over each of the two pulses. Interaction of the signal and idler in the AgGaS₂ generates a stable, tunable ~4 μ J mid-IR laser pulse. The mid-IR pulse is separated from the residual signal and idler beams by transmission through a long-pass 2.5 μ m Germanium filter. The resulting mid-IR laser beam can be compressed to a transform limited Gaussian wavepacket with pulse duration of ~100 fs and RMS stability of $\pm 1\%$ over the course of a day.

2.2.2 2D-IR Interferometer

The work presented in this thesis employed pump-probe, transient grating, and homodyne and heterodyne detected stimulated vibrational echo experiments to probe different aspects of protein dynamics. In this context, non-linear experiments are those that require multiple light-matter interactions to generate a non-linear polarization in the sample. Thus, the signal scales as the square or cube power of the input field intensity. A description of the theory underpinning these experiments will be presented in the next section. For now, it is sufficient to say that a highly flexible experimental setup was required to accommodate the different pulse sequences and detection schemes required by each type of experiment. Furthermore, as the “state-of-the-art” improved, the experimental apparatus underwent several upgrade cycles. Rather than presenting a historical account of these modifications, the latest iteration of the 2D-IR experiment will be described in detail. The 2D-IR interferometer presented below was built with flexibility in mind and is capable of measuring the pump-probe, transient grating, or heterodyne detected vibrational echo experiments with a few changes to key interchangeable optics.

In a 2D-IR vibrational echo experiment, three ultrashort IR pulses tuned to the frequency of the vibrational modes of interest are crossed in the sample. Because the pulses are very short, they have a broad bandwidth, which makes it possible to simultaneously excite a number of vibrational modes or a very broad spectral feature. The IR pulses (~100 fs) are produced using a regeneratively amplified Ti:Sapphire laser pumped optical parametric amplifier system described above.¹⁶ A 2D-IR vibrational echo pulse sequence is illustrated below. The time ordering of the pulse

sequence is shown in Figure 2.5. The times between pulses 1 and 2 and pulses 2 and 3 are called τ and T_w , respectively. The three successive ultrashort IR pulses with wave vectors (propagation directions) \vec{k}_1 , \vec{k}_2 , and \vec{k}_3 are applied to the sample to induce the subsequent emission of the time delayed 4th pulse, the vibrational echo. The vibrational echo pulse is emitted from the sample in a distinct phase-matched direction, $\vec{k}_e = \vec{k}_2 + \vec{k}_3 - \vec{k}_1 - \vec{k}_1$.

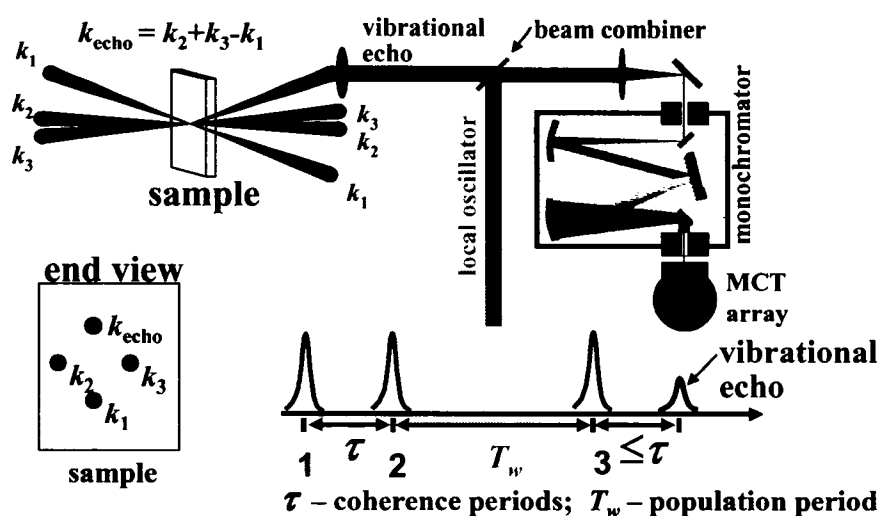


Figure 2.5 A schematic of the BOXCARS geometry, phase sensitive signal detection, and pulse sequence employed in generating the 2D-IR correlation spectra.

Both the intensity of the echo pulse and its time structure contain important information in the 2D-IR vibrational echo experiment. If the echo pulse is spectrally dispersed through a monochromator and sent directly into an IR detector, its intensity is measured (homodyne detection), but phase and sign information is lost. These first stimulated vibrational echo experiment constitute a significant portion of the experimental results presented in this thesis. A key technological breakthrough in linear stepper-motors that could reproducibly make 10 nm steps allowed implementation of a heterodyne detection strategy that was employed in the latest 2D-IR interferometer.

Complete information is obtained by allowing the vibrational echo pulse to interfere with a 5th pulse called the local oscillator (LO). In the heterodyne detected vibrational echo experiments, the local oscillator and vibrational echo pulses are collinear, and the phase information is obtained by observing the interference pattern (interferogram) as a function of time. In addition to providing phase and sign information, combining the vibrational echo with the local oscillator optically heterodyne amplifies the vibrational echo signal. The combined pulses are dispersed in a monochromator and then detected with a 32-element HgCdTe IR array detector, which measures the signal at 32 wavelengths simultaneously.

Figure 2.6 presents the home-built 2D-IR interferometer. The output of the OPA is collimated by a CaF₂ lens L1. To achieve the shortest time resolution (~100 fs), the linear chirp must be removed by a combination of materials (C1 and G1) that introduce either positive or negative GVD. Calcium Flouride (CaF₂) and Germanium (Ge) are both transparent in the IR and provide opposite GVD. The materials are set at Brewsters angle to guarantee maximum transmission of the IR light.

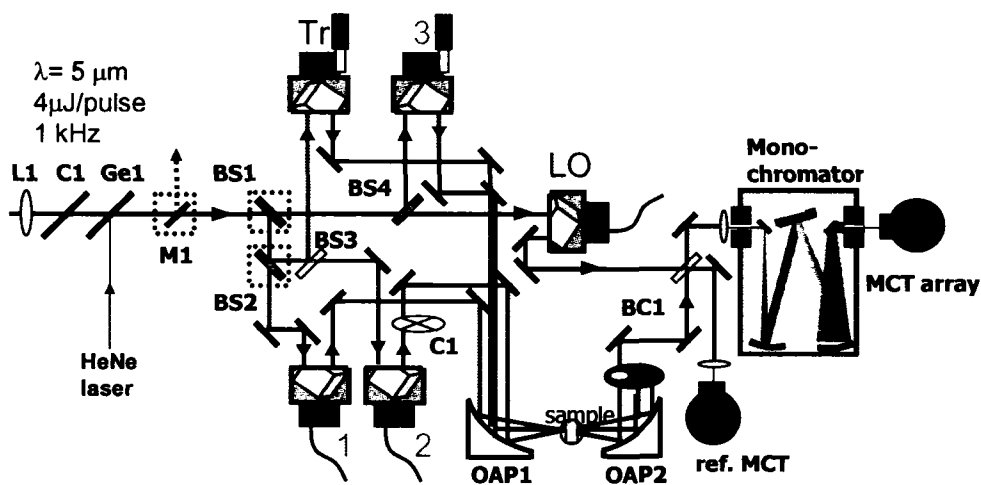


Figure 2.6 A simplified schematic of the 2D-IR interferometer. With beam splitters BS1 and BS2 in place, the instrument is capable of acquiring transient grating, and heterodyne detected 2D-IR data. Substituting BS1 and BS2 with mirrors re-configures the system for pump-probe measurements.

The Germanium (G1) is also used to overlap a cw Helium:Neon (HeNe) laser beam with the mid-IR pulse. The HeNe beam is made collinear with the mid-IR beam and used as a diagnostic for all subsequent alignments. The mirror M1 on a flipper stage deflects the beams through a series of diagnostic optics (not shown) that assure excellent co-alignment of the HeNe and IR laser beams over a distance of ~4 meters. The mirror M1 is removed (indicated by dotted black square) from the optical path during a typical experiment.

The main beam is split into 5 daughter pulses by Zinc Selenide (ZnSe) beam splitters BS1-BS4. In addition to being relatively transparent in the 0.7 – 20 μm spectral region (both mid-IR and HeNe beams are transmitted), ZnSe is an excellent optical material because it introduces almost zero GVD into the IR beam and thus does not broaden the temporal profile of the pulses significantly. Nonetheless, the beam is pre-compensated with chirp-compensation optics and the number of transmissions through the beam splitters of the crucial beams is conserved, thus theoretically introducing the same distortion in each of the beams.

The combination of beam splitters BS1-BS4 generates five beams, three of which are used for generating the non-linear signal. The fourth beam acts as a local oscillator (LO) and the fifth, a weak tracer beam, serves as a diagnostic during the vibrational echo experiments. Beam splitter BS1 splits the mother pulse equally into two pulses of 50% intensity. Beam splitters BS2 & BS4 split these pulses again equally, generation four pulses, each with ~25% of the total laser intensity. One of these four beams is transmitted through BS3, which is a partially coated (anti-reflective back face and uncoated front face) ZnSe optic that takes ~10% of this pulse for the tracer beam. The 5 beams are made to traverse through corner-cube retro-reflectors, three of which are on computer controlled delay stages and two of which are on manual delay stages. Delay stages 1-3 (see Figure 2.6) are used to control relative timing between the three pulses that generate the echo signal. The weak tracer beam goes through a manually controlled delay stage (Tr) and is co-aligned with the approximate echo path (based on the phase matching geometry).

Beams 1-3 and the tracer beams are arranged in a BOXCARS geometry (see Figure 2.5) and are focused into the sample by a six inch effective focal length off-axis parabolic reflector, OAP1. The generated echo signal, as well as the residual transmitted input beams, is collimated by an identical six inch effective focal length off-axis parabolic optic (OAP2). The echo is emitted in a unique direction and is spatially filtered from the input beams by an iris before it is made co-linear with the LO.

The local oscillator pulse traverses a computer controlled delay stage (LO in Figure 2.6), before it is mixed with the echo pulse in a ZnSe beam combiner (BC1). The beam combiner is un-coated on one side and anti-reflective on the other side to facilitate transmission of most of the weak echo pulse through the combiner, while a small percentage of the strong LO pulse is reflected along the echo path direction. The intensity of the LO is further controlled by swapping mirrors with Ge or CaF₂ wedges in the LO path. These optics reflect 5-50% of the incident beam (depending on the incident angle) and do not add any chirp into the beam path. The transmitted portion of the LO beam is used for diagnostics and as a shot-to-shot reference during data acquisition.

The collinear LO and echo pulses are dispersed through a 0.5 m monochromator (SPEX 500M) with a 210 grooves/mm grating onto a custom 32-element HgCdTe detector (MCT). The MCT has 48 independent amplification stages, 32 of which are dedicated to the array detector. The remaining 16 stages can be used with other external detectors. The 48 channels are multiplexed into a 16 bit A/D board that interfaces with a custom data acquisition package written in LabView.

During a typical 2D-IR experiment, the three input laser beams (with wave vectors \vec{k}_1 , \vec{k}_2 , and \vec{k}_3) are spatially and temporally overlapped in a sample that gives a strong non-resonant signal (e.g. carbon tetrachloride). Spatial overlap is optimized by independently adjusting each beam's mirrors while monitoring the total signal amplitude. Temporal overlap is optimized by scanning the experimental delay stages 1 & 2 and observing the maximum of the emitted non-resonant signal. Excellent temporal overlap can be achieved (< 2 fs) by this method. The non-resonant sample is

swapped for the appropriate protein sample and the input beams are no longer adjusted. The tracer beam is blocked during this alignment procedure.

The emitted echo pulse is co-aligned with the local oscillator over a ~2 meter path length (not shown in Figure 2.6) and sent through the monochromator onto the array detector. The time separation between the echo and LO pulses is computer controlled by the LO delay stage. To measure the temporal separation between the echo signal and the LO, the LO is translated ~3-4 ps away from the echo pulse and a spectral interferogram is observed. Spatial overlap is optimized by increasing the amplitude of the interferogram with a precision mirror mount. Temporal overlap between the LO and echo is adjusted by Fourier transforming the frequency domain interferogram into the time domain and computing the time-difference between the two beams. Before the start of the experiment, the timing of the LO pulse relative to the echo is set by moving the LO stage the distance measured via the spectral interferogram.

All optical phase-sensitive experiments are strongly affected by timing errors or pointing instabilities in any of the laser beams. At 5 μm , a single optical cycle has a time duration of only ~17 fs, thus a 2 fs error (~500 nm displacement) in one beam's optical path relative to another can introduce a potentially disastrous 40° phase error between two signals. To account for experimental time-overlap errors, non-linear chirp, and other experimental considerations a “phasing” procedure needs to be performed.¹⁶

2.3 THEORETICAL FORMALISM

Within a semi-classical formalism of light-matter interaction, the radiation field is treated as a classical electromagnetic wave that interacts with either the electrons or nuclei of a quantum chromophore. The interaction of light with matter generates a time dependent polarization

$$\mathbf{P}(\mathbf{r}, t) = \mathbf{P}_r(\mathbf{r}, t) + \mathbf{P}_{nr}(\mathbf{r}, t) \quad (2.3-1)$$

where $\mathbf{P}_r(\mathbf{r},t)$ represents the resonant contribution to the total polarization and $\mathbf{P}_{nr}(\mathbf{r},t)$ is the non-resonant component of the polarization. The induced total polarization, $\mathbf{P}(\mathbf{r},t)$, then acts as a source term in Maxwell's equations, inducing the generation of a signal electric field that can be detected optically. The resonant component of the polarization couples the quantized energy levels of the chromophore, whereas the non-resonant polarization occurs due to the induced ballistic motion of the electrons or nuclei when an intense electric field is present. The non-resonant term in Equation (2.3-1) is present in all non-linear experiments when the laser pulses are temporally overlapped in the sample, but does not contain information on the dynamics of the system. Thus, it is desirable to suppress the contribution of the non-resonant polarization by utilizing ultrafast laser pulses. The resonant polarization, $\mathbf{P}_r(\mathbf{r},t)$, contains all of the dynamical information regarding the interaction of the chromophore with its bath and the remainder of this section will focus on describing a theoretical approach to calculate this quantity.

In the limit of weak perturbations, it is convenient to expand $\mathbf{P}_r(\mathbf{r},t)$ as a Taylor series in the electric field

$$\mathbf{P}_r(\mathbf{r},t) = \mathbf{P}_r^{(1)}(\mathbf{r},t) + \mathbf{P}_r^{(2)}(\mathbf{r},t) + \mathbf{P}_r^{(3)}(\mathbf{r},t) + \dots \quad (2.3-2)$$

where $\mathbf{P}_r^{(n)}(\mathbf{r},t)$ describes the polarization generated in the sample due to an n th order interaction with the electric field. In centrosymmetric systems, all even-order components vanish, and the lowest order non-linear component is $\mathbf{P}_r^{(3)}(\mathbf{r},t)$.³ Non-linear experiments such as the vibrational echo or pump-probe spectroscopy measure this component of the total polarization. The quantity $\mathbf{P}_r^{(3)}(\mathbf{r},t)$ provides the bridge between theoretical treatments of the chromophore-bath systems and measurable spectroscopic observables.

To compute $\mathbf{P}_r^{(3)}(\mathbf{r},t)$, we must consider a generalized Hamiltonian that takes into account both the system and bath, as well as the system bath coupling and interaction with the electromagnetic field

$$\hat{H}_{tot} = \hat{H}_s(\mathbf{P}, \mathbf{Q}) + \hat{H}_b(\mathbf{p}, \mathbf{q}) + \hat{H}_{sb}(\mathbf{P}, \mathbf{Q}, \mathbf{p}, \mathbf{q}) + \hat{H}_{RM}(\mathbf{Q}, \mathbf{r}, t) \quad (2.3-3)$$

where $\hat{H}_s(\mathbf{P}, \mathbf{Q})$ is the system Hamiltonian that only depends on the internal degrees of freedom, the position and momenta, \mathbf{Q} and \mathbf{P} . $\hat{H}_b(\mathbf{p}, \mathbf{q})$ is the bath Hamiltonian that is a function of the bath momenta and positions, \mathbf{p} and \mathbf{q} . \hat{H}_{sb} is the system bath coupling and $\hat{H}_{RM}(\mathbf{Q}, \mathbf{r}, t)$ denotes the radiation-matter interactions. In the transition dipole coupling model, $\hat{H}_{RM}(\mathbf{Q}, \mathbf{r}, t)$ is expressed as

$$\hat{H}_{RM}(\mathbf{Q}, \mathbf{r}, t) = -\hat{\mu}(\mathbf{Q}) \cdot \mathbf{E}(\mathbf{r}, t) \quad (2.3-4)$$

where $-\hat{\mu}(\mathbf{Q})$ is the dipole operator and $\mathbf{E}(\mathbf{r}, t)$ represents the electric field. The next step involves solving the time-dependent generalized Hamiltonian given in Equation (2.3-3). Rather than recapitulating the full diagrammatic perturbation treatment, an intuitive physical picture will be developed in the discussion below.

2D-IR experiments probe nuclear degrees of freedom. The unperturbed system Hamiltonian, $\hat{H}_s(\mathbf{P}, \mathbf{Q})$, is approximated by a harmonic oscillator with potential energy levels H_0, H_1, \dots (see Figure 2.7). The energy difference between the ground and first excited states is $\hbar\omega_{01}$. The change in transition energies of the chromophore when immersed in a generalized bath is summarized by

$$H_{sb}(t) = \langle H_{sb} \rangle + \delta H_{sb}(t) \quad (2.3-5)$$

where $\langle H_{sb} \rangle$ denotes the solvatochromatic shift (indicated by a change in the potential energy levels in Figure 2.7) and $\delta H_{sb}(t)$ encapsulates the time dependent solvent-bath dynamics. For the case of carbon monoxide (CO) bound to the active site of heme proteins, the CO transition frequency shifts from 2131 cm^{-1} in the gas phase¹⁷ to $\sim 1900\text{-}1980 \text{ cm}^{-1}$ in the proteins.

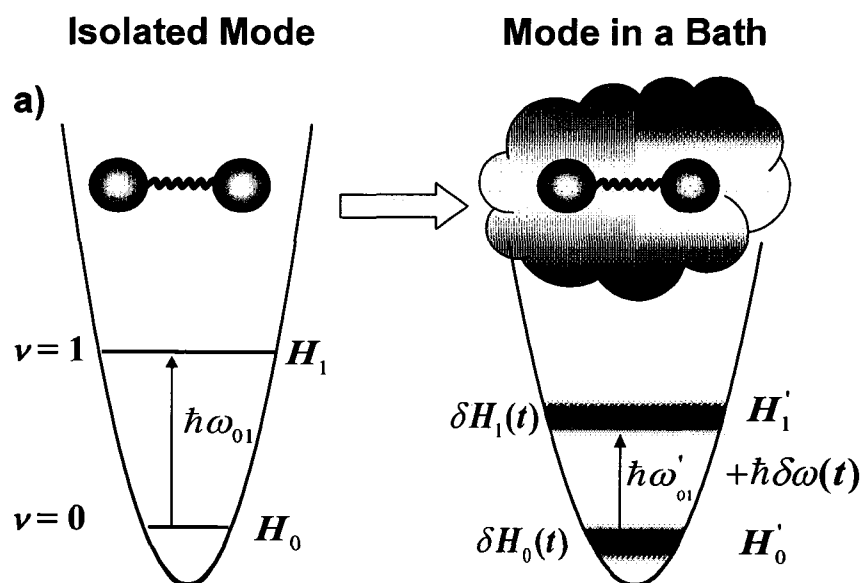


Figure 2.7 A diagram depicting the changes that occur to the potential energy levels of an isolated harmonic oscillator upon immersion in a dynamic bath. The oscillator is depicted as two balls connected by a spring. Upon immersion in a bath (right side of the figure) the energy levels shift and acquire a time-dependence. Time-domain non-linear spectroscopies are capable of probing this fluctuation in the energy levels to learn various aspects of bath-chromophore dynamics.

The protein and solvent constitute the generalized bath, and the time-dependent transition frequency, $\delta\omega(t)$, that arises due to chromophore-bath interactions is the fundamental quantity of interest. Obtaining information about $\delta\omega(t)$ is complicated by the ensemble averaging nature of the experiment. In complex condensed phase systems such as the protein studies described in the following chapters, the ensemble of chromophores populates a statistical distribution of slightly different microenvironments, with corresponding inhomogeneity in the transition frequencies. Inhomogeneous broadening in the protein systems is observed as a relatively broad Gaussian band in the FT-IR spectrum. This concept is illustrated in Figure 2.8a. It is useful to separate the time-dependent frequency fluctuations into several limits. Relatively fast dynamics that cause fluctuations in $\delta\omega(t)$ around some mean equilibrium value, $\langle\omega\rangle$, occur on the fastest timescales (Figure 2.8b). Slower fluctuations of each chromophore's microenvironment lead to spectral diffusion of individual absorbers within the inhomogeneous distribution. The vibrational echo

experiments that are described below are able to probe the time evolution of the system on both the fast and slower (spectral diffusion) timescales. In the limit of Gaussian bath fluctuations, a two-time frequency-frequency correlation function of the form

$$C(t) = \langle \delta\omega(0)\delta\omega(t) \rangle \quad (2.3-6)$$

summarizes both the fast and slower timescale dynamics. $C(t)$ measures how quickly a distribution of frequencies is randomized due to solvent-bath coupling. In principle, $C(t)$ can be obtained from the FT-IR spectrum. In practice, the FT-IR spectrum is a steady-state measurement that reports an ensemble *and* temporally averaged linewidth, thereby obscuring the underlying solvent-bath interaction dynamics. Third order experiments, such as the vibrational echo described qualitatively below, are able to access the chromophore dynamics with sufficient time resolution to see the fastest solvent-bath interactions.

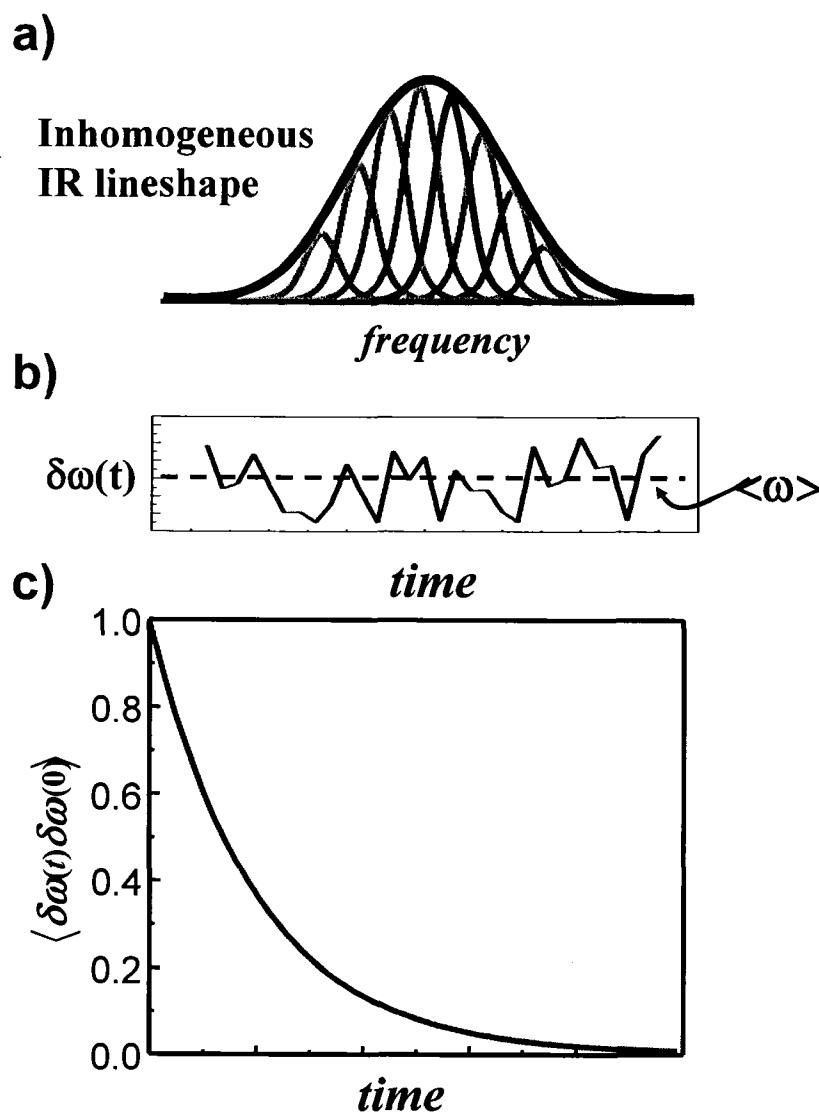


Figure 2.8 (a) An ensemble of microenvironments in a complex condensed phase system leads to a Gaussian, inhomogeneously broadened linear absorption spectrum. (b) Time-dependent frequency fluctuations of an ensemble of chromophores reports on the system-bath coupling dynamics. (c) A frequency-frequency correlation function provides the link between spectroscopic observables and theory. The correlation function measures the rate at which a distribution of frequencies is randomized, and is generally modeled as a monotonically decreasing function, eg. a sum of exponentials.

2.4 THE 2D-IR VIBRATIONAL ECHO EXPERIMENT

2.4.1 A Qualitative Description of the Vibrational Echo

The vibrational echo experiment employs three ultrafast mid-IR laser pulses with experimentally controlled delay times to induce a third-order polarization in the

material. In the vibrational echo experiment, the ultrafast pulses create and manipulate superpositions of molecular quantum states, and are thus able to peer behind the ensemble and time averaging of the material dynamics. Qualitatively, the vibrational echo experiment works in the following manner. The first pulse in the sequence places the vibrational oscillators into a coherent superposition state of the vibrational ground state (0) and the vibrational first excited state (1), with all of the oscillators initially in phase. The initial phase relationship among the oscillators decays rapidly causing a decay of the initial macroscopic polarization that is generated by an in-phase ensemble of oscillators. The decay of the macroscopic polarization is the free induction decay. The phase relationship between the oscillators decays because of inhomogeneous broadening of the spectral line (a spread of transition frequencies) with additional contributions from fast fluctuations of the transition frequencies caused by structural dynamics of the system. The rest of the pulse sequence can recover the phase relationships seemingly lost during the free induction decay because of inhomogeneous broadening. Only structural fluctuations that randomize the initial starting frequencies of the ensemble of oscillators (produce spectral diffusion) and occur over a sufficiently long time can totally destroy the phase relationship among the oscillators. This loss of phase relationships due to spectral diffusion cannot be recovered by the rest of the pulse sequence. However, even then, the signal is not zero because the initial two pulses also set up a spatial grating among the oscillators that contributes to the signal.

The second pulse in the sequence stores the phase (and spatial) information induced by the first pulse as a complex frequency and spatial pattern of alternating the populations of the 0 and 1 vibrational states. After the waiting period, T_w , (see Figure 2.5) the third pulse again generates coherent superposition states of the oscillators. Initially, the oscillators are not in phase, but the pulse sequence initiates a rephasing process.¹⁸ At a time $\leq \tau$ after the third pulse, the vibrational oscillators are again rephased. Each vibrational oscillator has associated with it a microscopic oscillating electric dipole. When rephasing has occurred, the sample again has a macroscopic polarization and, therefore, a macroscopic oscillating electric dipole that acts as the

source of the fourth pulse, the vibrational echo. The pulse is short because the dipoles again get out of phase just as they did after the first pulse.

In a dynamic system, the first laser pulse “labels” the initial structures of the species in the sample and initiates the first coherence period. The second pulse ends the first coherence period, τ , and starts clocking the waiting time during which the labeled species undergo structural dynamics that change their frequencies. The third pulse ends the waiting period of length T_w , and begins the last coherence period of length $\leq \tau$, which ends with the emission of the vibrational echo pulse. The echo signal contains information about the final structures of all labeled species.

During the coherence periods the ensemble of oscillators is in a coherent superposition of two vibrational states. Fast vibrational oscillator frequency fluctuations induced by fast structural fluctuations of the system cause dynamic dephasing, which is one contribution to the line shape in the 2D spectrum. During the T_w period, called the population period, all vibrations are consigned to either the ground or first excited vibrational state, not a superposition state. Slower structural fluctuations of the system give rise to spectral diffusion (slower time scale evolution of the oscillator frequencies), which also contributes to the 2D line shapes. Other processes during the population period also produce changes in the 2D spectrum. For example, chemical exchange can occur in which two species in equilibrium are interconverting one to the other without changing the overall number of either species.¹⁹ Chemical exchange causes new peaks to grow in as T_w is increased. In an experiment, τ is scanned for fixed T_w . The recorded signals are converted into a 2D vibrational echo spectrum. Then T_w is increased and another spectrum is obtained. The series of spectra taken as a function of T_w provides information on dephasing, spectral diffusion, and population dynamics.

To obtain the well resolved 2D vibrational echo spectra discussed below, it is necessary to acquire essentially pure absorption spectra. The measured interferogram contains both the absorptive and dispersive components of the vibrational echo signal. To isolate the absorptive features, two sets of quantum pathways are measured independently by appropriate time ordering of the pulses in the experiment.²⁰ With

pulses 1 and 2 at the time origin, pathway 1 or 2 is obtained by scanning pulse 1 or 2 to negative time, respectively. By adding the Fourier transforms of the interferograms from the two pathways, the dispersive component can be substantially cancelled leaving only the absorptive component.²⁰⁻²² The 2D vibrational echo correlation spectrum is constructed by plotting the amplitude of the absorptive part of the stimulated vibrational echo as a function of both ω_m (the emission frequencies, as measured through the monochromator) and ω_t (the absorption frequencies, obtained by numerically Fourier transforming the interferogram generated by scanning the τ delay stage).

Lack of perfect knowledge of the timing of the pulses and consideration of chirp on the vibrational echo pulse requires a “phasing” procedure to be used.^{16,23} The projection slice theorem^{20-22,24} is employed to generate the absorptive 2D correlation spectrum. The projection of the absorptive 2D correlation spectrum onto the ω_m axis is equivalent to the IR pump-probe spectrum recorded at the same T_w , as long as all the contributions to the stimulated vibrational echo are absorptive. Consequently, comparison of the projected 2D stimulated vibrational echo spectrum with the pump-probe spectrum permits the correct isolation of the absorptive vibrational echo correlation spectrum from the 2D spectrum obtained from the addition of the two quantum pathways.

2.4.2 Calculation of the 2D-IR Spectra

We calculate the vibrational echo signal from third-order perturbation theory in the radiation-matter interaction^{6,7}. The third-order nonlinear polarization can be expressed as the sum of eight relevant response functions after application of the rotating wave approximation and the phase-matching condition $\vec{k}_s = \vec{k}_2 + \vec{k}_3 - \vec{k}_1$ ^{6,7}. The material system is treated as a quantum-mechanical three-level system, coupled to a classical solvent that is treated within a second-order cumulant expansion. Within this approximation, the dynamics of the system can be described with a two-time autocorrelation function. Autocorrelation functions of fluctuations in the frequencies

of one-quantum transitions are set equal to the classical mechanical autocorrelation function of frequency fluctuations

$$C(t) = \langle \delta\omega_{10}(t)\delta\omega_{10}(0) \rangle = \langle \delta\omega_{21}(t)\delta\omega_{21}(0) \rangle \quad (2.4-1)$$

$$\delta\omega_{10}(t) = \omega_{10}(t) - \langle \omega_{10} \rangle \quad (2.4-2)$$

where $\delta\omega_{10}(t)$ denotes the time dependent fluctuations in the ensemble averaged mean transition frequency between the ground and first excited states, $\langle \omega_{10} \rangle$. $\delta\omega_{21}(t)$ denotes the time dependent frequency fluctuations of the 2-1 transition. The assumption inherent in Equation (2.4-1) is that the changes in the ground and excited state Hamiltonians are perfectly correlated. This assumption is valid in vibrational spectroscopy due to the relatively low perturbation of the system by mid-IR light but must be reconsidered in electronic spectroscopy where significant chromophores and solvent reconfiguration proceeds optical excitation. The lifetime of the second excited state is taken to be half that of the first excited state²⁵, and the transition dipole moments are related by $\mu_{21} = \sqrt{2}\mu_{10}$, as appropriate for a nearly harmonic vibration²⁶. Within this model, the eight response functions are given by^{6,7}

$$R_1 = R_2 = \left| \overline{\mu}_{10} \right|^4 e^{-i\omega_{10}(t_3-t_1)} e^{-\frac{(t_1+2t_2+t_3)}{2T_1}} \exp(-g(t_1) + g(t_2) - g(t_3) - g(t_2 + t_1) - g(t_3 + t_2) + g(t_1 + t_2 + t_3)) \quad (2.4-3)$$

$$R_3 = -\left| \overline{\mu}_{10} \right|^2 \left| \overline{\mu}_{21} \right|^2 e^{-i\omega_{10}(t_3-t_1)} e^{i\Delta t_3} e^{-\frac{(t_1+2t_2+3t_3)}{2T_1}} \exp(-g(t_1) + g(t_2) - g(t_3) - g(t_2 + t_1) - g(t_3 + t_2) + g(t_1 + t_2 + t_3)) \quad (2.4-4)$$

$$R_4 = R_5 = \left| \overline{\mu}_{10} \right|^4 e^{-i\omega_{10}(t_1+t_3)} e^{-\frac{(t_1+2t_2+t_3)}{2T_1}} \exp(-g(t_1) - g(t_2) - g(t_3) + g(t_2 + t_1) + g(t_3 + t_2) - g(t_1 + t_2 + t_3)) \quad (2.4-5)$$

$$R_6 = -\left| \overline{\mu}_{10} \right|^2 \left| \overline{\mu}_{21} \right|^2 e^{-i\omega_{10}(t_3+t_1)} e^{i\Delta t_3} e^{-\frac{(t_1+2t_2+3t_3)}{2T_1}} \exp(-g(t_1) - g(t_2) - g(t_3) + g(t_2 + t_1) + g(t_3 + t_2) - g(t_1 + t_2 + t_3)) \quad (2.4-6)$$

$$R_7 = \left| \overline{\mu}_{10} \right|^2 \left| \overline{\mu}_{21} \right|^2 e^{-i\omega_{10}(t_1+2t_2+t_3)} e^{i\Delta t_2} e^{-\frac{(t_1+2t_2+t_3)}{2T_1}} \exp(g(t_1) - g(t_2) + g(t_3) - g(t_2 + t_1) - g(t_3 + t_2) - g(t_1 + t_2 + t_3)) \quad (2.4-7)$$

$$R_8 = -\left|\overline{\mu}_{10}\right|^2 \left|\overline{\mu}_{21}\right|^2 e^{-i\omega_{10}(t_1+2t_2+t_3)} e^{i\Delta(t_2+t_3)} e^{\frac{(t_1+2t_2+3t_3)}{2T_1}} \exp(g(t_1) - g(t_2) + g(t_3) - g(t_2+t_1) - g(t_3+t_2) - g(t_1+t_2+t_3)) \quad (2.4-8)$$

where ω_{10} is the fundamental transition frequency, Δ is the anharmonicity, and T_1 is the lifetime of the first vibrational excited state. The effect of the bath on the chromophore dynamics enter these response functions through the line-broadening function, $g(t)$:

$$g(t) = \int_0^t d\tau_1 \int_0^{\tau_1} d\tau_2 C(\tau_2) \quad (2.4-9)$$

The third order polarization is calculated by convolving the material response functions with the applied electric field:

$$P_r^{(3)}(\tau, T_w, t) \propto \int_0^\infty dt_3 \int_0^\infty dt_2 \int_0^\infty dt_1 \left(\sum_i R_i(t_3, t_2, t_1) \right) \times E_3(t-t_3) E_2(T_w+t-t_3-t_2) E_1^*(\tau+T_w+t-t_3-t_2-t_1) \quad (2.4-10)$$

In complex condensed phase systems, a chromophore may exhibit multiple spectrally distinct substates that appear as multiple peaks in the linear absorption spectrum. For example in the case of carbon monoxide bound to myoglobin (MbCO), the FT-IR spectrum of the CO stretch exhibits three spectrally distinct substates. In such systems, the third order nonlinear response function is calculated by treating each of the conformational substates as a distinct non-interconverting species. (A more complicated formalism is required in the case when the species may interconvert during the experimental observation window.^{19,27}) Each nonlinear response function is convolved with the temporal profiles of the excitation fields as shown in Equation (2.4-10) to yield the nonlinear polarization for that substate, and the total nonlinear polarization is computed from a concentration weighted sum of polarizations associated with each conformer

$$P_{total}^{(3)}(\tau, T_w, t) = \sum_{\alpha} c_{\alpha} P_{\alpha}^{(3)}(\tau, T_w, t) \quad (2.4-11)$$

where c_{α} is the concentration, $P_{\alpha}^{(3)}$ is the nonlinear polarization, and α is the index labeling the conformational substates. The transition dipole moment and anharmonicity were assumed to be the same for each substate. The concentrations, c_{α} , are obtained from the linear absorption spectrum.

In the homodyne detection scheme, the third order polarization is dispersed through a monochromator and measured as a function of frequency at the intensity level

$$I_s(\tau, T_w, \omega_m) = \left| \int_{-\infty}^{\infty} dt P^{(3)}(\tau, T_w, t) e^{-i\omega_m t} \right|^2 \quad (2.4-12)$$

where ω_m is the frequency axis that is obtained by the optical Fourier transform performed in the monochromator. In this detection strategy, phase and sign information of the third order polarization are lost. A more advanced, heterodyne detection strategy is capable of measuring the complete third order polarization. In this strategy, the third order polarization is mixed with a local oscillator pulse before being dispersed through the monochromator. In this case, the signal is expressed as

$$I_s(\tau, T_w, \omega_m) = \left| \int_{-\infty}^{\infty} dt \left[P^{(3)}(\tau, T_w, t) + E_{LO}(t) \right] e^{-i\omega_m t} \right|^2 \quad (2.4-13)$$

where $E_{LO}(t)$ represents the local oscillator electric field. The total signal is comprised of three contributions

$$I_s = |E_{LO}|^2 + 2\text{Re}[E_{LO}^* \cdot P^{(3)}] + |P^{(3)}|^2 \quad (2.4-14)$$

The first term in Equation (2.4-14) does not contain any information about the material response and can be subtracted from the observed signal during data acquisition. The last term in Equation (2.4-14) is negligibly small compared to the middle term, which now encapsulates the dynamics of interest.

The linear absorption spectrum of the CO vibration is calculated within the same approximations used to calculate the nonlinear polarization, and is given as the Fourier transform of $I(t)$, a weighted sum of contributions from the conformational substates:

$$I(t) = \sum_{\alpha} c_{\alpha} I_{\alpha}(t) \quad (2.4-15)$$

$$I_{\alpha}(t) = \left| \vec{\mu}_{10} \right|^2 e^{-i\omega_{\alpha} t} e^{-t/2T_1} e^{-g_{\alpha}(t)} \quad (2.4-16)$$

where the subscript α is used to denote the different substates of the protein.

To extract $C(t)$ from the experimental observables, a fitting algorithm with a model frequency-frequency correlation function is employed. A multi-exponential form of $C(t)$ conveniently organizes a distribution of protein fluctuation rates into several timescales and has been found to adequately reproduce structural dynamics in multiple heme proteins²⁸⁻³⁰

$$C(t) = \sum_{i=1}^n \Delta_i^2 e^{-t/\tau_i} + \Delta_0^2 \quad (2.4-17)$$

The static component in $C(t)$, Δ_0 , is the contribution to the frequency distribution that occurs from protein structures that interconvert slower than the experimental timescales. Typically, a bi-exponential plus a constant correlation function is necessary to describe structural fluctuations in proteins. The 2D-IR experiment is sensitive to dynamics that occur out to several T_w ,³¹ $C(t)$ were extracted from the experimental data via an iterative fitting algorithm. The correlation function obtained from analysis of the data using response theory calculations was deemed correct when it could be used to simultaneously calculate 2D-IR spectra that accurately reproduced the vibrational echo data at all T_w and the linear absorption spectrum, to capture the slowest dynamics. Generally, excellent agreement is achieved between the data and calculations (see Chapters 3-5).

2.5 TRANSIENT GRATING AND PUMP-PROBE EXPERIMENTS

Spectrally resolved pump-probe and transient grating experiments are routinely collected to measure the vibrational lifetime and to aid in phasing the 2D-IR spectrum. A homodyne detected transient grating (TG) experiment is a limiting case of the vibrational echo pulse sequence described above. The homodyne TG uses the same pulse sequence as described for the vibrational echo, but unlike the vibrational echo, the TG signal is acquired by scanning T_w (time between pulses 2 and 3) while holding $\tau = 0$. The signal is emitted in the same phase matched direction as the vibrational echo and is dispersed through a monochromator onto an array detector. The TG experiment does not require any changes in the laser setup and is a background free experiment in the sense that one is not looking for a small change on top of a large signal (such as in pump-probe), but rather a small signal with zero background. The TG signal can be written as:

$$S_{TG}(t; \omega) \propto \left(e^{-t/T_1} \right)^2 = \left| e^{-t/2T_1} \right| \quad (2.5-1)$$

where $S_{TG}(t; \omega)$ is the TG signal as a function of the time between the first two pulses and pulse 3, ω is the detection frequency, and T_1 is the vibrational lifetime. Since the signal is acquired at the intensity level, it contains both absorptive and dispersive components, all sign information is lost, and the observed exponential decays at $2T_1$ (twice as fast). In principle, heterodyne detection of the TG signal may be employed and can offer several advantages over a pump-probe experiment (such as enhanced polarization sensitivity), but experimental phase shifts between the LO and signal pulses would have to be corrected.

The pump-probe experiment can also be used to measure the vibrational lifetime more directly, but requires a slight modification to the laser setup. A schematic of the pulse sequence employed in the pump-probe experiment is presented in Figure 2.9. A strong pump-pulse (95% of total laser intensity) and significantly weaker probe pulse are crossed in the sample. The probe pulse is subsequently dispersed through a monochromator onto a 32-element MCT array detector. The

experimental time t between the pump and probe pulses is scanned by a computer controlled delay stage.

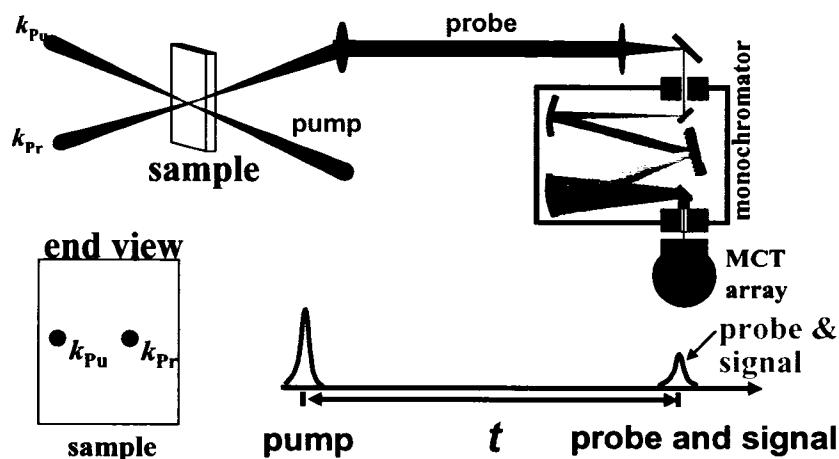


Figure 2.9 A schematic of the pump-probe setup.

The pump-probe experiment generates a non-linear third order polarization that is co-linear and phase locked with the probe beam, thereby giving full frequency and phase information without need for phasing the data. Pump-probe spectra are purely absorptive and contain full sign information and spectra, thereby making them extremely useful for phasing and interpreting 2D-IR spectra.

The 2D-IR experimental setup is designed to be easily converted into pump-probe beam geometry by replacing beam splitters BS1 and BS2 by two mirrors (see Figure 2.6). The total laser pulse is directed towards the $\sim 10\%$ / 90% beam splitter BS3, and the weak beam (Tr) becomes the probe and strong pump beam is directed through the computer controlled delay stage 2. The choice of Tr as the probe beam means that the signal is emitted in the same direction as the vibrational echo and no re-alignment is necessary in any subsequent optics. Temporal overlap between the two beams is set by measuring rising edge of the pump-induced increased absorbance in a semi-conductor material. Typical conversion between vibrational echo and pump-probe experiments can be accomplished in less than 30 minutes.

2.6 REFERENCES

- (1) Jung, I. D.; Kartner, F. X.; Matuschek, N.; Sutter, D. H.; MorierGenoud, F.; Zhang, G.; Keller, U.; Scheuer, V.; Tilsch, M.; Tschudi, T. *Optics Letters* **1997**, *22*, 1009.
- (2) Jung, I. D.; Kartner, F. X.; Matuschek, N.; Sutter, D. H.; MorierGenoud, F.; Shi, Z.; Scheuer, V.; Tilsch, M.; Tschudi, T.; Keller, U. *Applied Physics B: Lasers and Optics* **1997**, *65*, 137.
- (3) Boyd, R. W. *Nonlinear Optics*; Academic Press: San Diego, 1992.
- (4) Allen, L. C.; Eberly, J. H. *Optical resonance and two-level atoms*; Dover Publications, 1987.
- (5) Yariv, A. *Quantum Electronics, 3rd ed.*; John Wiley & Sons, Inc: New York, 1989.
- (6) Mukamel, S. *Principles of Nonlinear Optical Spectroscopy*; Oxford University Press: New York, 1995.
- (7) Hamm, P.; Hochstrasser, R. M. Structure and dynamics of proteins and peptides: Femtosecond two-dimensional infrared spectroscopy. In *Ultrafast Infrared and Raman Spectroscopy*; Fayer, M. D., Ed.; Marcel Dekker, Inc.: New York, 2001; Vol. 26; pp 273.
- (8) Cho, M. "Shonan Lecture Notes", 2000.
- (9) Spence, D. E.; Evans, J. M.; Sleat, W. E.; Sibbet, W. *Optics Letters* **1991**, *16*, 1762.
- (10) Spence, D. E.; Kean, P. N.; Sibbet, W. *Optics Letters* **1991**, *16*, 42.
- (11) Murnane, M. M.; Kapteyn, H. C.; Huang, C.-P.; Asaki, M. T.; Garvey, D. "Designs and Guidelines for Constructing a Mode-locked Ti:sapphire Laser," Washington State University, 1992.
- (12) Rundquist, A.; Durfee, C.; Chang, Z.; Taft, G.; Zeek, E.; Backus, S.; Murnane, M. M.; Kapteyn, H. C.; Christov, I.; Stoev, V. *Applied Physics B: Lasers and Optics* **1997**, *65*, 161.
- (13) Backus, S.; Durfee, C. G.; Murnane, M. M.; Kapteyn, H. C. *Review of Scientific Instruments* **1998**, *69*, 1207.
- (14) Piletic, I. Dynamics of nanoscopic hydrogen bonded systems probed using ultrafast nonlinear infrared spectroscopy., Stanford University, 2006.
- (15) Hamm, P.; Kaindl, R. A.; Stenger, J. *Optics Letters* **2000**, *25*, 1798.
- (16) Asbury, J. B.; Steinel, T.; Fayer, M. D. *J. Luminescence* **2004**, *107*, 271.
- (17) Park, E.; Andrews, S.; Boxer, S. G. *J. Phys. Chem.* **1999**, *103*, 9813.
- (18) Hahn, E. L. *Phys. Rev.* **1950**, *80*, 580.
- (19) Zheng, J. R.; Kwak, K.; Chen, X.; Asbury, J. B.; Fayer, M. D. *Journal of the American Chemical Society* **2006**, *128*, 2977.
- (20) Khalil, M.; Demirdoven, N.; Tokmakoff, A. *Phys. Rev. Lett.* **2003**, *90*, 047401.
- (21) Khalil, M.; Demirdoven, N.; Tokmakoff, A. *J. Phys. Chem. A.* **2003**, *107*, 5258.
- (22) Asbury, J. B.; Steinel, T.; Stromberg, C.; Gaffney, K. J.; Piletic, I. R.; Goun, A.; Fayer, M. D. *Phys. Rev. Lett.* **2003**, *91*, 237402.

- (23) Asbury, J. B.; Steinel, T.; Stromberg, C.; Gaffney, K. J.; Piletic, I. R.; Fayer, M. D. *Journal of Chemical Physics* **2003**, *119*, 12981.
- (24) Ernst, R. R.; Bodenhausen, G.; Wokaun, A. *Nuclear Magnetic Resonance in One and Two Dimensions*; Oxford University Press: Oxford, 1987.
- (25) The total dephasing is overwhelmingly dominated by pure dephasing processes in this system, and would be essentially unaffected by small errors in the second excited state lifetime.
- (26) Fourkas, J. T.; Kawashima, H.; Nelson, K. A. *J. Chem. Phys.* **1995**, *103*, 4393.
- (27) Zheng, J.; Kwak, K.; Xie, J.; Fayer, M. D. *Science* **2006**, 1951.
- (28) Merchant, K. A. *Ultrafast Multidimensional Vibrational Spectroscopy: Theoretical and Experimental Studies on Proteins and Model Compounds*, Stanford University, 2003.
- (29) Massari, A. M.; Finkelstein, I. J.; McClain, B. L.; Goj, A.; Wen, X.; Bren, K. L.; Loring, R. F.; Fayer, M. D. *J. Am. Chem. Soc.* **2005**, *127*, 14279.
- (30) Massari, A. M.; Finkelstein, I. J.; Fayer, M. D. *J. Am. Chem. Soc.* **2006**, *128*, 3990.
- (31) Bai, Y. S.; Fayer, M. D. *Phys. Rev. B.* **1989**, *39*, 11066.

CHAPTER 3: AQUEOUS PROTEIN DYNAMICS

3.1 INTRODUCTION

The previous chapter presented a description of the experimental apparatus and a theoretical framework for the 2D-IR experiments. This chapter will describe the application of 2D-IR spectroscopy, in conjunction with molecular dynamics (MD) simulations, to probe the ultrafast dynamics of several heme proteins in aqueous solutions. In Section 3.3, the 2D-IR method is illustrated by considering the dynamics of myoglobin (Mb), as reported by CO bound at the active site. First, a description of the homodyne detected vibrational echo signal is presented. The homodyne detection strategy was used to measure the dynamics of myoglobin and cytochrome c mutants in the first 2D-IR studies. Section 3.3 concludes by extending the discussion to a description of the heterodyne detection strategy, as applied to the same protein system. Heterodyne detected 2D-IR spectroscopy offers multiple advantages over homodyne detection, making it the current state of the art in the field. Heterodyne detected 2D-IR studies are further described in Chapter 5 of this work.

Myoglobin is a small globular protein that is found in mammalian muscle tissue. The protein reversibly binds exogenous ligands such as O₂, NO, and CO via a prosthetic iron heme group (see Figure 3.1). It has long been realized that aqueous MbCO can adopt several distinct conformations at room temperature.^{1,2} The spectroscopic signature for these structural substates is the multi-peak linear infrared absorption spectrum of the CO stretch,²⁻⁴ which is dominated by three lines denoted, from high to low peak frequency, A₀, A₁, and A₃. A₁ and A₃ are the predominant spectral lines at room temperature and neutral pH. Section 3.3 describes how a comparison of measured and simulated absorption spectra and vibrational echoes showed that the primary structural difference between A₁ and A₃ states could be assigned to a rotation of the singly protonated imidazole group of the distal histidine, H64.⁵⁻⁷



Figure 3.1 The x-ray crystal structure of MbCO (PDB ID: 1DWR). The CO bound heme active site and key histidines H64 (distal) and H93 (proximal) are shown explicitly.

Much of the detailed understanding of myoglobin and its conformational dynamics has come from a combination of simulations and biophysical studies on the native protein and a library of prepared mutants with key modified residues.⁸⁻¹² To further probe the influence of distal residues on the fastest dynamics of Mb, 2D-IR experiments and MD simulations of a distal histidine mutant were undertaken. Section 3.4 presents an investigation of the ultrafast protein dynamics of the CO adduct of a myoglobin mutant with the polar distal histidine replaced by a nonpolar valine (H64V). The protein structural fluctuations have been investigated by spectrally resolved infrared stimulated vibrational echo experiments and MD simulations. In aqueous solution at room temperature, the vibrational dephasing rate of CO in the mutant is reduced by ~50% relative to the native protein. This finding confirms that the dephasing of the CO vibration in the native protein is sensitive to the interaction between the ligand and the distal histidine. The stimulated vibrational echo observable is calculated from MD simulations of H64V within a model in which

vibrational dephasing is driven by electrostatic forces. In agreement with experiment, the calculated vibrational echoes show slower dephasing for the mutant than for the native protein. However, vibrational echoes calculated for H64V do not show the quantitative agreement with measurements demonstrated previously for the native protein.

Section 3.5 presents spectrally resolved infrared vibrational echo studies of several distal modifications to the heme cofactor in two mutated forms of the *Hydrogenobacter thermophilus* (*Ht*) cytochrome *c*₅₅₂. Cytochromes *c* (cyt *c*) are small electron transfer heme proteins that play key roles in respiration and photosynthesis.¹³⁻¹⁵ Due to their wide availability, robust structure, and ease of handling, these proteins have served as model systems to study the interplay of protein structure, dynamics, and function.¹⁶⁻²⁵ In Section 3.5, 2D-IR vibrational echo spectroscopy²⁶ was used to directly measure the active site structural dynamics of two mutated forms of *Ht*-cyt *c*₅₅₂.²⁷⁻²⁹ In both mutants, the heme axial ligand, Met61, was replaced by an alanine (M61A). This allowed a strong IR probe (CO) to be strategically bound to the ferrous heme in place of Met61 to report on the active site dynamics of both proteins. The first mutant (*Ht*-M61A) was characterized by only the single M61A mutation and retained an axial Gln64, which was expected to be oriented out of the heme pocket (see Figure 3.2b) as it is in the native protein.^{27,28,30} The second mutant (*Ht*-M61A/Q64N) was further modified to have Gln64 replaced by an Asn in an effort to generate an active site structure with Asn64 positioned to interact with the heme-bound CO (see Figure 3.2a). The vibrational echo experiments presented in Section 3.5 reveal that the shortest timescale vibrational dephasing of the CO is faster in the *Ht*-M61A/Q64N mutant than in *Ht*-M61A. Longer timescale dynamics, measured as spectral diffusion, are unchanged by the Q64N modification. We conclude that the faster dynamics in *Ht*-M61A/Q64N are due to the location of Asn64, which is a hydrogen bond donor, above the heme-bound CO. The results suggest a general trend for rapid ligand vibrational dynamics in the presence of a hydrogen bond donor.

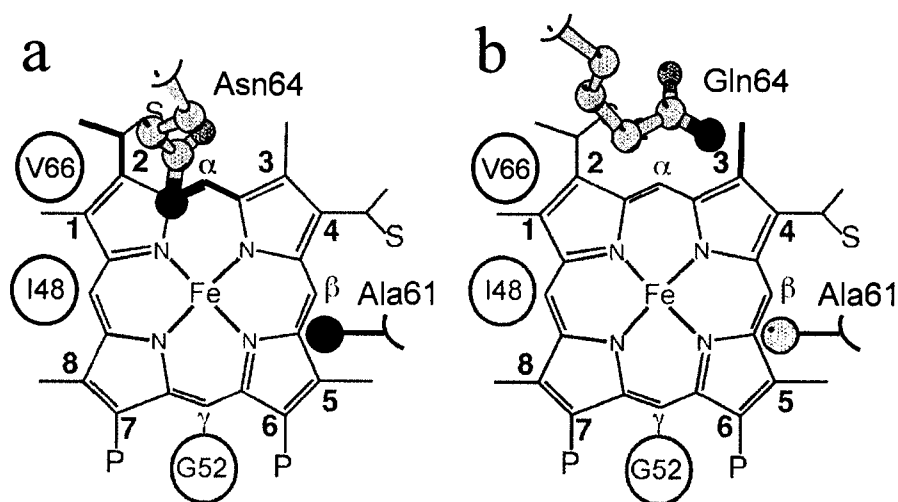


Figure 3.2 The active site structures of *Ht-cyt c*₅₅₂ mutants M61A/Q64N (a) and M61A (b), as determined by 2D NMR.³¹

3.2 MATERIALS AND METHODS

3.2.1 Protein Preparation

Horse heart myoglobin was purchased from Sigma-Aldrich and used without further purification. Purified human myoglobin mutant H64V was provided by Boxer and coworkers³². Preparation of cytochrome c mutants *Ht*-M61A and *Ht*-M61A/Q64N utilized an *E. coli*-based expression system.^{29,33} Molecular biology procedures and materials, and the preparation of *Ht*-M61A are described in detail elsewhere.^{28,34} To prepare *Ht*-M61A/Q64N, the polymerase chain reaction overlap extension method³⁵ was employed using the pSHC552A61 expression plasmid³⁴ as the template. Cloning, expression, and purification of *Ht*-M61A/Q64N was as described for *Ht*-M61A.³⁴

3.2.2 Sample Preparation for Vibrational Echo Spectroscopy.

To prepare aqueous samples of carbonmonoxy bound proteins, ~10 mg of lyophilized protein was dissolved in 1.0 mL pH 7.4 D₂O phosphate buffer (50mM). The buffer pH was measured before addition of protein. The solutions were reduced with a 5-fold excess of dithionite (Sigma-Aldrich) and stirred under a CO atmosphere

for one hour. The solutions were centrifuged at 14,000 rcf for 15 minutes through a 0.45 μm acetate filter (Pall Nanosep MF) to remove particulates. The samples were further concentrated by repeated centrifugation (Eppendorf 5415D) over modified polyethersulfone membranes (Pall Nanosep 3K Omega) to a final protein concentration of 10-15 mM. The sample was then placed in a sample cell with CaF_2 windows and a 50 μm Teflon spacer. UV-visible (Varian Cary 3E) and FT-IR (ATI Mattson Infinity 9495) absorption spectroscopies were performed to determine all protein concentrations. The samples had mid-IR absorbances at the CO stretching frequency of ~ 0.1 on a background absorbance of 0.5.

3.2.3 *Molecular Dynamics Simulations of H64V*

Molecular dynamics (MD) simulations were performed on one molecule of H64V and 3483 rigid TIP3P water molecules³⁶ using the MOIL software package.³⁷ The MOIL force field³⁷ describes covalent interactions with the AMBER potential³⁸, non-bonded interactions with the OPLS potential³⁹, and improper torsions with the CHARMM potential.⁴⁰ Protein and solvent were contained within a 45 \AA x 54 \AA x 61 \AA cell, subject to periodic boundary conditions. The H64V molecule was constructed by attaching a CO ligand to the active site of sperm whale metmyoglobin with mutations H64V and D122N⁴¹, from structure 2MGJ in the Protein Data Bank.⁴² The D122N mutation is far from the active site and is expected to have a negligible effect on the protein structure and dynamics. The protein structure carries a net positive charge, so one chloride ion was added to ensure electroneutrality. After attachment of the ligand, the system's energy was minimized, and the system was heated from 0 K to 300 K at a rate of 1.5K/ps, and then equilibrated at constant temperature, achieved by rescaling particle velocities. After equilibration, the system was simulated at constant energy for 5.9 ns, with $T = 300 \pm 3$ K.

We relate molecular dynamics trajectories to spectroscopic observables with the electrostatic model applied previously to wtMbCO.^{5-7,43,44} In this picture, the force exerted by the local electric field on the electric dipole of the CO induces a shift in the

CO transition frequency. Therefore, the frequency fluctuates in time with the dynamics of the local electric field. This frequency fluctuation is given by:

$$\delta\omega(t) = \lambda \left[\vec{u}(t) \cdot \vec{E}(t) - \langle \vec{u} \cdot \vec{E} \rangle \right] \quad (3.2-1)$$

where $\delta\omega(t)$ is the time-dependent deviation from the mean vibrational frequency of the CO, $\vec{E}(t)$ is the time-dependent electric field calculated at the midpoint of the CO bond, λ is the Stark effect tuning rate, and $\vec{u}(t)$ is a unit vector along the carbon-oxygen bond of the CO. The local electric field was calculated from the partial charges in the MOIL force field, Coulomb's law in vacuum, and the atomic configurations generated by the simulations. The coupling constant λ in Equation (3.2-1) has been measured independently by Boxer and coworkers with vibrational Stark spectroscopy.^{45,46} For wtMbCO and other heme-CO systems, the coupling constant is found to lie in the range $\lambda=1.8-2.2 \text{ cm}^{-1}/(\text{MV}/\text{cm})$.^{45,46} In the previous comparison of calculated and measured vibrational echoes and absorption spectra for wtMbCO, λ was treated as an adjustable parameter, with a best fit value of $\lambda=2.1 \text{ cm}^{-1}/(\text{MV}/\text{cm})$,⁷ consistent with the range of measured values.^{45,46} We fixed the value of $\lambda=2.1 \text{ cm}^{-1}/(\text{MV}/\text{cm})$ in the calculations reported here for H64V. Variation of λ within the experimentally determined range for heme-CO systems does not significantly affect the absorption spectrum or vibrational echo decays. Therefore, the calculation of the observables for H64V is performed without recourse to adjustable parameters. Molecular dynamics trajectories are used to compute the equilibrium autocorrelation function of frequency fluctuations, $C(t)$:

$$C(t) = \langle \delta\omega(0)\delta\omega(t) \rangle \quad (3.2-2)$$

The vibrational echo and absorption spectrum are then determined from $C(t)$ as described in Chapter 2.

3.2.4 FFCF Extraction From Vibrational Echo Data

To extract quantitative information from the vibrational echo decays, nonlinear response theory calculations were compared to the experimental data.^{44,47} Within

conventional approximations,⁴⁷ both the vibrational echo and the linear infrared absorption spectrum are completely determined by the FFCF (see Chapter 2). The FFCF is the starting point from which the experimental observables are calculated. A multi-exponential form of the FFCF, $C(t)$, was used in accordance with previous vibrational echo analysis and MD simulations of heme proteins.^{34,44,48} It is important to note that the exponentials in the FFCF do not give rise to single or multi-exponential vibrational echo decay curves, but rather produce complicated non-exponential decays. The FFCF has the form:

$$C(t) = \Delta_0^2 + \sum_{i=1}^n \Delta_i^2 \exp(-t / \tau_i) \quad (3.2-3)$$

Here, Δ_0 is the contribution from inhomogeneous broadening. Inhomogeneous broadening is caused by variations in protein structure that influence the CO frequency but evolve on timescales that are much slower than the experimental time window. In this study, the structural dynamics that occur on timescales greater than ~ 100 ps will contribute to inhomogeneous broadening. Δ_i is the magnitude of the contribution from a frequency perturbing process with correlation time τ_i . If τ_i is fast compared to Δ_i^{-1} ($\Delta_i \tau_i \ll 1$, Δ in radians/ps) for a given exponential term, then that component of the FFCF is motionally-narrowed.⁴⁹⁻⁵² For a motionally-narrowed term in $C(t)$, the Δ and τ_i cannot be determined independently,³⁴ but a pure dephasing time, T_2^* , can be defined ($T_2^* = (\Delta^2 \tau)^{-1}$), which describes the “homogeneous linewidth” for that component of the FFCF. Although protein dynamics generally occur over a continuum of timescales, a multi-exponential $C(t)$ organizes these fluctuations into experimentally relevant timescales that can be compared from one system to another. The FFCF is used to calculate the linear absorption spectrum and a series of vibrational echo decay curves (τ scanned, T_w fixed) for a range of T_w s. To maximize the efficiency of the empirical fits, delta-function laser pulses were used when fitting the data. A comparison of these fits to those obtained by performing the full three time ordered integrals with the finite length pulse durations verified that the effects of pulse duration were negligibly small given the very short pulses used in the

experiments. The FFCF obtained from analysis of the data using response theory calculations was deemed correct when it could be used to calculate vibrational echo decays that fit the experimental vibrational echo data at all T_w s while simultaneously reproducing the linear absorption spectrum.

3.3 ILLUSTRATION OF THE TECHNIQUE – MYOGLOBIN-CO

3.3.1 *Homodyne Detected Vibrational Echo Spectroscopy*

To illustrate the nature of the 2D-IR method, experiments on the CO bound to the active site of the protein myoglobin is used as an example. Carbonmonoxy-myoglobin (MbCO) has been extensively studied both experimentally^{2,10,31,48,53-58} and computationally.⁵⁹⁻⁶² The CO stretching mode of MbCO has a strong transition dipole, making its infrared absorption an easily monitored experimental observable that can be used to track kinetics and dynamics in the protein. Studies on Mb, and in particular on MbCO, test many of the ideas on the relationship between structure and function in proteins. Figure 3.3 shows the linear FT-IR absorption spectrum of the CO stretch of MbCO. There are three bands labeled A_0 , A_1 , and A_3 that correspond to different configurations of the distal histidine (H64). These bands will be discussed below.

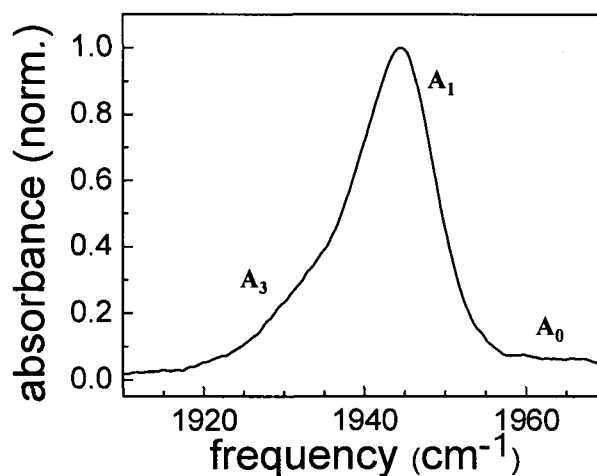


Figure 3.3 The FT-IR absorption spectrum of wild type MbCO.

Figure 3.4 presents the homodyne detected vibrational echo data for MbCO. In the homodyne detected experiment, the echo signal (see Chapter 2) is dispersed through a monochromator onto an infrared array detector. The square-law detector reports the intensity level spectrum of the echo wavepacket. The 2D-IR spectrum is recorded as a function of τ , the delay between input beams 1 and 2, for a fixed T_w , the delay between beams 2 and 3. Thus, for each waiting time, T_w , a 2D spectrum is constructed, with the intensity level vibrational echo spectrum on the horizontal axis and the time-course of the τ decay on the vertical axis. The full 2D vibrational echo spectrum is shown as an inset in Figure 3.4, with several vertical slices through the data at 1930 cm^{-1} (red), 1938 cm^{-1} (black), and 1946 cm^{-1} (blue) shown in the main panel. It is evident from Figure 3.4 that the frequency dependent decay dynamics seen at early waiting times are essentially absent at longer T_w . The spectral features in the $\sim 1930\text{-}1950\text{ cm}^{-1}$ range of the 2D spectrum arise due to the ground state dynamics of the three A_i states of MbCO, and the red-shifted band ($\sim 1900\text{-}1930\text{ cm}^{-1}$) is due to the anharmonically shifted 1-2 transitions of the A_i states. In principle, the vibrational echo signals from the three spectroscopic substates of MbCO are additive at the electric field level. However, since the homodyne detection strategy reports the vibrational echo wavepacket at the intensity level, spectral overlap between the three states ensures that the resulting signal will have significant mixing of the substate dynamics. This complicates analysis of the homodyne signal significantly. In congested spectra, the vibrational echo decay must be considered at multiple frequency slices.

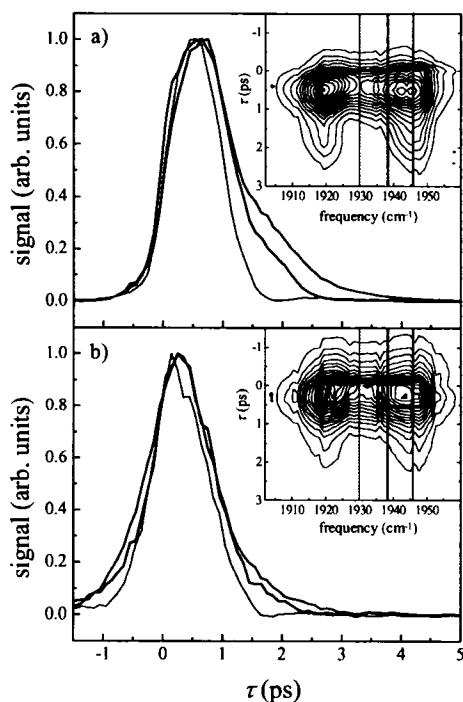


Figure 3.4 Homodyne detected 2D-IR vibrational spectra of wild type MbCO at (a) $T_w = 0$ ps and (b) $T_w = 8$ ps. The inset shows the full 2D-IR vibrational echo signal as a function of emission frequency (horizontal axis) and decay time τ (vertical axis). The main panels show slices through the 2D-IR data at 1946 cm^{-1} (blue), 1938 cm^{-1} (black), and 1930 cm^{-1} (red). Although the data is initially frequency dependent, by $T_w = 8$ ps, the decays are almost frequency independent at long T_w .

The stimulated vibrational echo measures spectral diffusion by varying the T_w delay time. As T_w is increased, it acts as a time gate, allowing dephasing events with longer timescales to influence the vibrational echo curves. A convenient way to analyze the slower timescale dynamics is to plot the vibrational echo peak shift. The vibrational echo peak shift is the difference between the time of peak amplitude of the decay curve and zero time. When longer timescale protein dynamics are present, the echo decays become faster as T_w becomes longer and their peaks shift towards the origin. In the frequency domain (Fourier transform of the vibrational echo decay), the vibrational echo spectrum, the dynamical linewidth broadens with increasing T_w due to protein dynamics that influence the CO frequency on the T_w timescale. A broader

dynamical linewidth (faster vibrational echo decay and smaller peak shift) means that a larger portion of the total possible structural configurations of the protein has been sampled. For long enough T_w , spectral diffusion is complete and all chromophores have sampled the entire spectral line. In this case, the dynamic line shape is equal to the absorption line and the vibrational echo peak shift is zero. However, because the vibrational lifetime limits the timescale of the experiments, it is not possible to observe the slowest timescale motions. These slow dynamics appear static on the vibrational echo timescale.

3.3.2 Heterodyne Detected 2D-IR Echo Spectroscopy

In the heterodyne detected 2D vibrational echo spectrum, there are two frequency axes, which require two Fourier transforms to convert the time structure of the echo observable into 2D frequency data. The vibrational echo pulse, which is spatially overlapped with the local oscillator (LO) pulse, is passed through the monochromator. Taking the spectrum of the pulse performs one of the Fourier transforms and provides the vertical axis in the 2D spectrum, ω_m (m for monochromator, see Figure 3.5b). The other frequency axis is obtained by scanning τ . Scanning τ produces an interferogram (see Figure 3.5a) as the echo pulse changes its phase relationship relative to the fixed LO pulse. There is one interferogram for each frequency on the ω_m axis for which there is signal. The numerical Fourier transforms of the τ scan interferograms provide the ω_τ axis. The data $S(\omega_\tau, \omega_m, T_w)$ are then plotted for each T_w in a three dimensional representation, that is, the amplitude as a function of both ω_τ and ω_m (the ω_1 and ω_3 axes, respectively in 2D NMR). More experimental details of the method including phase error corrections have been presented in detail.^{63,64}

In the 2D-IR spectrum of MbCO (Figure 3.5b) there is a positive going band (red) on the diagonal (dashed line) and a negative going band (blue) off-diagonal. Each contour is a 10% change in amplitude. The positive band on the diagonal reflects the ground state to first vibrationally excited state (0-1 transition) of the CO

stretch of MbCO. The negative going off-diagonal band involves the 1-2 transition. The frequencies of the first interaction of the radiation field (first pulse) with the vibrations are the frequencies on the ω_τ axis. The frequencies of the third interaction (third pulse) with the vibrations, which is also the frequency of the echo emission, is the frequency on the ω_m axis. If $\omega_m = \omega_\tau$, the peak is on the diagonal. This is the situation for the red band in Figure 3.5b (the 0-1 transition).

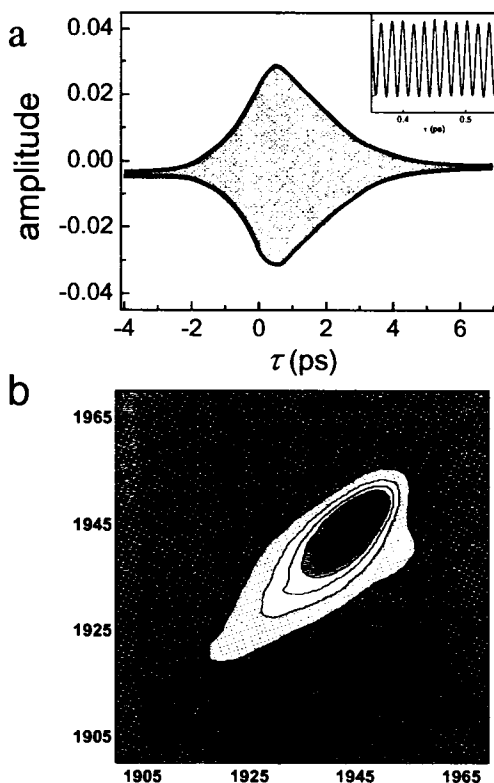


Figure 3.5 (a) A time-domain interference pattern collected in the 2D-IR experiment at the center of the A_1 transition in MbCO. The interferogram is shown in gray and envelope as a solid blue or red line. Positive τ (red envelope) is defined by beam 1 arriving at the sample before beam 2 and negative τ (blue envelope) indicates that beam 2 arrives before beam 1. The optical carrier frequency is clearly visible in the inset. (b) 2D-IR absorptive spectrum of MbCO at $T_w = 0.5$ ps. The positive going bands correspond to 0-1 transitions of the A_1 and A_3 states and negative going bands are the 1-2 transitions, displaced along ω_m by the anharmonicity. The A_0 state is not visible at this contouring level (10%).

The blue off-diagonal 1-2 band arises as follows. The first interaction produces a coherent superposition state of the 0-1 transition. One of the quantum pathways for the second interaction (second pulse) produces a population in the 1 state (first vibrationally excited state). Then the third pulse can couple the 1 state to the 2 state, and produce a coherent superposition of 1 and 2. This results in the vibrational echo being emitted at the 1-2 transition frequency, which is shifted to lower frequency than the 0-1 transition by the vibrational anharmonicity. Therefore, the ω_r frequency is the 0-1 frequency (1945 cm^{-1}), but the ω_m frequency is the 1-2 frequency (1921 cm^{-1}). The off-diagonal anharmonicity peak is negative going because there is a 180° phase shift in the echo pulse electric field relative to the 0-1 echo. The spectrum in Figure 3.5b is for $T_w = 0.5\text{ ps}$, a short time compared to the timescale of protein structural fluctuations in this system. Therefore, spectral diffusion is not complete, and the 0-1 band in the 2D spectrum is elongated along the diagonal and the 1-2 band is elongated along a line parallel to the diagonal. The elongation is the signature of inhomogeneous broadening. However, while the band is dominated by the A_1 peak (see Figure 3.3) there is also some contribution along the diagonal from the A_3 band. With the 10% contours shown, the A_0 band is not visible but can be seen when finer contours are used. As discussed below, the change in shape with increasing T_w measures spectral diffusion, and, thus, the structural evolution of the system. In the heterodyne detected 2D-IR spectra, contributions of the A_i peaks to the 2D spectrum is additive, making it possible to separate and analyzed their respective dynamics independently.

Figure 3.6 displays 2D vibrational echo data for MbCO at four T_w s. The diagonal 0-1 band and the off-diagonal 1-2 band contain essentially the same information. Because the vibrations are nearly harmonic, it can be shown that the 0-1 and 1-2 bands will be nearly identical in their time dependent evolution, which is confirmed by experimental studies. Therefore, only the 0-1 band will be discussed. As T_w increases, the shape of the spectrum changes, going from elongated along the diagonal to essentially round. The change in shape of the bands as T_w is increased

reflects protein structural dynamics. The vibrational echo pulse sequence used to collect 2D-IR spectra displays inhomogeneous broadening along the diagonal and dynamic broadening along the anti-diagonal (shown as dashed lines in the upper left panel of Figure 3.6).⁶⁵ At short T_w the 2D dynamic line shape has significant inhomogeneous broadening, which manifests itself as elongation along the diagonal. As T_w is increased, the experiment picks up longer timescale protein dynamics that increases the anti-diagonal width and decreases the diagonal width, but to a lesser extent than the change in the anti-diagonal. In the long time limit, all protein fluctuations contribute to the 2D spectrum, which would lead to a 2D-IR shape with equal diagonal and anti-diagonal linewidths.

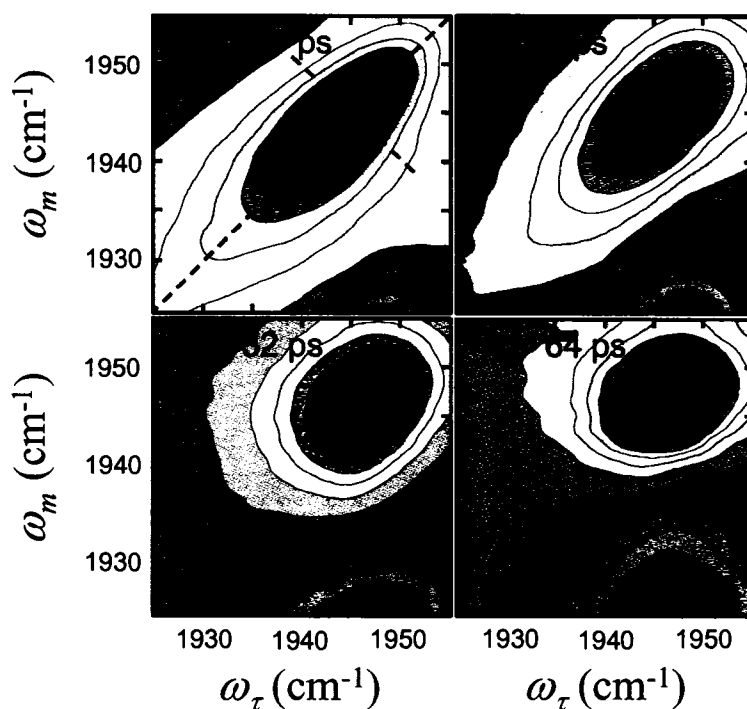


Figure 3.6 A series of 2D-IR spectra for MbCO as a function of increasing T_w . Only the 0-1 transition is shown and the data is presented at 10% contour levels. Dashed lines through the top left panel indicate the diagonal (long line) and anti-diagonal (short line) slice through the center of the A_1 peak.

To analyze the time evolution of the 2D spectrum, the full 2D band shapes are used. It is convenient to discuss the time evolution of 2D spectral band shapes by defining the eccentricity, ε ,

$$\varepsilon(T_w) = \sqrt{1 - \frac{\sigma_{AD}^2(T_w)}{\sigma_D^2(T_w)}} \quad (3.3-1)$$

where σ_{AD} and σ_D are the band widths along the anti-diagonal and diagonal slices, respectively. This definition for the eccentricity displays several convenient limits. In the case of large inhomogeneous broadening, $\sigma_{AD} \ll \sigma_D$, and $\varepsilon \rightarrow 1$. At longer T_w s, slower timescale protein dynamics contribute to the anti-diagonal width, causing the eccentricity to decay to zero. In the long time limit in which all protein structures have been sampled, $\varepsilon \rightarrow 0$. The eccentricity is a convenient way to succinctly summarize protein dynamics contained in the 2D-IR spectra. The full 2D spectral shapes are used in fitting the data.

Figure 3.7a shows the diagonal of the 2D vibrational echo spectrum at $T_w = 0.5$ ps with the diagonal spectrum decomposed into the three peaks, which are fit as Gaussians. It has been found in the study of several heme proteins that the band shapes are well described as Gaussians. However, as discussed below, the quantitative analysis does not assume a particular line shape. The eccentricity of the A_1 state as a function of T_w is shown in Figure 3.7b. It was determined by measuring the antidiagonal width at the peak frequency and subtracting the contribution to the width from the overlapping A_3 state, which was measured on the red side of the band. The eccentricity of the A_1 state of MbCO decays as a biexponential. As discussed immediately below, there is actually a third, T_w independent component in the 2D signal that arises from fast, motionally narrowed protein dynamics that is revealed in the full analysis of the data.

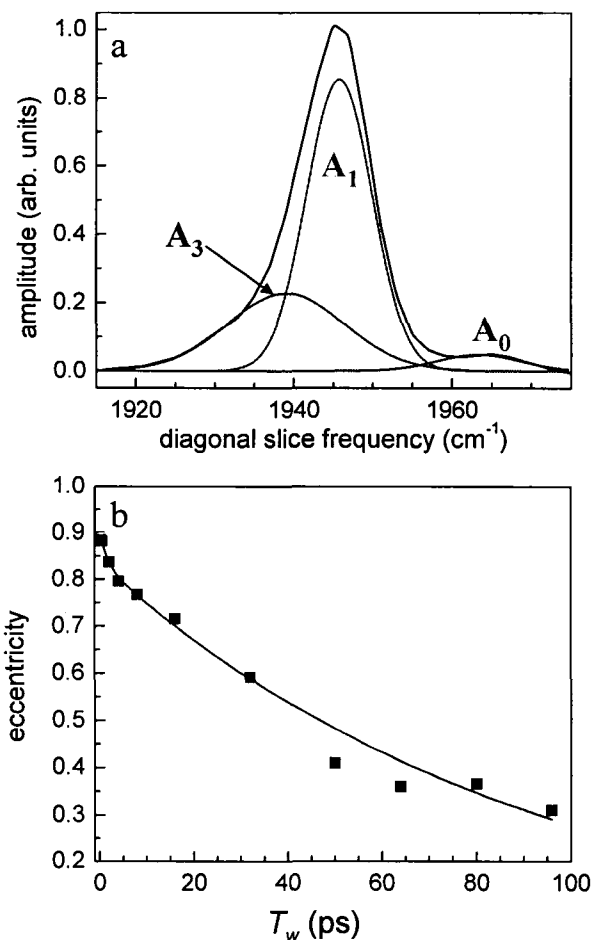


Figure 3.7 (a) Normalized diagonal slice through the 2D-IR data for MbCO at $T_w = 0.5$ ps. The spectrum is fit to three Gaussian lines, centered at the center frequencies of the A bands in MbCO. (b) Eccentricity of the A_1 substate of MbCO. The line through the data is a bi-exponential fit.

3.3.3 The Frequency-Frequency Correlation Function

A quantitative description of the amplitudes and timescales of CO frequency fluctuations is provided by the frequency-frequency correlation function (FFCF).^{5,44,47,48,66,67} Structural fluctuations give rise to frequency fluctuations. The FFCF is the probability that a molecule with frequency ω at time $t = 0$, still has frequency ω at some later time averaged over the complete ensemble of molecules. As time increases, molecules sample an increasingly wide range of frequencies, and the FFCF decays. At sufficiently long time, all accessible structures are sampled, and

all frequencies in the absorption line are sampled as well. Therefore, the FFCF decays to zero.

Within standard approximations, both the linear absorption spectrum and the 2D-IR vibrational echo spectra at all T_w can be simultaneously calculated with the appropriate FFCF (see Section 3.2.4).⁴⁷ FFCFs were obtained from the data by iterative fitting using response theory calculations.^{47,66} The FFCF was deemed correct when it could be used to simultaneously reproduce the 2D-IR spectra (homodyne or heterodyne detected) at all T_w , and the linear absorption spectrum. Such calculations can also reproduce the T_w dependence of the eccentricity.

From studying the dynamics of MbCO and combining the results with molecular dynamics simulations, it was possible to determine the structures of the A_1 and A_3 substates.⁴⁴ It has been well documented that the A_0 state has the distal histidine swung out of pocket that contains the active iron heme site.^{68,69} It was also known that the A_1 and A_3 states have the distal histidine in the pocket. However, these structures interconvert too quickly to be studied using other techniques such as NMR. Using the vibrational echo experiments, the FFCFs of both the A_1 and A_3 states were determined. The results were then compared to MD simulations. However, it was first necessary to develop a method to calculate the ultrafast vibrational echo observables from a classical MD simulation of MbCO.⁵

Figure 3.8 shows a schematic illustration of how the protein structural fluctuations influence the CO transition frequency via the vibrational Stark effect. The method uses the MD simulations to determine the fluctuating electric field along the CO transition dipole. The electric field fluctuations are caused by the motions of all of the groups in the proteins that carry partial charges, as prescribed by the MOIL potential. The simulation produces the time dependent fluctuating electric field, depicted as red field lines in Figure 3.8. These electric fields couple to the CO transition dipole moment (blue arrow in Figure 3.8) via the time-dependent Stark effect.

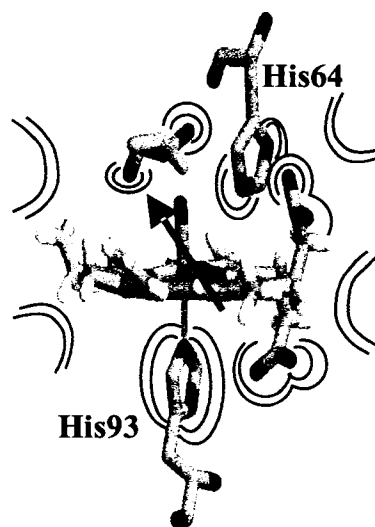


Figure 3.8 A schematic illustration of the active site of MbCO. Time dependent electric fields (red field lines) arising from structural fluctuations of charged groups within the protein create a macroscopic time dependent electric field (blue arrow) at the midpoint of the CO bond. The CO transition frequency is modulated by this electric field via the Stark effect.

Figure 3.9a shows a portion of a frequency trajectory obtained from one run of the MD simulation.⁴⁴ The FFCF is calculated from the time dependent frequency shift. Then the FFCF obtained from the MD simulations is used as an input in the same diagrammatic perturbation calculations used to fit the 2D-IR data. The agreement between the simulations and the experiments was found to be excellent.⁴⁴ As can be seen in Figure 3.9a, the nature of the fluctuations in the frequency periodically changes. By comparison with experiment, it was possible to identify the segments of the MD trajectory when the protein is in either the A_1 or A_3 state. It was, therefore, also possible to identify the points in time when the transitions occurred between the two structural substates. These are indicated in Figure 3.9a. This is the key point. Once it was known that a transition between substates had occurred, the MD simulation was examined to determine the nature of the structural changes at the transition points.

Figure 3.9b shows the results for the structural determination of the A_1 and A_3 states based on the combined vibrational echo experiments and the MD simulation.⁴⁴

The structural change is primarily a rotation about the distal histidine's C_{β} - C_{α} bond. The dihedral angle changes by $\sim 40^{\circ}$. The distance from the protonated nitrogen N_{ϵ} -H to the CO is $\sim 5 \text{ \AA}$ in the A_1 state but only $\sim 3 \text{ \AA}$ in the A_3 state. Thus, the vibrational echo experiments not only provided insights into the dynamics of the protein but also provided the necessary observables enabling the solution of a long standing structural problem.

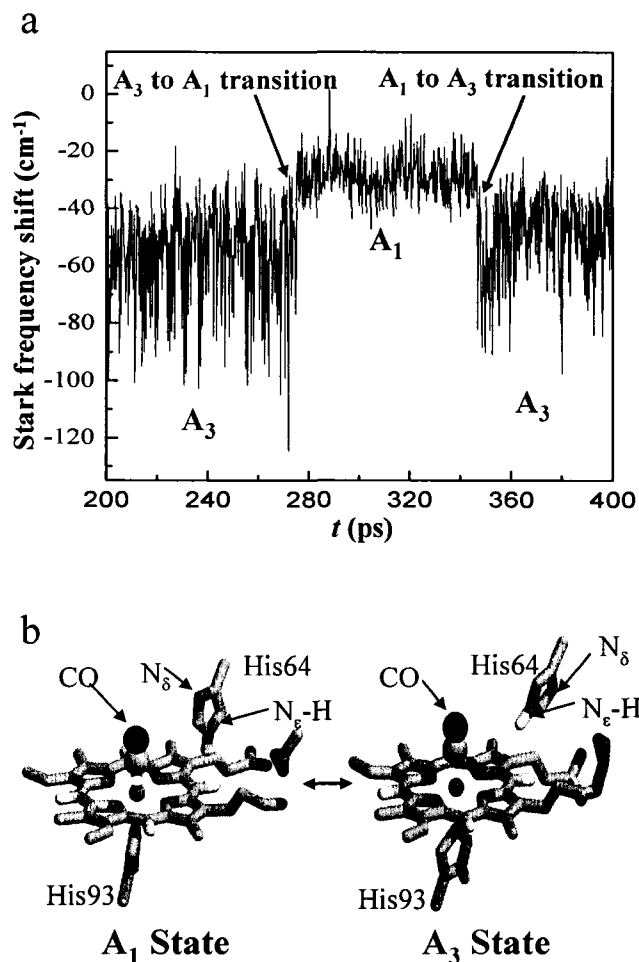


Figure 3.9 (a) The time dependent Stark frequency shift taken from a segment of an MD simulation of MbCO. Discontinuous steps in the Stark shift signal structural interconversion between the A_1 and A_3 states of MbCO (b).

3.4 DYNAMICS OF MYOGLOBIN WITHOUT THE DISTAL HISTIDINE

3.4.1 *Vibrational Echo Spectroscopy*

The background subtracted linear absorption spectrum of CO bound to the active site of H64V is plotted in Figure 3.10. The H64V spectrum is well fit by a Gaussian function centered at 1968.5 cm^{-1} with a FWHM of 9.5 cm^{-1} . In contrast, Figure 3.3 shows that the spectrum of wtMbCO consists of at least three distinct absorption lines, centered at 1934 cm^{-1} (A_3), 1945 cm^{-1} (A_1), and 1965 cm^{-1} (A_0).^{1,2,44} The A_0 peak, the smallest of the three features at room temperature and neutral pH, is believed to arise from configurations in which the ligand interacts most weakly with H64 because the distal histidine is swung out of the pocket.^{68,70-73} As has been discussed in detail previously, substitution of the distal histidine (H64) by a valine spectroscopically mimics the A_0 state of wtMbCO.

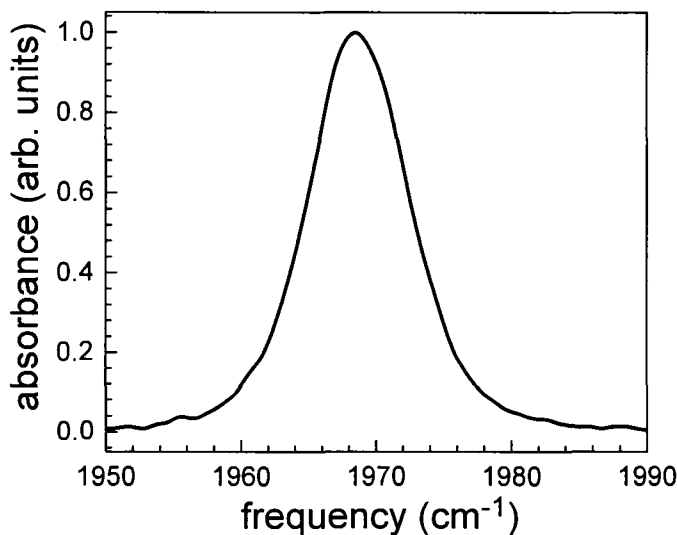


Figure 3.10 The background subtracted linear absorption spectrum of the CO stretch of H64V. The absorption line is well fit by a single Gaussian function centered at 1968.5 cm^{-1} with a FWHM of 9.5 cm^{-1}

Spectrally resolved infrared vibrational echo data for CO bound to H64V is presented in Figure 3.11. The normalized vibrational echo data are plotted as a function of τ for a series of T_w . The vibrational echo signal is spectrally resolved and

a full 2D-IR spectrum is acquired (as in Figure 3.4). Figure 3.11 plots a slice through the vibrational echo spectrum corresponding to the center of the H64V absorption spectrum, 1968.5 cm^{-1} , at several values of T_w . As T_w is increased, the decay becomes faster. In previous experiments on wtMbCO, separating contributions from the three wtMbCO substates required analyzing many wavelengths.⁴⁴ For H64V, no additional information is obtained by analyzing different wavelengths. However, spectral resolution is necessary to avoid contributions from the 1-2 vibrational transition.⁷⁴

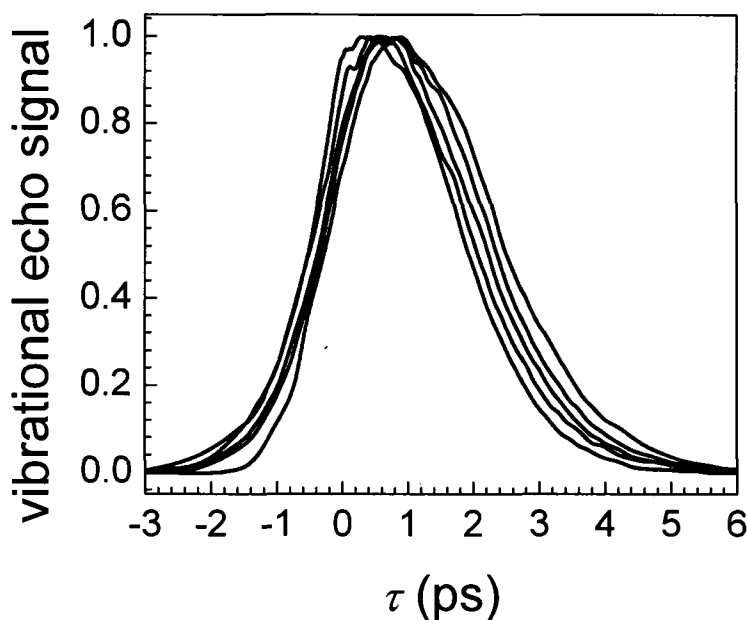


Figure 3.11 The vibrational echo decay curves of H64V taken at the center frequency of the CO stretch absorption (1968 cm^{-1}) are plotted as a function of τ for $T_w = 0.5 \text{ ps}$, 2 ps , 4 ps , 8 ps , and 16 ps . The echo decays get faster and the curve maximum shifts towards the origin with increasing T_w .

At short T_w , H64V exhibits a large peak shift of almost 1 ps. In contrast, wtMbCO has a very small peak shift at early T_w . This indicates that even at short T_w , the wtMbCO chromophores have nearly sampled the entire linear line shape while the H64V chromophores have sampled only a small fraction of the available frequencies, and therefore, only a small fraction of the structural configurations. By $T_w = 16 \text{ ps}$, the A_1 state of myoglobin has a peak-shift nearly equal to zero, whereas the H64V maintains a significant peak shift of 0.5ps; the H64V stimulated vibrational echo decays have only shifted $\sim 40\%$ of the way towards the asymptotic limit. These results

indicate that spectral diffusion is significantly slower in H64V relative to the A_1 and A_3 substates in wtMbCO.^{44,75} The dynamic population of chromophores in wtMbCO has nearly sampled the entire range of accessible spectral frequencies in a very short time, while the H64V chromophores do not completely sample the available spectrum by the longest T_w that was measurable in this study.

Figure 3.12 shows the substantial qualitative difference in the vibrational echo decays of H64V relative to those of the A_1 band of wtMbCO. The solid curve is the spectrally resolved vibrational echo decay collected at the center of the H64V absorption line for a T_w of 2 ps. The dashed curve presents the spectrally resolved vibrational echo decay collected at the center of the wtMbCO A_1 absorption line at the same T_w . The H64V decays are ~50% slower than those of the A_1 state of wtMbCO for all experimentally acquired values of T_w . Previously, it has been shown that the A_1 state dephasing dynamics of wtMbCO are significantly slower than those of the A_3 state.^{6,7,44} At neutral pH, the steady-state concentration of the A_0 substate is very low, precluding a detailed analysis of its dynamics. The dashed curve in Figure 3.12 represents the slowest measurable decay for wtMbCO under physiological conditions.

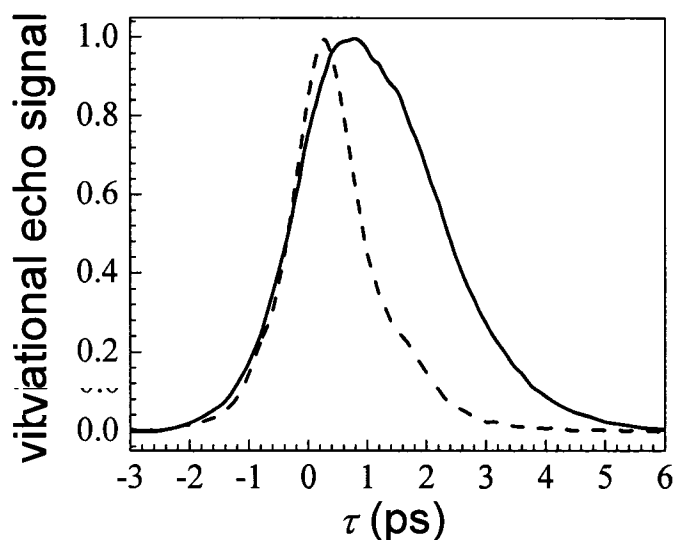


Figure 3.12 The vibrational echo decay curves of H64V (solid curve) compared to the A_1 state of wtMbCO (dashed curve). The echo signal is taken at the center frequency of the CO stretch absorption (1968 cm^{-1} for H64V, 1945 cm^{-1} for wtMbCO) and for $T_w = 2\text{ ps}$. The wtMbCO dynamics are significantly faster than those of H64V.

The vibrational echo decay curves and linear absorption spectrum of H64V were simultaneously fit with a biexponential plus a constant frequency-frequency correlation function, according to Equation (3.2-3). An example of the excellent agreement between the fit (dashed curve) and experimental data (solid curve) is presented in Figure 3.13. The inset shows the measured and calculated linear absorption spectrum, and the body of the figure shows the vibrational echo decay for $T_w = 2$ ps. The experimental observables calculated from $C(t)$ that best fit both the linear absorption spectrum and vibrational echo data are nearly indistinguishable from the measured data on this plot. Excellent simultaneous agreement was achieved for all measured values of T_w (not shown). The experimentally determined FFCF provides a quantitative measure of protein dynamics and serves as another link between experimental observables and MD simulations.

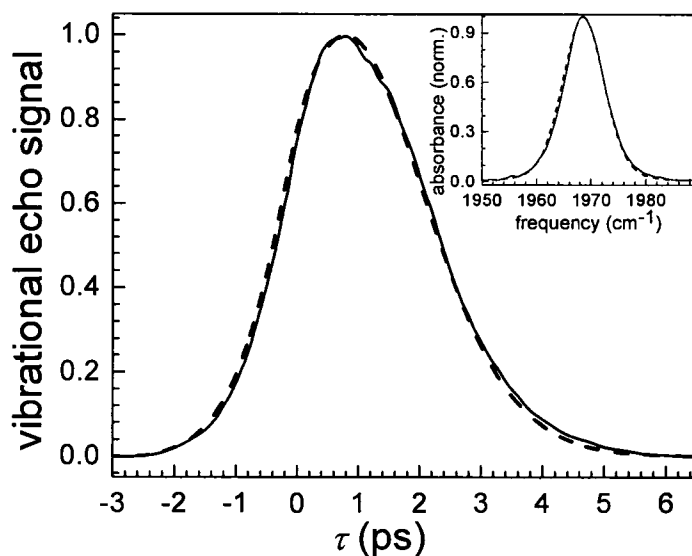


Figure 3.13 A comparison of the experimental H64V data (solid curves) and a fit to all spectroscopic data with an experimentally determined $C(t)$ (dashed curves). Figure body: a representative example of the agreement between measured H64V vibrational echo data and fit for $T_w = 2$ ps. Inset: the linear absorption spectrum of H64V (solid curve) and fit to the data (dashed curve) obtained from an experimentally determined FFCF.

3.4.2 MD Simulations of the H64V Dynamics

Figure 3.14 shows a comparison of the experimental observables calculated from molecular dynamics simulations and the experimental data. The body of the figure displays the vibrational echo for $T_w = 2$ ps, with simulation results given by the solid curve and experimental data shown by the dashed curve. The inset shows the linear absorption spectrum. Again, the solid curve is calculated from molecular dynamics simulation, and the experimental spectrum is the dashed curve. The simulations have no adjustable parameters. The simulated spectrum is 20% too broad while the simulated vibrational echo decay at this and all other T_w values is $\sim 50\%$ too fast. Given the complexity of the calculations to obtain real experimental observables and the absence of adjustable parameters, the agreement between the simulations and the data is reasonably good.

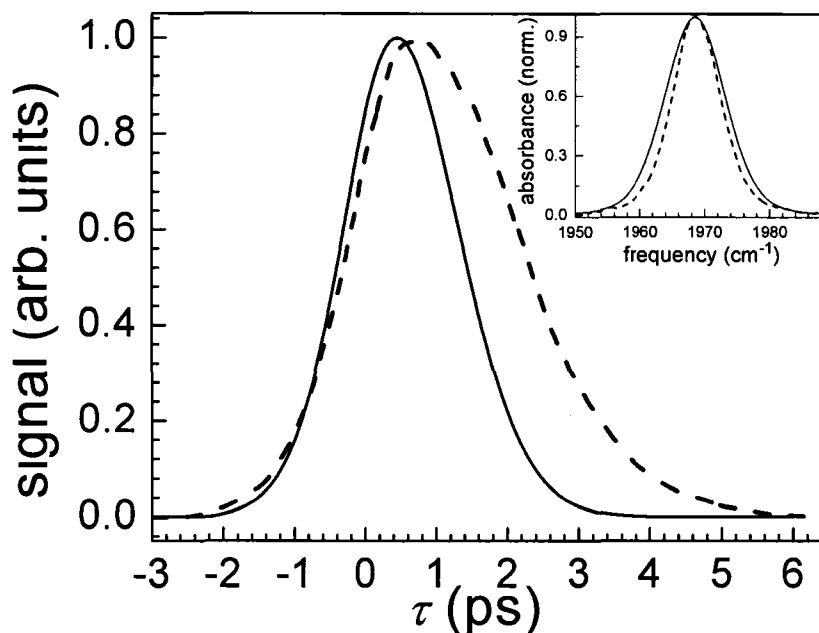


Figure 3.14 A comparison of the measured and simulated linear and vibrational echo signals. **Figure body:** the vibrational echo decay curve of H64V (dashed curves) taken at the center frequency of the CO stretch absorption (1968 cm⁻¹) re-plotted for comparison with the vibrational echo decays calculated from the MD simulation (solid curve). The decays are plotted as a function of τ for $T_w = 2$ ps. **Inset:** the background subtracted, experimentally measured linear absorption spectrum of H64V (dashed curve). The linear absorption spectrum calculated from MD simulations is shown as the solid curve. The lack of quantitative agreement between experiment and simulation is discussed in the text.

Another observable that can provide some information on the nature of the discrepancies between experiment and simulation is the vibrational echo peak shift. The significance of the vibrational echo peak shift and its relation to spectral diffusion was previously discussed. The spectrally resolved peak shift can be calculated directly from the FFCF,⁷⁶⁻⁷⁸ providing another comparison between calculated and measured dynamics. Figure 3.15a plots the vibrational echo peak shifts vs. T_w obtained from the simulated FFCF (solid line) and from the experimentally fit FFCF (dashed line). The black squares are the peak shifts measured from the spectrally resolved vibrational echo data. The experimental $C(t)$ yields peak shifts that are in good agreement with the experimental data, confirming the relation between FFCF and echo peak shift. The simulated peak shift at $T_w = 0$ is within ~10% of the measured value. This demonstrates that at short T_w both simulations and experimental data show that the chromophore has sampled a small percentage of its available spectral frequencies. The simulated FFCF produces peak shifts that decay far too fast. However, it is instructive to examine the derivative of the peak shift with respect to T_w , which is shown in Figure 3.15b. The simulated and experimental derivative curves are nearly identical by $T_w \sim 5$ ps. The results show that the simulation properly accounts for the underlying dynamics that give rise to spectral diffusion after a few ps. The most severe deviations between experiment and simulation are observed at short times, suggesting that the lack of success in simulating the vibrational echo decay curves is caused by a failure to reproduce the dynamical contribution to the observables in the first few ps.

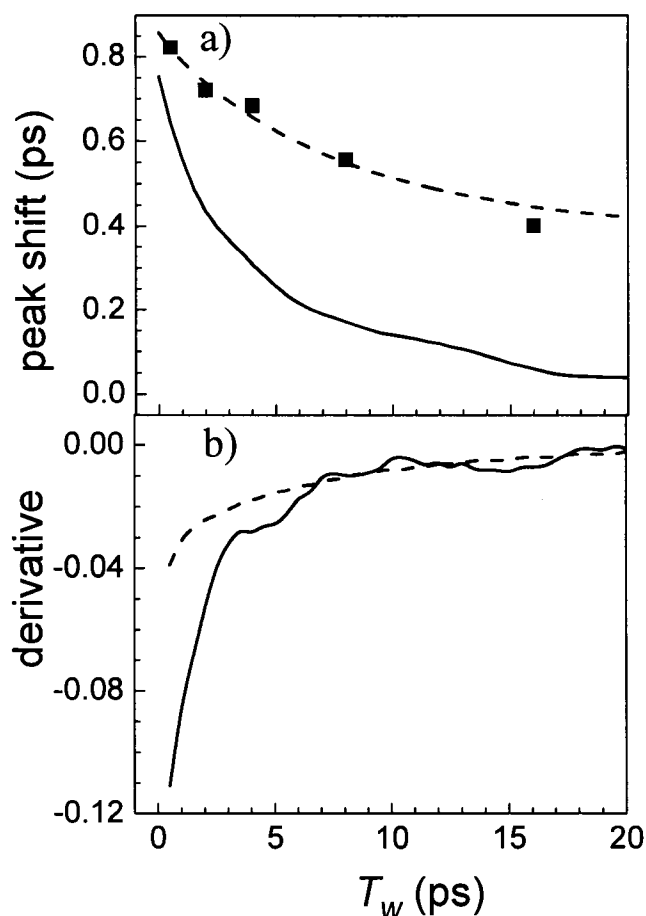


Figure 3.15 (a) Vibrational echo peak shifts calculated from the FFCF obtained by fitting the experimental data (dashed curve) and from the FFCF obtained from the simulation (solid curve). The squares plot experimentally measured peak shift values. (b) The derivative of the peak shift curves with respect to T_w . The dashed curve corresponds to the peak shifts obtained from the experimental FFCF, and the solid curve to the peak shifts obtained from the simulated FFCF. For $T_w > \sim 5$ ps, the curves coincide demonstrating that the simulated and experimental spectral diffusion are the same.

It is not difficult to understand why the analysis of H64V does not show perfect agreement with experimental data. The calculation of the vibrational echo from molecular dynamics trajectories rests on a foundation of numerous approximations previously described.⁴⁴ In particular, the CO vibration is assumed to interact with its surroundings through the classical electric field generated by the point charges of an empirical potential. The potential is constructed primarily to reproduce structural rather than dynamical properties. There is no inclusion of electronic

polarizabilities in the force field for either the protein or the solvent. In addition to the direct coupling of the fluctuating electric field to CO frequency, it might be necessary to include other contributions, e. g., it is possible that fluctuations in the back bonding from the heme π molecular orbitals into the CO π^* antibonding orbitals need to be taken into account.^{70,79} Given this list of approximations, the agreement seen between the simulations and the H64V data is quite reasonable.

In previous experiments and simulation on wtMbCO, virtually perfect agreement between experiment and simulation of both the A₁ and A₃ conformational substates of Mb was achieved.⁴⁴ Connecting MD simulations to spectroscopic observables required one adjustable parameter, the Stark constant λ . However, the value that gave the best fits fell within the error bars of the measurement of this parameter.^{45,46} An important question is why did the wtMbCO simulations provide significantly better agreement with experiment than did the simulations of H64V? To examine the question, we consider the FFCFs of wtMbCO and H64V that were determined by molecular dynamics simulation. The simulated FFCF for H64V, $C(t)$, is shown in Figure 3.16a. The inset is an expanded view of the short time portion. The decay of $C(t)$ for H64V more closely resembles that of A₁ than that of A₃ state in wtMbCO. The A₃ state has the protonated N_ε of the imidazole ring of H64 pointed at and very close to the CO.⁴⁴ This relatively strong interaction, which might be considered a hydrogen bond, should have a major influence on the local dynamics. This is borne out by the larger mean square frequency fluctuations which gives rise to substantially more rapid dephasing of the A₃ state compared to the A₁ state.⁴⁴ Therefore, we will compare H64V to the A₁ state, which has H64 in close proximity to the CO, but without the strong direct interaction associated with the A₃ state.

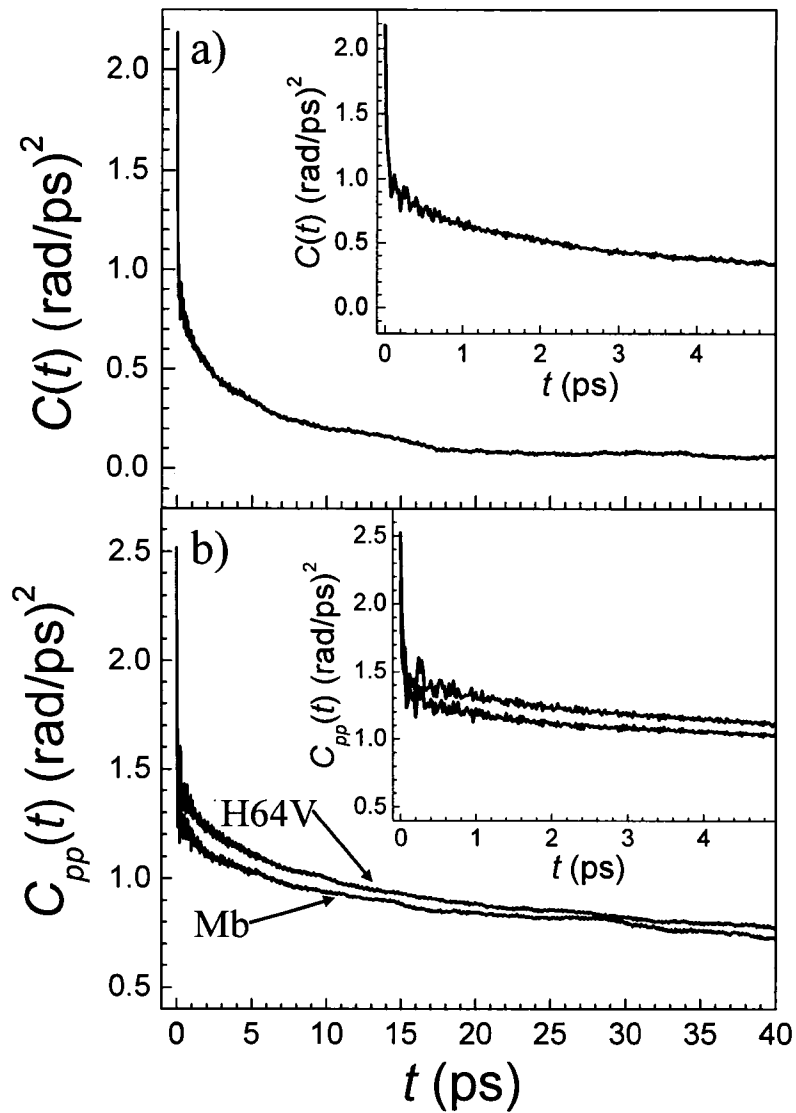


Figure 3.16 (a) The total frequency autocorrelation function, $C(t)$, calculated from an MD simulation of H64V. A Stark tuning constant value of $\lambda=2.1 \text{ cm}^{-1}/(\text{MV}/\text{cm})$ was used in the MD calculated $C(t)$. (b) The frequency autocorrelation function of fluctuations arising from only the protein atoms, $C_{pp}(t)$. The top curve shows $C_{pp}(t)$ for H64V, the bottom curve shows $C_{pp}(t)$ for the A_1 state of wtMbCO. The insets in both figures show the early time behavior of $C(t)$.

The frequency fluctuations in the electrostatic model are proportional to the local electric field fluctuations at the CO ligand, and can be decomposed into contributions from different groups in the protein and solvent. For example, for wtMbCO, we can write the frequency fluctuation of the CO vibration as

$$\delta\omega(t) = \delta\omega_p(t) + \delta\omega_{\text{H64}}(t) + \delta\omega_s(t) \quad (3.4-1)$$

with $\delta\omega_p(t)$ the frequency fluctuation induced by the electric field exerted on the CO by the protein and heme excluding H64, $\delta\omega_{H64}(t)$ the contribution from the distal histidine, and $\delta\omega_s(t)$ the contribution from the solvent. $C(t)$ may then be decomposed into a sum of auto and cross-correlation functions associated with these electric fields. $C_{pp}(t) = \langle \delta\omega_p(0)\delta\omega_p(t) \rangle$, the autocorrelation function of fluctuations of the CO frequency induced by the electric field of the protein, excluding H64 and solvent, is shown by the bottom curve for the A_1 state of wtMbCO in Figure 3.16b. The top curve shows $C_{pp}(t)$ for H64V, and is nearly identical to the A_1 result. The small difference in the offset makes virtually no difference in calculated observables. From Figure 3.16b it is clear that the protein contribution to the experimental observables in the H64V simulations is virtually identical to the protein contribution without the H64 in the simulation of wtMbCO. Furthermore, the comparison demonstrates that the protein-induced electric field at CO in the A_1 state of wtMbCO is nearly equal to the sum of the protein-induced field in H64V and an uncorrelated contribution from H64.⁴⁴ The nonpolar distal valine was determined to make a negligible contribution to the FFCF of H64V in these simulations.

The remaining contribution to the electric field at the CO in Equation (3.4-1) comes from the water solvent. In the simulations of H64V and of wtMbCO, the TIP3P water model³⁶ was employed. As a check, the H64V simulations were run with the SPC⁸⁰ water potential. Changing the water model produced an insignificant difference in the calculated vibrational echo curves.

As shown in Figure 3.15, the error in the FFCF calculated for H64V occurs at relatively short times (< a few ps) for which the simulation produces too much dephasing. Figure 3.15b, shows that the longer time portion of the FFCF is relatively accurate. The proposition that the H64V simulation produces too rapid dephasing is born out by a comparison to the experimentally determined FFCF. The simulated and experimentally determined $C(t)$ share similar subpicosecond decays. However, the experimentally determined $C(t)$ includes a term that is static on the timescale that influences the vibrational echo decays (< ~ 100 ps), Δ_0^2 , which was required to fit the

absorption spectrum. As a vibrational echo experiment is designed to remove the effects of static line broadening, the calculated vibrational echo is relatively insensitive to the presence of this static term. No comparable effectively static process occurs in the simulated $C(t)$, which nearly decays to zero on the timescale of 50 ps. The net result is that the experimentally determined FFCF has a slow component that is static on the timescale of the experiments while the simulated FFCF does not display this component. This comparison to the experimentally determined FFCF together with Figure 3.15b demonstrates that the H64V simulation produces too much dephasing on the ~ 10 ps timescale.

The simulated FFCF of the A_1 state of wtMbCO is approximately equal to a sum of FFCFs from the distal histidine and from the rest of the protein and solvent. This observation, along with the fact that the FFCF of H64V closely resembles the A_1 FFCF from wtMbCO with the contribution of H64 suppressed (Figure 3.16b), suggests a possible explanation for the lack of perfect agreement between the H64V simulations and experiment that is found for wtMbCO as follows: The protein plus solvent contribution to the simulation produces too much dephasing resulting in calculated H64V vibrational echo decays that are too fast and a line width that is too wide. Previous analysis of wtMbCO showed that the distal histidine plays a major role in the fastest timescales of CO dephasing of both the A_1 and A_3 states of the native protein. These facts strongly suggest that the remarkable agreement found in wtMbCO is due to a cancellation of errors. The protein plus solvent contribution produces too much dephasing while the distal histidine, H64, produces too little. In going from wtMbCO to H64V, H64 is removed, and the cancellation of errors ceases.

3.5 CYTOCHROME C_{552} ACTIVE SITE MUTANTS

3.5.1 *Linear IR spectroscopy*

The background subtracted linear FT-IR spectra of the CO bound to *Ht*-M61A and *Ht*-M61A/Q64N are shown in Figure 3.17. The spectrum of *Ht*-M61A (solid line) shows a single transition at 1974 cm^{-1} with a FWHM of 14.7 cm^{-1} , while *Ht*-

M61A/Q64N (dashed line) exhibits a single transition at 1965 cm^{-1} with a FWHM of 16.8 cm^{-1} . The red shifting of the CO stretching frequency of *Ht*-M61A/Q64N relative to *Ht*-M61A is reminiscent of the IR spectrum of aqueous MbCO, which exhibits three primary CO stretching peaks corresponding to three structurally distinct conformational substates (see Figure 3.3).^{2-4,7,44,48,81,82} In the case of MbCO, the inclusion of a polar, hydrogen bond donating residue inside the heme pocket results in a spectral shift of the CO stretch to lower frequencies (see Section 3.3). Comparing this example to the spectra of *Ht*-M61A and *Ht*-M61A/Q64N, the observed red spectral shift caused by replacing Gln64 with an Asn implies that the Gln may be located out of the active site (as does His64 in the MbCO A₀ substate) whereas the Asn is directed into the heme pocket (MbCO A₁ or A₃ substate). According to the electrostatic force model,^{5,44} the motions of a charged moiety in the vicinity of the heme-bound CO should dramatically affect the vibrational dynamics of this chromophore. However, the Gaussian shape of the spectral bands in *Ht*-M61A and *Ht*-M61A/Q64N suggests that these transitions are inhomogeneously broadened, which would obscure any dynamical information contained in the linear spectra. The vibrational stimulated echo experiments described below confirm that the spectral bands are indeed inhomogeneously broadened, and, therefore, that such experiments are necessary to uncover the underlying dynamics.

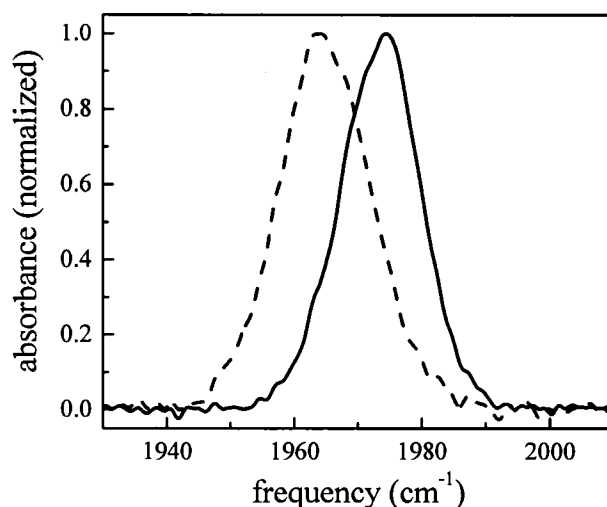


Figure 3.17 Normalized FT-IR spectra of the CO stretching mode bound to *Ht*-M61A (solid line) and *Ht*-M61A/Q64N (dashed line).

3.5.2 Stimulated Vibrational Echo Spectroscopy

Figure 3.18 shows the vibrational echo decays for *Ht*-M61A (solid curve) and *Ht*-M61A/Q64N (dashed curve) at $T_w = 0.5$ ps. The decay of *Ht*-M61A/Q64N is noticeably faster than that of *Ht*-M61A, indicating that the CO dephases faster when Gln64 is replaced by Asn64. For clarity, we focus our attention here on a single T_w , however, this trend is consistent at all values of T_w . In vibrational echo experiments, a faster rate of dephasing indicates that the frequency of the heme-bound CO is fluctuating more rapidly. Within the electrostatic force model described above, structural fluctuations produce motions of charged and polar residues that induce the largest changes in CO transition frequency. The dynamic response of these two proteins as measured by vibrational echo spectroscopy confirms the implications of the linear IR spectra discussed above. The increased fluctuations of the CO frequency are consistent with the structural picture in which Asn64 in *Ht*-M61A/Q64N is localized near the CO, whereas the Gln64 in *Ht*-M61A is directed out of the active site.

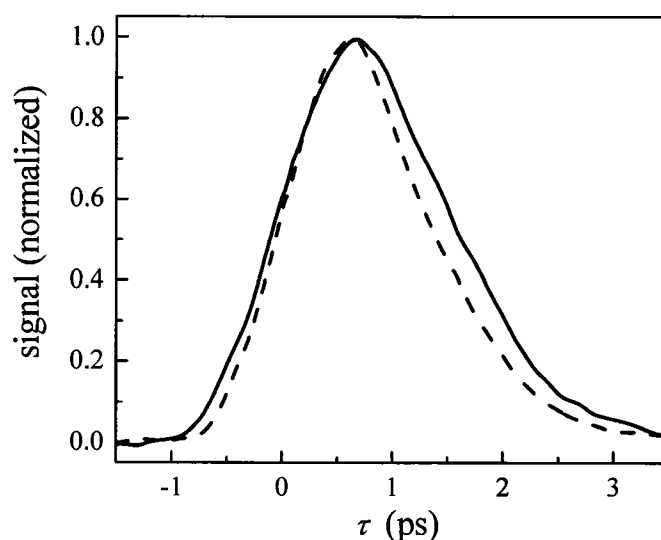


Figure 3.18 Spectrally-resolved vibrational echo decays at $T_w = 0.5$ ps for CO bound to *Ht-M61A* (1975 cm^{-1} , solid line) and *Ht-M61A/Q64N* (1965 cm^{-1} , dashed line).

The vibrational echo peak shifts for *Ht-M61A* and *Ht-M61A/Q64N* are shown in Figure 3.19 as a function of T_w . The peak shift values for *Ht-M61A/Q64N* (filled circles) are consistently smaller than those for *Ht-M61A* (filled squares). This shows that for each T_w time delay, the CO bound to *Ht-M61A/Q64N* has sampled a greater fraction of the spectral line, which is consistent with the faster dephasing. This is shown at a single T_w in Figure 3.18. The fact that the vibrational echo decay peaks have not shifted to zero by $T_w = 16$ ps demonstrates that the full range of protein dynamics affecting the CO frequency have not occurred within this time frame; not all protein configurations that influence the frequency of the CO vibrational transition have been accessed. In these experiments, fluctuations on times greater than ~ 50 ps appear as inhomogeneous broadening, which is accounted for by the Δ_0 term in the FFCF. Aside from the nearly constant offset between the data for these two mutants (Figure 3.19), the peak shifts for both proteins as a function of T_w have the same qualitative shape. The protein dynamics, as sensed by the heme-bound CO, that occur on timescales longer than a few ps qualitatively appear to be unaffected by replacing the Gln64 in *Ht-M61A* with the Asn64 in *Ht-M61A/Q64N*. This indicates that the

primary influence of Asn64 on the CO dynamics occurs on the timescale of a few ps or faster.

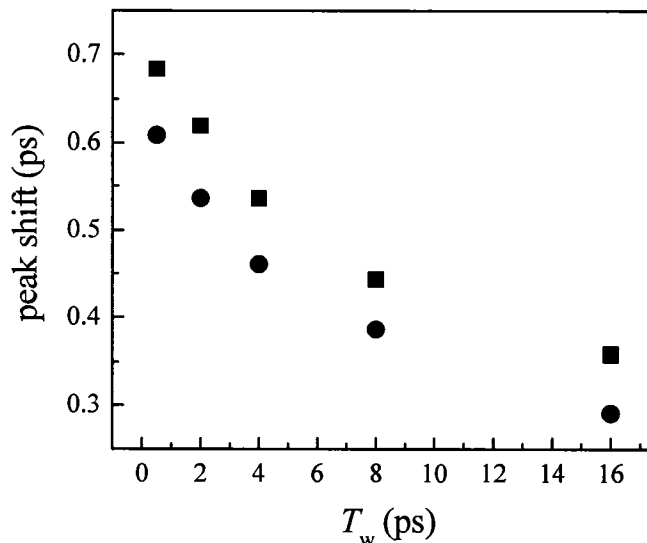


Figure 3.19 Vibrational echo peak shifts as a function of T_w for *Ht-M61A* (filled squares) and *Ht-M61A/Q64N* (filled circles).

To compare the structural dynamics of these two proteins quantitatively, the FFCF for each protein was obtained by simultaneous fits that reproduced the FT-IR absorption spectrum and the vibrational echo decay curves at all T_w values using the procedure described in Section 3.2.4. An example of the quality of the fits obtained using the five adjustable parameters in the biexponential FFCFs is shown for the vibrational echo decay at $T_w = 2$ ps and the linear IR spectrum for *Ht-M61A* in Figure 3.20. The linear absorption spectrum is very sensitive to the constant, Δ_0 , because its width and shape are determined by both the dynamic and inhomogeneous contributions to the spectrum. The shapes of the vibrational echo curves and their change in shape with T_w are very sensitive to the other parameters.

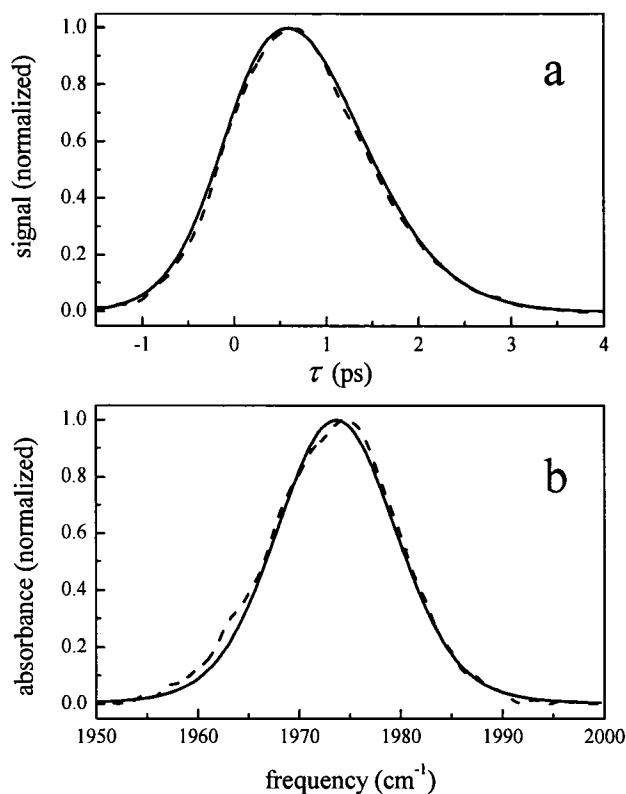


Figure 3.20 a) Experimental vibrational echo decay data at $T_w = 2$ ps and b) linear spectrum for *Ht-M61A* (dashed lines) overlaid with the best-fit vibrational echo decay and linear spectrum calculated from nonlinear response theory (solid lines) at 1975 cm^{-1} .

The FFCF of *Ht-M61A/Q64N* is characterized by a larger Δ_0 than *Ht-M61A*, which shows that some, but not all, of the increase in linear linewidth shown in Figure 3.17 is due to an increase in inhomogeneous broadening. The first exponential term in the FFCFs for both proteins have correlation times (τ_1) that are very fast (hundreds of fs). However, these components are very near the boundary of motional narrowing ($\Delta\tau \ll 1$),⁴⁹⁻⁵² at which point the Δ and τ cannot be determined independently.³⁴ In this near-motionally-narrowed regime, it is reasonable to believe that the relative timescale of the τ_1 s is correct, while the precise value of each τ_1 is not well-defined. To compare the relative dynamics encompassed by the first exponential terms in the FFCFs for *Ht-M61A/Q64N* and *Ht-M61A*, it is instructive to express this near-motionally-narrowed component of the FFCF as a pure dephasing time (T_2^*), which

depends on both Δ_1 and τ_1 . The T_2^* values for *Ht*-M61A/Q64N and *Ht*-M61A are 2.9 and 4.1 ps, respectively. That the dephasing dynamics represented by this first exponential component of $C(t)$ are over 40% faster for *Ht*-M61A/Q64N than *Ht*-M61A is consistent with the faster vibrational echo decay shown in Figure 3.18. Likewise, the similar longer timescale dynamics shown for these two mutants in Figure 3.19 is reflected in the second exponential component of their FFCFs. Since this component of $C(t)$ is not motionally-narrowed, both the magnitude (Δ_2) and correlation time (τ_2) are quantitatively correct and can be used to describe both the vibrational echo and linear IR data. The extracted FFCFs show that the CO frequency fluctuations that occur on longer timescales (tens of ps) for *Ht*-M61A/Q64N and *Ht*-M61A are characterized by very similar, but not identical, Δ_2 s and τ_2 s. This supports the similar shapes of the vibrational echo peak shift data. The fundamental dynamical difference imparted by replacing Gln64 with Asn64 is an increase in dephasing on the hundreds of fs timescale, while the CO frequency fluctuations on the tens of ps timescale are virtually unchanged.

In light of the structural characterization of *Ht*-M61A and *Ht*-M61A/Q64N by NMR,³¹ the comparison of these *Ht*-cyt c_{552} mutants to MbCO and its variants can now be elaborated. As described above, the linear IR spectra of *Ht*-M61A and *Ht*-M61A/Q64N appeared to correspond structurally to the MbCO A_0 and A_1 or A_3 conformational substates, respectively. The NMR results clearly indicate that the structural analogy is valid: *Ht*-M61A and the A_0 substate are characterized by residue 64 directed out of the heme pocket, while this residue is positioned within the pocket above the heme iron in *Ht*-M61A/Q64N and the A_1 and A_3 substates. In general, these data indicate that the inclusion of a polar hydrogen bond donating residue above the heme ring has a noticeable effect on the active site dynamics. For comparison to the *Ht*-cyt c_{552} mutant dephasing dynamics shown in Figure 3.18, the spectrally-resolved vibrational echo decays for MbCO at the A_1 (dashed curve) and A_3 (solid curve) substates are presented in Figure 3.21. Due to spectral overlap of all three spectroscopic lines in MbCO, the echo data for these substates are complicated by

accidental degeneracy beats (ADB).⁸³ Fortunately, the FFCF extraction procedure described earlier allows the vibrational echo decays for each substate to be recalculated, as shown by the A_1 and A_3 echo decays in Figure 3.21, without the influence of the other states. The low intensity of the A_0 substate precludes the acquisition of data at this frequency, however, a MbCO mutant in which H64 has been replaced by a valine (H64V) has been shown to represent the CO vibrational dynamics that correspond to this substate (see above).⁴⁸ The vibrational echo decay for H64V (dotted curve), representing the A_0 substate decay, is overlaid in Figure 3.21 with the decays for the A_1 and A_3 substates (all decays shown at $T_w = 0.5$ ps).

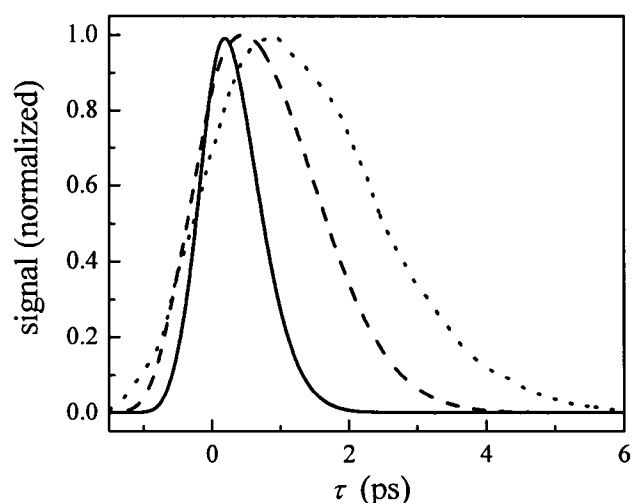


Figure 3.21 Spectrally-resolved vibrational echo decays at $T_w = 0.5$ ps for CO bound to MbCO at the A_3 (1938 cm^{-1} , solid line) and A_1 (1944 cm^{-1} , dashed line) conformational substates. The vibrational echo decay at $T_w = 0.5$ ps for the H64V mutant is overlaid (1968 cm^{-1} , dotted line) and represents the echo decay from the A_0 substate in MbCO.

It is apparent in Figure 3.21 that the dephasing of the A_3 substate is faster than the A_1 substate,^{6,7,44} which in turn dephases faster than the A_0 substate. The fundamental difference between the A_1 and A_3 structures lies in the rotation of the singly protonated imidazole ring on His64. The N_ϵ -H proton and N_δ of this imidazole ring are equidistant from the CO ligand in the A_1 substate, whereas the N_ϵ -H proton is directed toward the CO ligand in the A_3 substate.^{7,44} In the A_3 geometry, the direction of the hydrogen bond donating group (N_ϵ -H proton) toward the heme-bound CO could

provide an additional source of dephasing and generate the faster vibrational echo decay in Figure 3.21. It is important to recognize that *Ht-cyt c₅₅₂* and MbCO are different proteins within the general category of heme proteins, and their overall dynamic ranges are quite different. Nonetheless, the relative magnitude of the change of dephasing rate from *Ht-M61A* to *Ht-M61A/Q64N* is more similar to that of the MbCO A₀ relative to the A₁ substate, rather than A₀ to A₃. While this is admittedly pushing the limitations of the analogy, the similarity of *Ht-M61A/Q64N* dynamics (relative to *Ht-M61A*) to the A₁ substate could suggest that the hydrogen bonding amine group on Asn64 is rotated away from the CO ligand to some degree. To unambiguously identify the atomic displacements responsible for the vibrational dynamics measured in these experiments, calculation of the vibrational echo data from molecular dynamics simulations are required.

That the dynamical trends of *Ht-M61A* and *Ht-M61A/Q64N* are similar to those of the conformational substates of MbCO is an intriguing result. In the case of MbCO, His64 has been implicated in the physiologically crucial differentiation between CO and O₂ binding to the heme group of myoglobin and hemoglobin.^{41,70,84,85} The sensitivity of the active site dynamics for MbCO to the geometry and dynamics of residue 64 suggests that an amino acid residue positioned to interact with heme axial ligands also has a profound effect on the functionality of the active site of cyts *c*. This hypothesis has been recently supported by dynamical studies on *Ht-cyt c₅₅₂* and *Ht-M61A/Q64N*.^{27,28} It is plausible that the presence of Gln64 in the active site of *Ht-cyt c₅₅₂* instead of the Asn64 found in most other cyts *c₈* affords a unique physiological function that is beneficial to that species. The current study reveals a dynamical difference imparted by Gln64 on the ps timescale, and shows that, in addition to affecting slower structural motions, single site mutations in naturally occurring proteins can also influence dynamical processes. Fast structural fluctuations can be the precursors to slower timescale structural changes.

3.6 CONCLUDING REMARKS

A protein's function is defined by its structural architecture and the evolution of that architecture with time. To understand, alter, or mimic the function of a protein or enzyme, it is necessary to understand the roles that specific residue motions play in determining the physiological reactivity of the active site. The full compliment of 2D-IR experiments and MD simulations presented here is a powerful methodology for probing the ultrafast dynamics of protein in thermal equilibrium. Studies on wtMbCO and a distal mutant have established the importance of the distal residues on the dynamics as measured by the CO transition frequency. It was shown that the vibrational Stark effect provides a quantitative comparison between classical MD simulations and quantum spectroscopic observables. Although vibrational echo decays and MD simulations for wtMbCO were found to be in excellent agreement, experiments on H64V were only in qualitative agreements.

Vibrational echo studies on *Ht-cyt. c₅₅₂* mutants revealed that the rate of dephasing (ps timescale) of the heme-bound CO in *Ht-M61A/Q64N* is significantly faster than for *Ht-M61A*, while the rate of spectral diffusion (tens of ps timescale) is nearly identical for the two mutants. This implies that the crucial residues surrounding the active site of a protein or enzyme could be optimized to satisfy the specific needs of an organism without significantly altering the longer timescale structural dynamics that typically involve movements of larger domains. We conclude that the faster dynamics on the ps timescale measured in *Ht-M61A/Q64N* are due to the geometry of Asn64, which is a hydrogen bond donor that localizes above the heme-bound CO. A similar interaction between residue 64 and the CO ligand has been observed for MbCO and its H64V variant. These examples suggest a general trend toward rapid active site dynamics when in the presence of a hydrogen bond donor, and represent a mechanism by which an organism might impart a unique selectivity to substrate binding or reactivity at the active site of a protein or enzyme.

3.7 REFERENCES

- (1) Makinen, M. W.; Houtchens, R. A.; Caughey, W. S. *Proc. Natl. Acad. Sci. USA* **1979**, *76*, 6042.
- (2) Caughey, W. S.; Shimada, H.; Choc, M. C.; Tucker, M. P. *Proc. Natl. Acad. Sci. USA* **1981**, *78*, 2903.
- (3) Li, T. S.; Quillin, M. L.; Phillips, G. N., Jr.; Olson, J. S. *Biochemistry* **1994**, *33*, 1433.
- (4) Anderton, C. L.; Hester, R. E.; Moore, J. N. *Biochim. Biophys. Acta* **1997**, *1338*, 107.
- (5) Williams, R. B.; Loring, R. F.; Fayer, M. D. *J. Phys. Chem. B* **2001**, *105*, 4068.
- (6) Merchant, K. A.; Thompson, D. E.; Xu, Q.-H.; Williams, R. B.; Loring, R. F.; Fayer, M. D. *Biophys. J.* **2002**, *82*, 3277.
- (7) Merchant, K. A.; Noid, W. G.; Thompson, D. E.; Akiyama, R.; Loring, R. F.; Fayer, M. D. *J. Phys. Chem. B* **2003**, *107*, 4.
- (8) Henry, E. R.; Sommer, J. H.; Hofrichter, J.; Eaton, W. A. *Journal of Molecular Biology* **1983**, *166*, 443.
- (9) Martin, J. L.; Vos, M. H. *Methods in Enzymology* **1994**, *232*, 416.
- (10) Morikis, D.; Champion, P. M.; Springer, B. A.; Sligar, S. G. *Biochemistry* **1989**, *28*, 4791.
- (11) Balasubramanian, S.; Lambright, D. G.; Simmons, J. H.; Gill, S. J.; Boxer, S. G. *Biochem.* **1994**, *33*, 8355.
- (12) Ostermann, A.; Waschipsky, R.; Parak, F. G.; Nienhaus, G. U. *Nature* **2000**, *2000*, 205.
- (13) Moore, G. R.; Pettigrew, G. W. *Cytochromes c. Evolutionary, structural, and physicochemical aspects*; Springer-Verlag: Berlin - Heidelberg - New York, 1990.
- (14) Wilson, M. *in Cytochrome c: A multidisciplinary approach*; University Science Books: Sausalito, CA, 1996.
- (15) Mathews, F. S. *Prog. Biophys. Molec. Biol.* **1985**, *45*, 1.
- (16) Pan, L. P.; Hibdon, S.; Liu, R. Q.; Durham, B.; Millett, F. *Biochemistry* **1993**, *32*, 8492.
- (17) Bai, Y. W. *Proc. Natl. Acad. Sci. USA* **1999**, *96*, 477.
- (18) Mines, G. A.; Pascher, T.; Lee, S. C.; Winkler, J. R.; Gray, H. B. *Chemistry and Biology* **1996**, *3*, 491.
- (19) Bjerrum, M. J.; Casimiro, D. R.; Chang, I. J.; Dibilio, A. J.; Gray, H. B.; Hill, M. G.; Langen, R.; Mines, G. A.; Skov, L. K.; Winkler, J. R.; Wuttke, D. S. *J. Bioenerg. and Biomem.* **1995**, *27*, 295.
- (20) Winkler, J. R.; Malmstrom, B. G.; Gray, H. B. *Biophys. Chem.* **1995**, *54*, 199.
- (21) Bryngelson, J. D.; Onuchic, J. N.; Socci, N. D.; Wolynes, P. G. *Proteins-Structure Function and Genetics* **1995**, *21*, 167.

- (22) Geren, L. M.; Beasley, J. R.; Fine, B. R.; Saunders, A. J.; Hibdon, S.; Pielak, G. J.; Durham, B.; Millett, F. *J. Biol. Chem.* **1995**, *270*, 2466.
- (23) Sosnick, T. R.; Mayne, L.; Hiller, R.; Englander, S. W. *Nature Struct. Biol.* **1994**, *1*, 149.
- (24) Raphael, A. L.; Gray, H. B. *Journal of the American Chemical Society* **1991**, *113*, 1038.
- (25) Bren, K. L.; Kellogg, J. A.; Kaur, R.; Wen, X. *Inorganic Chemistry* **2004**, *43*, 7934.
- (26) Lim, M.; Hamm, P.; Hochstrasser, R. M. *Proc. Natl. Acad. Sci. USA* **1998**, *95*, 15315.
- (27) Zhong, L.; Wen, X.; Rabinowitz, T. M.; Russell, B. S.; Karan, E. F.; Bren, K. L. *Proc. Natl. Acad. Sci. USA* **2004**, *101*, 8637.
- (28) Wen, X.; Bren, K. L. *Biochemistry* **2005**, *44*, 5225.
- (29) Karan, E. F.; Russell, B. S.; Bren, K. L. *J. Biol. Inorg. Chem.* **2002**, *7*, 260.
- (30) Travaglini-Allocatelli, C.; Gianni, S.; Dubey, V. K.; Borgia, A.; Di Matteo, A.; Bonivento, D.; Cutruzzola, F.; Bren, K. L.; Brunori, M. *Journal of Biological Chemistry* **2005**, *280*, 25729.
- (31) Massari, A. M.; McClain, B. L.; Finkelstein, I. J.; Lee, A. P.; Reynolds, H. L.; Bren, K. L.; Fayer, M. D. *J. Phys. Chem. B* **2006**, *110*, 18803.
- (32) Hill, J. R.; Dlott, D. D.; Rella, C. W.; Peterson, K. A.; Decatur, S. M.; Boxer, S. G.; Fayer, M. D. *J. Phys. Chem.* **1996**, *100*, 12100.
- (33) Fee, J. A.; Chen, Y.; Todaro, T. R.; Bren, K. L.; Patel, K. M.; Hill, M. G.; Gomez-Moran, E.; Loehr, T. M.; Ai, J.; Thöny-Meyer, L.; Williams, P. A.; Stura, E.; Sridhar, V.; McRee, D. E. *Protein Sci.* **2000**, *9*, 2074.
- (34) Massari, A. M.; Finkelstein, I. J.; McClain, B. L.; Goj, A.; Wen, X.; Bren, K. L.; Loring, R. F.; Fayer, M. D. *J. Am. Chem. Soc.* **2005**, *127*, 14279.
- (35) Ho, S. N.; Hunt, H. D.; Horton, R. M.; Pullen, J. K.; Pease, L. R. *Gene* **1989**, *77*, 51.
- (36) Jorgensen, W. L.; Chandrasekhar, J.; Madura, J. D.; Impey, R. W.; Klein, M. L. *J. Chem. Phys.* **1983**, *79*, 926.
- (37) Elber, R.; Roitberg, A.; Simmerling, C.; Goldstein, R.; Li, H.; Verkhivker, G.; Keaser, C.; Zhang, J.; Ulitsky, A. *Comput. Phys. Commun.* **1994**, *91*, 159.
- (38) Weiner, S. J.; Kollman, P. A.; Case, D. A.; Singh, U. C.; Ghio, C.; Alagona, G.; Profeta, S.; Weiner, P. *J. Am. Chem. Soc.* **1984**, *106*, 765.
- (39) Jorgensen, W. L.; Tirado-Rives, J. *J. Am. Chem. Soc.* **1984**, *106*, 765.
- (40) Brooks, B. R.; Bruccoleri, R. E.; Olafson, B. D.; States, D. J.; Swaminathan, S.; Karplus, M. *J. Comput. Chem.* **1983**, *4*, 187.
- (41) Quillin, M. L.; Arduini, R. M.; Olson, J. S.; Phillips, G. N., Jr. *J. Mol. Biol.* **1993**, *234*, 140.
- (42) Berman, H. M.; Westbrook, J.; Feng, Z.; Gilliland, G.; Bhat, T. N.; Weissig, H.; Shindyalov, I. N.; Bourne, P. E. *Nucleic Acids Research* **2000**, *28*, 235.
- (43) Williams, R. B.; Loring, R. F. *J. Chem. Phys.* **2000**, *113*.

- (44) Merchant, K. A.; Noid, W. G.; Akiyama, R.; Finkelstein, I.; Goun, A.; McClain, B. L.; Loring, R. F.; Fayer, M. D. *J. Am. Chem. Soc.* **2003**, *125*, 13804.
- (45) Park, E.; Andrews, S.; Boxer, S. G. *J. Phys. Chem.* **1999**, *103*, 9813.
- (46) Park, E. S.; Boxer, S. G. *J. Phys. Chem. B* **2002**, *106*, 5800.
- (47) Mukamel, S. *Principles of Nonlinear Optical Spectroscopy*; Oxford University Press: New York, 1995.
- (48) Finkelstein, I. J.; Goj, A.; McClain, B. L.; Massari, A. M.; Merchant, K. A.; Loring, R. F.; Fayer, M. D. *J. Phys. Chem. B* **2005**, *109*, 16959.
- (49) Berg, M. A.; Rector, K. D.; Fayer, M. D. *J. Chem. Phys.* **2000**, *113*, 3233.
- (50) Kubo, R. A stochastic theory of line-shape and relaxation. In *Fluctuation, Relaxation and Resonance in Magnetic Systems*; Ter Haar, D., Ed.; Oliver and Boyd: London, 1961.
- (51) Kubo, R. In *Fluctuation, Relaxation, and Resonance in Magnetic Systems*; Haar, D. T., Ed.; Oliver and Boyd: London, 1962.
- (52) Schmidt, J.; Sundlass, N.; Skinner, J. *Chem. Phys. Lett.* **2003**, *378*, 559.
- (53) Ansari, A.; Berendzen, J.; Braunstein, D.; Cowen, B. R.; Frauenfelder, H.; Hong, M. K.; Iben, I. E. T.; Johnson, J. B.; Ormos, P.; Sauke, T. B.; Scholl, R.; Schulte, A.; Steinbach, P. J.; Vittitow, J.; Young, R. D. *Biophys. Chem.* **1987**, *26*, 337.
- (54) Rector, K. D.; Fayer, M. D. *Laser Chem.* **1999**, *19*, 19.
- (55) Tian, W. D.; Sage, J. T.; Champion, P. M.; Chien, E.; Sligar, S. G. *Biochemistry* **1996**, *35*, 3487.
- (56) Phillips, G. N., Jr.; Teodoro, M. L.; Li, T.; Smith, B.; Olson, J. S. *J. Phys. Chem. B* **1999**, *103*, 8817.
- (57) Fayer, M. D. *Ann. Rev. Phys. Chem.* **2001**, *52*, 315.
- (58) Oldfield, E.; Guo, K.; Augspurger, J. D.; Dykstra, C. E. *J. Am. Chem. Soc.* **1991**, *113*, 7537.
- (59) Rovira, C.; Schulze, B.; Eichinger, M.; Evanseck, J. D.; Parrinello, M. *Biophys. J.* **2001**, *81*, 435.
- (60) Elber, R.; Karplus, M. *Science* **1987**, *235*, 318.
- (61) Vitkup, D.; Ringe, D.; Petsko, G. A.; Karplus, M. *Nature Struct. Bio.* **2000**, *7*, 34.
- (62) Kushkuley, B.; Stavrov, S. S. *Biophysical Journal* **1997**, *72*, 899.
- (63) Khalil, M.; Demirdoven, N.; Tokmakoff, A. *Phys. Rev. Lett.* **2003**, *90*, 047401.
- (64) Asbury, J. B.; Steinel, T.; Fayer, M. D. *J. Luminescence* **2004**, *107*, 271.
- (65) Roberts, S. T.; Loparo, J. J.; Tokmakoff, A. *J. Chem. Phys.* **2006**, *125*, 084502.
- (66) Mukamel, S. *Ann. Rev. Phys. Chem.* **2000**, *51*, 691.
- (67) Hamm, P.; Hochstrasser, R. M. Structure and dynamics of proteins and peptides: Femtosecond two-dimensional infrared spectroscopy. In *Ultrafast Infrared and Raman Spectroscopy*; Fayer, M. D., Ed.; Marcel Dekker, Inc.: New York, 2001; Vol. 26; pp 273.
- (68) Tian, W. D., Sage, J. T., Champion, P. M. *J. Mol. Bio.* **1993**, *233*, 155.

- (69) Braunstein, D. P.; Chu, K.; Egeberg, K. D.; Frauenfelder, H.; Mourant, J. R.; Nienhaus, G. U.; Ormos, P.; Sligar, S. G.; Springer, B. A.; Young, R. D. *Biophysical Journal* **1993**, *65*, 2447.
- (70) Rovira, C. *Journal of Molecular Structure (THEOCHEM)* **2003**, *632*, 309.
- (71) Johnson, J. B.; Lamb, D. C.; Frauenfelder, H.; Müller, J. D.; McMahon, B.; Nienhaus, G. U.; Young, R. D. *Biophys. J.* **1996**, *71*, 1563.
- (72) Yang, F.; Phillips, G. N., Jr. *J. Mol. Biol.* **1996**, *256*, 762.
- (73) Zhu, L.; Sage, J. T.; Rigos, A. A.; Morikis, D.; Champion, P. M. *J. Mol. Biol.* **1992**, *224*, 207.
- (74) Finkelstein, I. J.; McClain, B. L.; Fayer, M. D. *J. Chem. Phys.* **2004**, *121*, 877.
- (75) Rector, K. D.; Rella, C. W.; Kwok, A. S.; Hill, J. R.; Sligar, S. G.; Chien, E. Y. P.; Dlott, D. D.; Fayer, M. D. *J. Phys. Chem. B.* **1997**, *101*, 1468.
- (76) Tan, H.-S.; Piletic, I. R.; Riter, R. E.; Levinger, N. E.; Fayer, M. D. *Phys. Rev. Lett.* **2005**, *94*, 057405.
- (77) Cho, M. H.; Yu, J. Y.; Joo, T. H.; Nagasawa, Y.; Passino, S. A.; Fleming, G. R. *J. Chem. Phys.* **1996**, *100*, 11944.
- (78) Passino, S. A.; Nagasawa, Y.; Joo, T.; Fleming, G. R. *J. Phys. Chem. A* **1997**, *101*, 725.
- (79) Ray, G. B.; Li, X.-Y.; Ibers, J. A.; Sessler, J. L.; Spiro, T. G. *J. Am. Chem. Soc.* **1994**, *116*, 162.
- (80) Berendsen, H. J. C.; Postma, J. P. M.; van Gunsteren, W. F.; Hermans, J. *Intermolecular Forces* **1981**, 331.
- (81) Hong, M. K.; Braunstein, D.; Cowen, B. R.; Frauenfelder, H.; Iben, I. E. T.; Mourant, J. R.; Ormos, P.; Scholl, R.; Schulte, A.; Steinbach, P. J.; Xie, A.; Young, R. D. *Biophys. J.* **1990**, *58*, 429.
- (82) Young, R. D.; Frauenfelder, H.; Johnson, J. B.; Lamb, D. C.; Nienhaus, G. U.; Philipp, R.; Scholl, R. *Chem. Phys.* **1991**, *158*, 315.
- (83) Merchant, K. A.; Thompson, D. E.; Fayer, M. D. *Phys. Rev. A* **2002**, *65*, 023817.
- (84) Antonini, E.; Brunori, M. *Hemoglobin and Myoglobin in Their Reactions with Ligands*; North-Holland: Amsterdam, 1971.
- (85) Braunstein, D.; Ansari, A.; Berendzen, J.; Cowen, B. R.; Egeberg, K. D.; Frauenfelder, H.; Hong, M. K.; Ormos, P.; Sauke, T. B.; Scholl, R.; Schulte, A.; Sligar, S. G.; Springer, B. A.; Steinbach, P. J.; Young, R. D. *Proc. Natl. Acad. Sci. USA* **1988**, *85*, 8497.

CHAPTER 4: DYNAMICS IN CONFINED ENVIRONMENTS

4.1 INTRODUCTION

Proteins are charged with carrying out their function in a congested and viscous intracellular milieu. It has been known for some time that enzymatic function, specificity, and rates of reaction are strongly modulated by the nature of the solvent. For example, proteins in non-aqueous solvents are known to exhibit significantly modified substrate specificity and reaction rates.^{1,2} Confinement of proteins in nanoscopic water pools such as the pores of a sol-gel glass or reverse micelles increases protein stability towards denaturation³⁻⁵ and can increase the enzymatic turnover.⁶ The protein glass transition, most clearly seen as a decrease in the amplitude of anharmonic protein fluctuations around ~180K and universally observed in all proteins to date, is another example of protein-solvent coupling.^{7,8} The studies presented in this chapter methodically address the role of the solvent in modulating heme protein dynamics by applying 2D-IR spectroscopy and molecular dynamics simulations to obtain a molecular description of protein dynamics in confinement.

Section 4.3 presents homodyne detected 2D-IR experiments and MD simulations of several protein confined in a room-temperature trehalose glass. Trehalose, a non-reducing sugar that forms a glass at room temperature, has long been recognized as an efficient natural bioprotectant and is employed by organisms capable of surviving conditions of extreme heat and draught (anhydrobiosis).⁹⁻¹² Organisms such as the “water bear” (see Figure 4.1) are capable of entering a state of suspended animation that can persist for several years. Surprisingly, when re-hydrated, these organisms return to their previous level of biological activity unaffected by the dehydration process. The ability to survive such adverse conditions without irreversible damage to proteins and cellular membranes has been linked to high concentrations of trehalose.¹¹ Although it is generally agreed that trehalose is the

source of anhydrobiotic protection, the mechanism by which the sugar interacts with proteins remains an area of active investigation.¹²⁻²⁰



Figure 4.1 Scanning electron micrograph images of an active water bear (tardigrade) under normal conditions (left) and in a state of anhydrobiosis (right). Organisms in such a state can survive environmental extremes for decades and still revive to levels of normal biological activity under appropriate conditions. The disaccharide trehalose is key in accomplishing this miraculous feat. Picture taken from reference 9.

In Section 4.4, homodyne detected 2D-IR spectroscopy is used to probe the fast structural dynamics of four globular heme proteins as a function of viscosity at room temperature. The solvent viscosity was tuned over five orders of magnitude by adding fructose to the aqueous protein solutions. Protein dynamics were directly measured by binding CO, a strong IR chromophore, to the reduced Fe(II)-heme active site of each of the proteins. Cytochrome *c*₅₅₂ from *Hydrogenobacter thermophilus* is a small, ~11 kDa, globular protein with a solvent-accessible active site that contains a methionine ligand distal to the heme plane. The axial methionine residue in cyt *c*₅₅₂ was replaced by an alanine (M61A) to accommodate CO binding to the heme, and the aqueous mutant protein has been recently characterized by 2D-NMR and vibrational echo experiments.²¹⁻²³ Since the residue distal to the heme is known to strongly influence the dynamics sensed by the CO²⁴, we also investigated the viscosity dependence of wild type myoglobin (MbCO) and a mutant in which the distal histidine has been replaced by a valine (H64V). Finally, we investigated the viscosity dependent protein dynamics of the ~64 kDa adult human hemoglobin (HbCO).

The work presented in Section 4.5 looks at aspects of protein dynamics in nanoscopic confinement by means of homodyne 2D-IR experiments and MD simulations. The proteins in this section, wild type myoglobin and hemoglobin, were embedded in silica sol-gel glasses. Sol-gel glasses consist of nanoporous networks with interpore connections that permit the exchange of solvent and small molecules while inhibiting the transport of larger species.²⁵ Therefore, sol-gel glasses are exemplary systems for studying the influence of spatial confinement on biomolecular structure, dynamics, and function.²⁶⁻²⁸ Studies of this nature can generate an understanding of protein functionality in the often crowded physiological environment in which biomolecules operate. It has been broadly shown that the overall stability of proteins and enzymes embedded in such glasses is enhanced with regard to temperature, pH, and chemical denaturation.^{3,29-36} In addition, tertiary and quaternary conformational changes in heme proteins, such as myoglobin (Mb) and hemoglobin (Hb), can be inhibited or dramatically slowed, which allows these proteins to be “trapped” and studied in non-equilibrium structural conformations.^{4,37-44}

Section 4.6 concludes this survey of protein dynamics in confinement by examining the dynamics of hemoglobin in human erythrocytes. Hemoglobin concentration inside a red blood cell is extremely high, particularly when compared to other cellular proteins. As a result of this high concentration, the physical properties of cytoplasmic hemoglobin, such as viscosity, are significantly different from those in aqueous solutions. The viscosity inside the erythrocytes is measured, so that the relevant comparisons to the results in aqueous solution can be examined. The results presented below demonstrate that the fast structural fluctuations sensed by the CO ligand bound at the active site of HbCO are the same in the erythrocytes as in aqueous solutions, in spite of the differences in concentration, viscosity, and the detailed chemical nature of the medium.

4.2 MATERIALS AND METHODS

4.2.1 *Preparation of Trehalose Glasses*

Lyophilized methemoglobin (human), sodium hydrosulfite (dithionite), and deuterium oxide (99%) were used as received from Sigma Aldrich. D-(+)-trehalose dihydrate was used as received from ICN Biochemicals Inc. Potassium phosphate monobasic and sodium hydroxide were used as received from J.T. Baker. Human mutant myoglobin H64V was graciously provided by Professor Steven Boxer, Department of Chemistry, Stanford University. The M61A mutant of *Ht* cyt *c*₅₅₂ (*Ht*-M61A) was prepared according to the procedure described previously in Section 3.2.1. HbCO, H64V, and *Ht*-M61A samples in trehalose were prepared by combining equal parts of the carbonmonoxy stock solution (prepared as described in Section 3.2.1) with a saturated trehalose solution (approx. 50% by weight) in D₂O. 25 μ L of the mixture was then spin coated onto a CaF₂ window to produce a thin (~30 μ m thick) high optical quality film. The samples were allowed to dry in a desiccator at ambient temperature and pressure for at least 10 hours and were then placed under vacuum (20 mTorr) for at least 24 hours to remove residual water. Typical trehalose samples had absorbances at the CO stretching frequency of 0.05 to 0.075 on a background absorbance of 0.15 OD. Using an average film thickness of 30 μ m and the integrated area of the OH stretching and libration combination band (2129 cm^{-1}) of pure water in a cell of known thickness, the amount of water remaining in these films was estimated to be less than 0.5% by weight. Data collection for all samples was performed in an enclosed, dry air purged environment. For HbCO and H64V in trehalose, all linear and nonlinear spectroscopic data were collected in a chamber under 20 mTorr vacuum to ensure maximum dehydration.

4.2.2 *Preparation of Variable Viscosity Fructose Solutions*

Aqueous proteins were prepared according to the procedure described above. To increase the solution viscosity, fructose was added to the samples. Proteins at intermediate viscosities (less than ~200 cP) were prepared by dissolving fructose

directly into the protein-water solutions. For the highest viscosities, the protein-water-fructose solutions were placed in a rotary evaporator to reduce the water content and increase solution viscosity. The viscosities of MbCO and HbCO fructose water solutions were measured directly by spinning disk rheometric methods (ARES Rheometer, Rheometric Scientific). Limited availability and small sample volumes of the mutant proteins (M61A and H64V) precluded a direct rheometric determination of the solution viscosity, thus we developed a spectroscopic approach to accurately measure the solution viscosity over a range between ~ 10 -10,000 cP.

4.2.3 Preparation of Sol-Gel Encapsulated Proteins

Sol-gel encapsulated protein samples were prepared using a slightly modified Ellerby procedure.²⁶ To prepare the sol, 1.84 mL of tetramethoxysilane (TMOS) (Sigma Aldrich) was combined with 422.5 μL of D_2O and 27.5 μL of 0.04 N HCl in D_2O , and then sonicated at room temperature for 10 minutes to produce a clear homogeneous mixture. Within 5 minutes, an aliquot of the prepared sol was rapidly mixed with pH 6.5 bis tris D_2O buffer (50mM) followed by mixing with the protein stock solutions (prepared as described above). It has been demonstrated that the use of D_2O instead of H_2O during the sol-gel preparation does not affect the polymerization process.⁴⁵ The volumes of these three components were varied as listed in Table 4.1, to produce samples with good optical quality and the desired molar ratio of silane precursor to water (R -value). The variations of pore diameter with R -value have been quantified by techniques that require drying of the sol-gel glass, which is known to decrease the pore volume by a few tens of percent. Thus there is some uncertainty in the wet-aged sol-gel pore diameters. However, it is reasonable to expect that the decrease in dried sol-gel mean pore diameter with an increase in R is a consistent trend among wet-aged sol-gel samples. At the protein concentrations used in this study, the protein was estimated to occupy 20% of the solution volume in the protein stock solutions. Therefore, when calculating the R -values in Table Table 4.1, the water volume added from the protein solutions was taken to be 80% of the total volume of stock protein solutions.

	sol (μL)	pH 6.5 buffer (μL)	protein stock solution (μL)	<i>R</i> -value
MbCO	20	5	25	15
	20	20	35	27
	20	35	25	30
	20	40	40	39
HbCO	20	5	25	15
	20	20	35	27

Table 4.1 Volumes of components mixed to prepare sol-gel encapsulated protein samples and their corresponding *R*-values.

The mixed components were immediately transferred to a sample cell consisting of two CaF_2 windows and a 50 micron Teflon spacer. The Teflon spacer was discontinuous around the edge of the CaF_2 windows to permit exchange of methanol and buffer solutions during the gelation and soaking processes. The samples typically formed a gel within 30 seconds, and a small weight maintained pressure on the sample cell for 5 minutes. The sol-gel samples were then soaked in pH 7.0 D_2O phosphate buffer solution (50 mM) to neutralize the pH of the aqueous solvent in the sol-gel pores. The pH-sensitive FT-IR spectra for MbCO and HbCO^{22,46} confirmed that the pH inside the sol-gel samples was 7.0 after 48 hours. The edge openings in the Teflon spacers were sealed with Parafilm to prevent drying and vibrational echo data was collected immediately after the 48 hour soaking period.

4.2.4 Preparation of CO-saturated Erythrocytes

Whole blood was purchased from the Stanford Blood Bank in an EDTA solution. The samples were spun at 2,200 rcf for 10 minutes in a microcentrifuge. The plasma was removed from the packed red cells by syringe and the process repeated. The blood cells were then placed under a CO atmosphere for one hour, followed by loading into a sample cell. Visible and infrared spectroscopic studies were performed to ensure binding of CO to the erythrocyte samples.

4.2.5 Determining FFCFs

Multi-exponential frequency-frequency correlation functions, $C(t)$, of the form

$$C(t) = \Delta_0^2 + \sum_{i=1}^n \Delta_i^2 \exp(-t/\tau_{m,i}) \quad (4.2-1)$$

were extracted from the data according to the procedures outlined in Section 3.2.4. Here, Δ_0 is the contribution from static frequency distributions, or inhomogeneous broadening, to the root-mean-squared vibrational frequency fluctuation of the CO, and Δ_i is the magnitude of the contribution from a process with correlation time $\tau_{m,i}$. If τ_m is fast compared to Δ^{-1} ($\Delta \tau_m \ll 1$, Δ in radians/ps) for a given exponential term, then that component of the FFCF is motionally-narrowed.⁴⁷⁻⁵⁰ For a motionally-narrowed term in $C(t)$, a pure dephasing time, T_2^* , can be defined ($T_2^* = (\Delta^2 \tau_m)^{-1}$), which describes the “homogeneous linewidth” for that component of the FFCF. Although protein dynamics generally occur over a continuum of timescales, a multi-exponential $C(t)$ organizes these fluctuations into experimentally relevant timescales.

Both substates in the aqueous HbCO data⁵¹ were modeled with bi-exponential FFCFs ($n = 2$ in Eq. (1)). The aqueous H64V and *Ht*-M61A and all three proteins in trehalose glasses were fit with a bi-exponential FFCF. The FFCF obtained from analysis of the data using response theory calculations was deemed correct when it could be used to calculate vibrational echo decays that fit the experimental vibrational echo data at all T_w s and simultaneously reproduce the linear absorption spectrum.

4.2.6 Computational Methods

MD simulations were performed on one molecule of H64V and 3483 TIP3P water molecules,⁵² using the MOIL software package, as described in Section (3.2.3).⁵³ Two sets of simulations were performed to model the dynamics of the protein in liquid and in glassy solvents. Dynamics in aqueous solution were modeled by simulations in which the protein and solvent were equilibrated to 300 K, followed by constant energy simulations for 5.9 ns with $T = 300 \pm 3$ K. Dynamics in a glassy solvent were represented by selecting water and protein configurations from trajectories with $T \approx 300$ K, fixing the water coordinates, and allowing the protein

dynamics to occur in the static potential of each of these fixed water configurations. A total of 15 trajectories of total duration 2.96 ns were computed for fixed water configurations.

The dynamic Stark effect model for calculating the FFCF from classical MD simulations has been described previously in Section 3.3. Briefly, this model postulates that protein and solvent dynamics, as manifested in the time-varying fluctuations in this electric field, induce a time-dependent fluctuation in the CO frequency. Within a second cumulant approximation to the averaging over the interactions between the CO vibration and its environment, the linear absorption spectrum and the nonlinear vibrational echo may both be calculated from the autocorrelation function of frequency fluctuations, or FFCF,

$$C(t) = \langle \delta\omega(t)\delta\omega(0) \rangle \quad (4.2-2)$$

To analyze the case of a glassy solvent, it is useful to divide the average over all degrees of freedom represented by the angular brackets in equation (4.2-2) into $\langle \dots \rangle_d$, which represents an average over the dynamic protein and solvent degrees of freedom for a given static solvent configuration, and $\langle \dots \rangle_s$, which represents the average over static solvent configurations. The FFCF for the glassy solvent case, $C_g(t)$, may then be rewritten as

$$C_g(t) = \left\langle \left\langle \delta\omega(t)\delta\omega(0) \right\rangle_d \right\rangle_s \quad (4.2-3)$$

with $\delta\omega(t) = \omega(t) - \langle \omega \rangle_d$.

To analyze the results of the simulations in terms of distance dependence from the protein surface,⁷ a grid with 0.2 Å spacing was superimposed onto the original 2MGJ crystal structure. Points within 3.165 Å, the Lennard-Jones minimum of the oxygen atom in the TIP3P potential, of an atom were selected, yielding a smoothed representation of the protein surface. The non-hydrogen protein atoms were then grouped into shells, with atoms in shell 1 within 3.5 Å of the surface, atoms in shell 2 within 3.5-4.5 Å of the surface, atoms in shell 3 within 4.5 –5.5 Å of the surface, atoms in shell 4 within 5.5-6.5 Å of the surface, atoms in shell 5 within 6.5-7.5 Å of the surface, atoms in shell 6 within 7.5-8.5 Å of the surface, and atoms in shell 7

further than 8.5 Å from the surface. Each hydrogen atom added to the crystal structure to form the simulated structure was assigned to the same shell as the non-hydrogen atom to which it was bonded. The heme atoms were not included in these shells, as we have found previously that, while the heme exerts a significant electric field at the CO, it does not contribute to the computed electric field fluctuations on the ps timescale.⁵⁴ The numbers of protein atoms included in each shell (n_i) were $n_1=651$, $n_2=276$, $n_3=209$, $n_4=136$, $n_5=105$, $n_6=68$, and $n_7=47$.

4.3 DYNAMICS IN A TREHALOSE GLASS

4.3.1 Linear Spectroscopy

The normalized and background subtracted linear FT-IR spectra of H64V, *Ht*-M61A, and HbCO are shown in Figure 4.2 for aqueous (solid lines) and glassy trehalose (dashed lines) environments. All peaks have been fit as Gaussian distributions to determine their full width at half maximum (FWHM) and center frequency. The linear IR spectrum of aqueous H64V shows a single transition at 1968.5 cm⁻¹ with a FWHM of 9.1 cm⁻¹ (Figure 4.2c). Since this protein is a mutant of MbCO with the distal histidine replaced by a valine, this peak is generally accepted to correspond to the MbCO A₀ spectroscopic substate.⁵⁴⁻⁵⁹ Upon embedding this protein in dry trehalose (at 20 mTorr), the peak blue-shifts to 1971 cm⁻¹ and broadens to 10.8 cm⁻¹ FWHM. CO bound to *Ht*-M61A in aqueous solution also exhibits a single transition at 1974 cm⁻¹ with a FWHM of 14.6 cm⁻¹ (Figure 4.2b). The *Ht*-M61A CO peak blue-shifts to 1977 cm⁻¹ when the protein is embedded in a trehalose glass. The FWHM of *Ht*-M61A does not change in trehalose from its aqueous value.

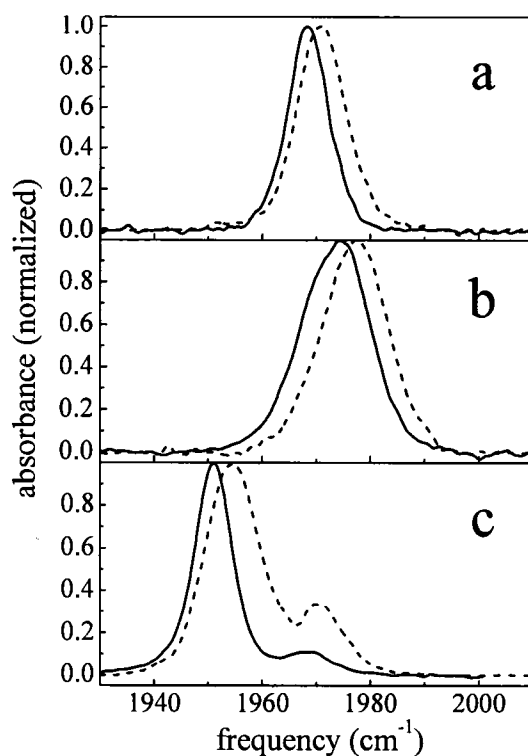


Figure 4.2 Normalized FT-IR spectra of the CO stretching mode bound to a) H64V, b) *Ht*-M61A, and c) HbCO in aqueous (solid lines) and glassy trehalose (dashed lines) environments.

The aqueous HbCO spectrum (Figure 4.2c) exhibits 2 maxima: The main band at 1700 cm^{-1} with a FWHM of 8.3 cm^{-1} and a smaller band at 1670 cm^{-1} . In aqueous HbCO, these have been designated the CIII and CIV peaks,⁵¹ respectively, and correspond to two unique protein structural states. Continuing the trend of H64V and *Ht*-M61A, the CIII band blue-shifts to 1704.5 cm^{-1} and broadens to nearly 12 cm^{-1} FWHM when HbCO is prepared in a dry trehalose glass (at 20 mTorr). In addition, the intensity of the CIV band increases to 33% of the CIII band, reflecting an increased preference for this conformation compared to aqueous solution. A similar phenomenon has been observed for the analogous substate in native MbCO when prepared in dry trehalose.⁴⁶ The spectral centers and linewidths of the three proteins in both aqueous and trehalose environments are summarized in Table 4.2. The Gaussian shape of the spectral bands in all three proteins suggests that these transitions are inhomogeneously broadened. The vibrational stimulated echo experiments described

below confirm that the spectral bands are indeed inhomogeneously broadened, and, therefore, vibrational echo experiments are necessary to uncover the underlying dynamics.

	FT-IR peak (cm ⁻¹)	FWHM (cm ⁻¹)	T_1 (ps)	T_2^* (ps) (= 1/($\Delta_1^2 \tau_1$))
H64V aqueous	1968.5	9.1	21.3 ± 0.2	7.57
H64V trehalose	1970.9	10.8	24.0 ± 0.1	12.75
<i>Ht</i> -M61A aqueous	1974	14.6	25.3 ± 0.2	8.44
<i>Ht</i> -M61A trehalose	1977	14.6	32.0 ± 0.2	9.19
HbCO aqueous	1951	8.3	23.5 ± 0.3	8.44
	1969	~8.3		
HbCO trehalose	1954.5	12.8	24.0 ± 0.2	7.97
	1971	~12.8		

Table 4.2 FT-IR peak centers and linewidths, vibrational lifetimes (T_1), and the pure dephasing times (T_2^*) of the motionally-narrowed component of the FFCFs for H64V, *Ht*-M61A, and HbCO in aqueous and glassy solvents.

4.3.2 Vibrational Echo Spectroscopy in a Trehalose Glass

Figure 4.3 shows the vibrational echo decays for the three proteins in aqueous and trehalose environments at a single T_w (0.5 ps) on a semi-logarithmic scale. The vibrational echo decays of H64V and *Ht*-M61A in aqueous solution (solid lines) and trehalose glasses (dashed lines) are shown in figures Figure 4.3b and Figure 4.3c, respectively. Both proteins exhibit significantly slower CO dephasing when the proteins are embedded in a trehalose glass. The vibrational echo decays for the HbCO CIII substate with the influence of the CIV substate removed in aqueous solution and a dry trehalose glass are shown in Figure 4.3c. It is apparent that the vibrational dephasing of the heme-bound CO is significantly slower for all three proteins in trehalose than it is in aqueous solution. For clarity, we focus our attention here on a single T_w , however, these trends are consistent at all values of T_w . Clearly, some contributions to the CO dephasing depend on surface topology changes.^{60,61} As discussed below, fixing the protein's surface inhibits the movement of some residues or domains deeper within the core of the protein that cause fluctuations in the CO frequency.

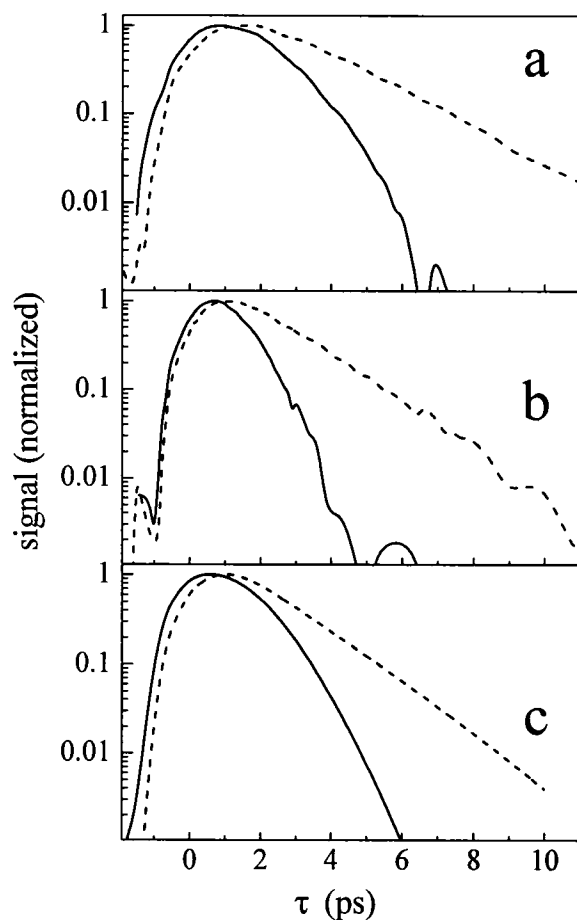


Figure 4.3 Vibrational echo decays at $T_w = 0.5$ ps for CO bound to the three proteins studied: a) H64V (1967 cm^{-1} aqueous, 1971 cm^{-1} trehalose), b) Ht-M61A (1974.7 cm^{-1} aqueous, 1976 cm^{-1} trehalose), and c) HbCO at the CIII band (1951 cm^{-1} aqueous, 1954 cm^{-1} trehalose) with the CIV substate “turned off”. For all plots, solid lines are aqueous data and dashed lines are data taken in trehalose glasses.

It is evident on a semi-logarithmic scale that the aqueous decays for all three proteins are highly non-exponential, while the decays in trehalose glasses are almost single exponentials. Thus, in addition to a change in dephasing rate, going from aqueous to trehalose solvent changes the functional form of the decay. In equation (4.2-1), if $C(t)$ consisted of only a constant term plus a single, motionally-narrowed exponential term, the observed vibrational echo decay curve would be a single exponential that would decay as $\exp(-4\tau/T_2)$ where $1/T_2 = 1/T_2^* + 1/2T_1$.⁶⁰ The fact that the semi-logarithmic plots for all three proteins in trehalose glasses in Figure 4.3 are nearly linear indicates that the stimulated vibrational echoes are dominated by a

motionally-narrowed term in the FFCF. This is in contrast to the data taken in the aqueous solutions in which the decays are highly non-exponential, indicating that the FFCF must contain a significant contribution from dynamics that are not motionally-narrowed.

Table 4.2 contains the T_1 values measured for the three proteins in aqueous and trehalose environments. These data were collected using the transient grating method.^{62,63} For H64V, *Ht*-M61A, and HbCO the T_1 values increase from 21.3 ps, 25.3 ps, and 23.5 ps to 24.0 ps, 32.0 ps, and 24.0 ps, respectively, upon going from an aqueous solution to a trehalose glass. The increases in T_1 in going from aqueous solution to a trehalose glass are small. This demonstrates that the rate of vibrational energy relaxation in the CO ligand is not significantly affected by the nature of the solvent dynamics. The CO vibrational energy has been shown to dissipate efficiently into the vibrational modes of the heme π -system,^{24,64,65} and these results show that fixing the surface of the protein with a glassy solvent does little to affect the vibrational energy relaxation mechanism.

In addition to decreasing the rate of CO dephasing, incorporating proteins into trehalose glasses also changes their spectral diffusion. Figure 4.4 shows vibrational echo decays for H64V in the two solvents at $T_w = 0.5, 4, 8,$ and 16 ps. The decays in aqueous solution (Figure 4.4a) become faster and the peaks of the decay curves shift towards the origin as T_w becomes longer. In the frequency domain, the changes observed in the vibrational echo decays with T_w show that the dynamical line broadens with increasing T_w due to protein dynamics that influence the CO frequency on the T_w timescale. For long enough T_w , spectral diffusion is complete and all chromophores have sampled the entire spectral line. In this case, the dynamic line shape (Fourier transform of the vibrational echo decay) is equal to the absorption line and the vibrational echo peak shift is zero. In aqueous solution, H64V exhibits peak shifts from almost 1 ps at $T_w = 0.5$ ps to less than 0.5 ps by $T_w = 16$ ps. The fact that the vibrational echo decay peaks have not reached zero by $T_w = 16$ ps demonstrates that the full range of protein dynamics affecting the CO frequency have not occurred within this time frame. Figure 4.4b shows that the vibrational echo decays for H64V

in dry trehalose do not change as dramatically with T_w as they do in aqueous solution. By $T_w = 16$ ps, the vibrational echo decay peak has shifted only a very small amount towards the origin, and the decays have become marginally but detectably faster. This demonstrates that some spectral diffusion persists for H64V in the trehalose glass but to a much lesser extent than in aqueous solution on the timescale of the experiment. While we do not present here a detailed study of spectral diffusion as a function of film hydration level, we have observed increases in spectral diffusion when this and other samples are measured at ambient humidity (data not shown). It is intriguing that inclusion of minute quantities of water into the trehalose glass produces a small but measurable change in the longer timescale dynamics reported by the CO. The same trends are observed in the vibrational echo data for *Ht*-M61A and HbCO in aqueous solution and trehalose glasses as a function of T_w . For all three proteins in this study, the qualitative trends are the same: Spectral diffusion is substantially reduced in a trehalose glass within the time frame of the experiments, yet locking the protein surface with this solid solvent does not completely eliminate protein dynamics sensed by the heme-bound CO on the tens of ps timescale.

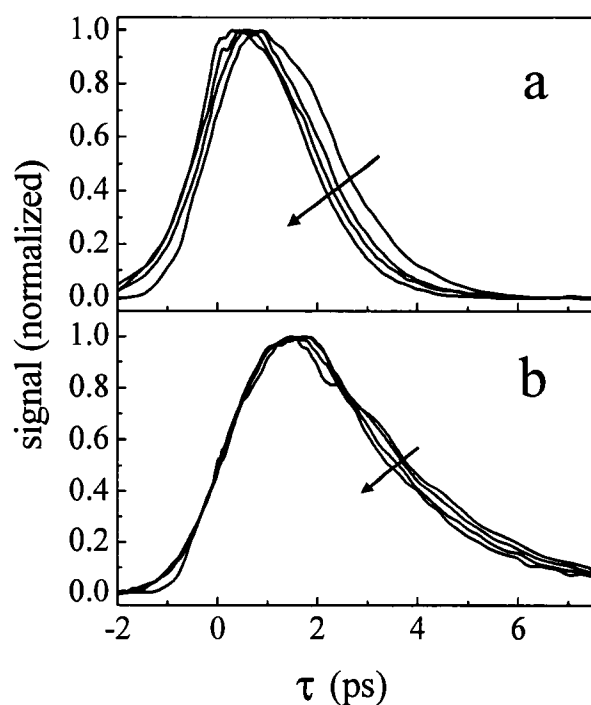


Figure 4.4 Vibrational echo decays as a function of T_w for a) H64V in aqueous solution at 1967 cm^{-1} and b) H64V in a trehalose glass at 1971 cm^{-1} . Both plots show $T_w = 0.5, 4, 8,$ and 16 ps and the arrows indicate the direction of vibrational echo decay shifting with increasing T_w .

Nonlinear response theory⁶⁶ was used to extract FFCFs from the linear and nonlinear spectroscopic signals as described previously. As an example, the best fit calculated linear spectrum and vibrational echo decay at $T_w = 8\text{ ps}$ are overlaid in Figure 4.5a and Figure 4.5b, respectively, with the corresponding experimental data for H64V in trehalose. The agreement between fitted and experimental echo signals is excellent, and the fits to all other data sets were of the same quality.

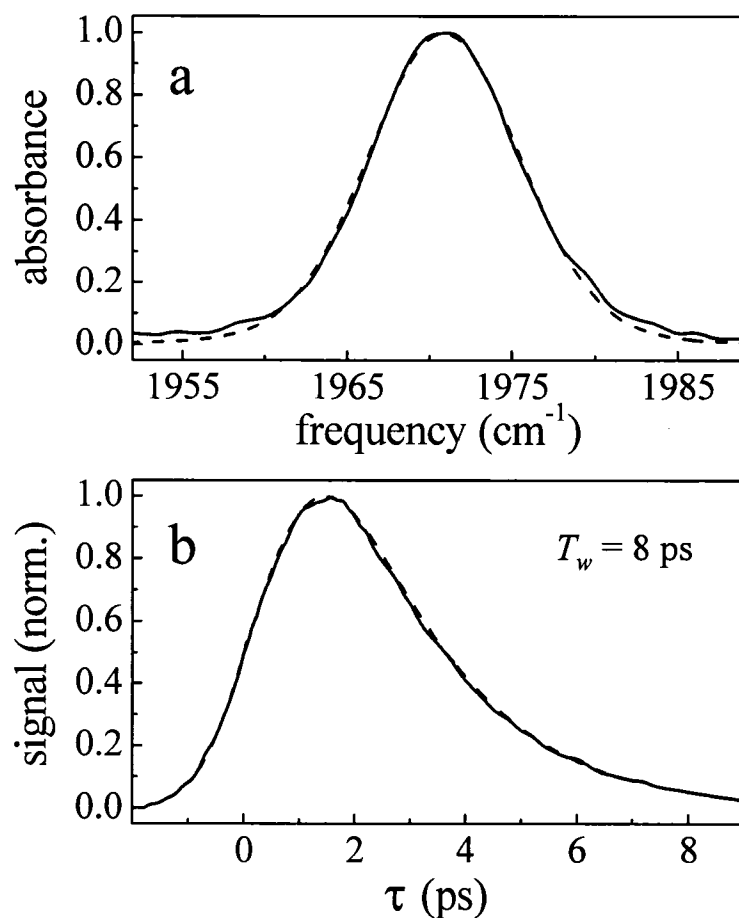


Figure 4.5 a) Experimental linear spectrum and b) vibrational echo decay data at $T_w = 8$ ps (solid lines) overlaid with the best fit linear spectrum and vibrational echo decay ($T_w = 8$ ps) calculated from nonlinear response theory (dashed lines) for H64V in trehalose at 1971 cm^{-1} .

The normalized experimental FFCFs for the three proteins in this study in aqueous solution and trehalose glasses are shown in Figure 4.6. While the differences in the FFCFs at longer times in going from aqueous solution to trehalose glass are dramatic, all six FFCFs contain a fast, motionally-narrowed exponential term. As discussed above (see Section 4.2.5), for a motionally-narrowed component of the FFCF, Δ_i and τ_i cannot be individually determined. Instead, the motionally-narrowed T_2^* is sufficient to describe this component of the FFCF for each sample. This is an intrinsic spectroscopic property and does not depend on the time resolution of the experiment. It was found that five of the six samples have almost the same T_2^* , with $T_2^* = 8.3 \pm 0.6$ ps. For H64V in trehalose $T_2^* = 12.7$ ps. Based on the extracted FFCFs,

we believe that all three heme proteins continue to undergo structurally similar, and possibly universal, fast fluctuations whether the surface of the protein is free to move in aqueous solution or is locked by the trehalose glass.

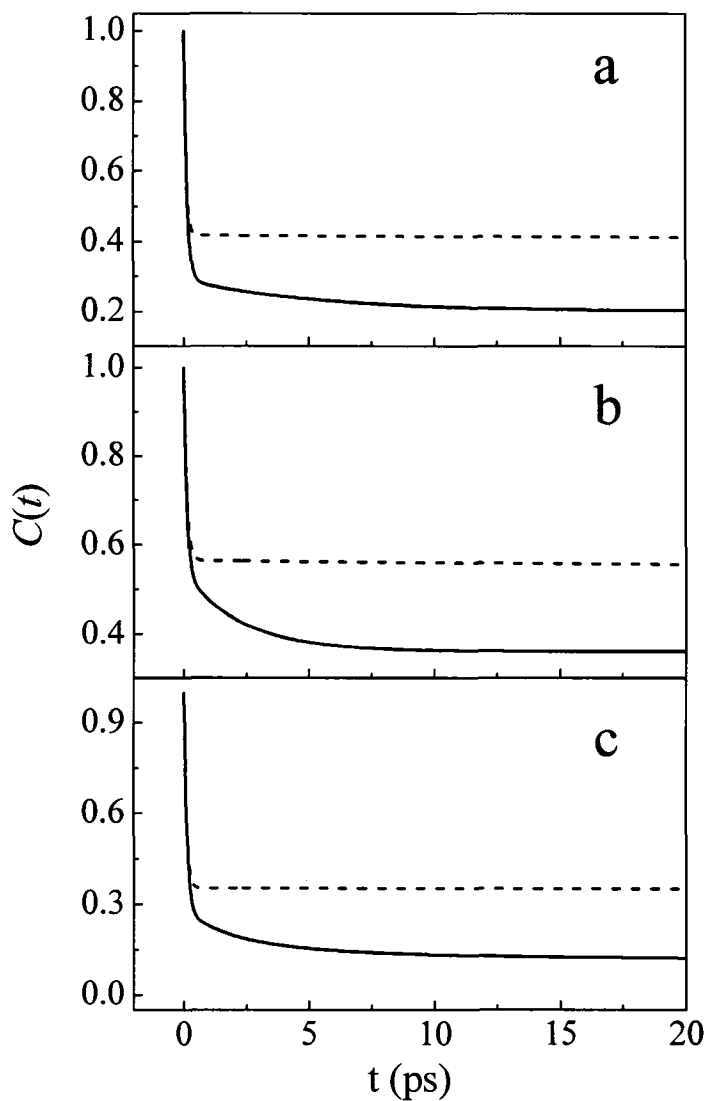


Figure 4.6 Comparison of normalized FFCFs extracted from measured vibrational echo data for a) H64V, b) *Ht*-M61A, and c) HbCO in aqueous (solid lines) and trehalose glass (dashed lines) environments.

On longer timescales (tens of ps), the dynamics of these proteins are quite different in trehalose glasses (Figure 4.6, dashed lines) as compared to aqueous solutions (solid lines). Comparison of the FFCFs for H64V, *Ht*-M61A, and HbCO in trehalose to their FFCFs in aqueous solution shows that embedding these proteins in a

glassy solvent essentially eliminates most of the longer timescale protein dynamics sensed by the CO within the experimental time window. The FFCFs for all three proteins in aqueous solution show some structural dynamics on the tens of ps timescale, while the proteins in trehalose glasses exhibit almost no dynamics after the initial fast motionally-narrowed decay. The dynamics that have been eliminated by placing the proteins in a glassy solvent are the contributions to the CO dephasing from protein motions that depend on surface topology changes; those that remain are independent of the protein exterior fluctuations.

It is notable that all three proteins in trehalose continue to exhibit limited spectral diffusion (Figure 4.4, for example), which is evidence of persistent longer timescale structural fluctuations. The FFCFs for all three proteins in trehalose require a second exponential term to reproduce the observed spectral diffusion. The data sets could not be fit adequately with a single motionally-narrowed term in the FFCF plus a constant term. The second exponential term in the FFCFs for all three proteins were of low amplitude (see Table 4.3 for complete tabulation of best-fit $C(t)$ parameters), indicating that slow fluctuations on the ps timescale contributed a small percentage of the total mean-squared frequency fluctuations. The second exponential term was not

	Δ_0 (rad/ps)	Δ_1 (rad/ps)	τ_1 (ps)	Δ_2 (rad/ps)	τ_2 (ps)
HbCO aqueous (CIII)	0.43	1.05	0.18	0.44	8.4
HbCO trehalose (CIII)	0.89	1.21	0.09	0.11	20.0
H64V aqueous	0.56	1.05	0.12	0.37	5.1
H64V trehalose	0.81	0.97	0.08	0.14	28.0
Ht-M61A aqueous	0.92	1.05	0.11	0.65	2.3
Ht-M61A trehalose	1.14	1.01	0.11	0.19	26.7

Table 4.3 Best fit $C(t)$ parameters (see Equation (4.2-1)) for the three proteins in this study. These values simultaneously reproduce the experimentally measured linear infrared spectra and the vibrational echo decays at several T_w delay times.

the same for the three proteins, nor was it coincident with any of the exponential terms in their respective aqueous FFCFs. The trehalose glass strongly damps slow protein motions that are coupled to the fluctuations of the protein surface. The slower motions that persist in the trehalose matrix appear to be protein specific.

4.3.3 MD Simulations of H64V in Glassy Water Solvents

To obtain a more thorough understanding of the effects of a glassy solvent on protein dynamics, we performed MD simulations on H64V in an environment approximating that of the glassy solvent. The MD simulations of H64V in liquid and static solvents permit the calculation of FFCFs that are directly comparable to the experimentally extracted FFCFs for H64V shown in Figure 4.6 and Table 4.3. The solid curve in Figure 4.7 shows the $C(t)$ calculated from the MD simulation of H64V in liquid solvent, while the dashed curve shows $C_g(t)$ from equation (4.2-3) for the glassy solvent. The MD simulated and experimentally extracted FFCFs for H64V in aqueous solution and their corresponding vibrational echo signals have been compared in detail in Chapter 3.⁵⁵ Comparison of the $C(t)$ extracted from the vibrational echo measurements of H64V in trehalose (Figure 4.6a, dashed line) with $C_g(t)$ for the static solvent in Figure 4.7 shows that the simulations of H64V in an immobile solvent qualitatively reproduce the protein dynamics observed in a glass. The initial rapid decay of the calculated $C(t)$ is very similar for static and dynamic solvents, while the slower dynamics are suppressed in the static solvent, as was observed in Figure 4.6. The rapid decay is also shown in Figure 4.6 and Figure 4.7 to be common to the other heme proteins in this study in both aqueous and glassy solvents. The simulated $C(t)$ s in Figure 4.7 are in accord with the experimental evidence that locking the protein surface affects internal protein dynamics that influence the long timescale frequency fluctuations of the heme-bound CO.

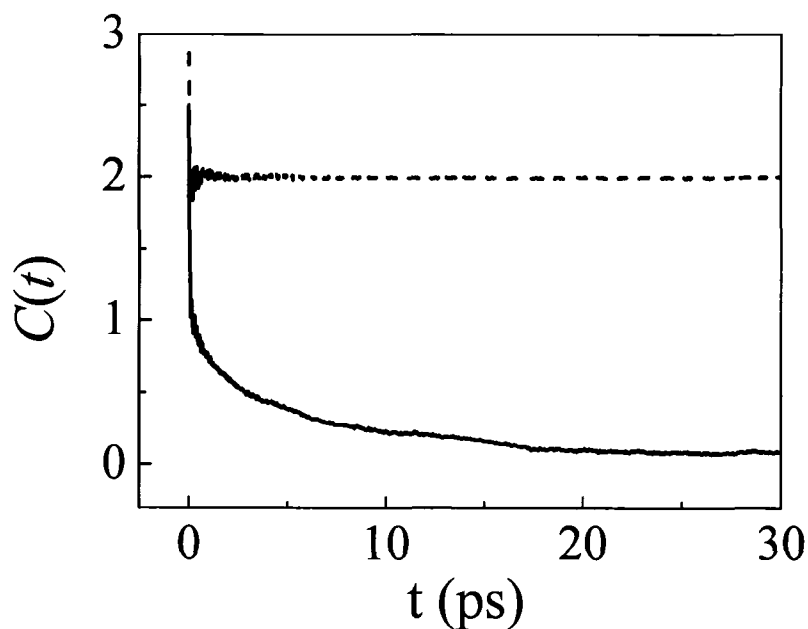


Figure 4.7 $C(t)$ in units of $(\text{rad/ps})^2$, the autocorrelation function of fluctuations in the CO vibrational frequency (FFCF), as calculated from MD simulations of H64V in water. The solid line shows $C(t)$ at $T = 300\text{K}$ in dynamic water, and the dashed line shows $C(t)$ for H64V at $T = 300\text{K}$ in a solvent of static water configurations, representing the effects of a glassy solvent.

MD simulations have the capacity to identify the molecular motions responsible for the initial rapid decay of $C(t)$ shared by H64V in an aqueous and static solvent. In our previous study of sperm whale MbCO,⁵⁴ it was concluded that the entire protein contributed to the initial decay of $C(t)$, and that no particular structural element or dynamical mode was responsible for the decay. Likewise, the initial decay of $C(t)$ for H64V in dynamic and static solvents shown in Figure 4.7 cannot be readily assigned to any single structural motion, but rather to small amplitude dynamics of the entire protein.

The separation of protein dynamics into fast motionally-narrowed and slower dynamic ranges is reminiscent of recent work by Fenimore and coworkers.⁸ Akin to α - and β -relaxations in glasses,⁶⁷⁻⁶⁹ the authors report a separation of mean-squared atomic displacements by Mössbauer and neutron scattering experiments into “bulk solvent-slaved” (α) and “hydration shell-coupled” (β) fluctuations. A completely dehydrated protein continues to display small harmonic motions that have no coupling to an external solvent (“class III” fluctuations).^{8,68,70} Tarek and co-workers reported

that MD simulations with static water mimicked the dynamics of a dehydrated protein.⁷¹ In this context, the predominantly fast structural dynamics that persist for HbCO, H64V, and *Ht*-M61A in trehalose glasses can be classified as a combination of class III and β -dynamics, as there is no bulk solvent present to generate α -fluctuations. In aqueous solution, dynamics on the tens of ps timescale appear for all three proteins and must therefore be coupled to the bulk solvent (α -fluctuations). This correlation seems especially valid in light of our observation that a small amount of hydration of the trehalose films increases spectral diffusion. We speculate that eliminating the hydration shell that is maintained at the protein surface by the trehalose glass might extinguish spectral diffusion completely. Placing these samples into ambient humidity allows more of the β -dynamics to turn on.

To investigate the influence of the solvent on dynamics in different parts of the protein in our MD simulations, we analyzed the dependence of atomic contributions to the equilibrium mean-squared fluctuations in the CO vibrational frequency, $C(0) = \langle (\delta\omega(0))^2 \rangle$, on the distance from the protein surface.⁷ The simulations were analyzed in terms of CO frequency fluctuations instead of the conventional mean-squared atomic displacements because the mean-squared frequency fluctuations have a direct connection to the measured vibrational echo data. According to Equation (4.2-1), $C(0)$ is proportional to the mean-squared fluctuation in the component of the electric field at the CO along the CO dipole. This quantity will certainly be influenced by equilibrium atomic mobilities as measured by the mean-squared fluctuations in atomic coordinates calculated by others,^{7,16,20,72} but will also depend on partial charges and the geometrical effects that determine the direction of the instantaneous electric field vector at the CO. We have grouped the protein atoms by distance from the protein surface using criteria similar to those employed previously (see Section 4.2.6),⁷ and have confirmed the same trends in mean-squared atomic displacements for H64V as observed by Vitkup and coworkers for wild type MbCO (data not shown).⁷ The contribution of shell i to the frequency fluctuation of the CO vibration is denoted $\delta\omega_i(t)$ and is computed from the electric field exerted by atoms in that shell on the CO.

Autocorrelation and cross-correlation functions associated with these shells are then given by $C_{ij}(t) = \langle \delta\omega_i(t)\delta\omega_j(0) \rangle$ with $i = j$ and $i \neq j$, respectively.

The autocorrelation function of CO frequency fluctuations from shell i , $C_{ii}(t)$, is plotted in Figure 4.8a for the liquid solvent and in Figure 4.8b for the static solvent for $i = 1$ (uppermost curve), $i = 3$ (middle curve), and $i = 6$ (lowest curve). As noted in Section 4.2.6, atoms in shell 1 are within 3.5 Å of the protein surface in the crystal structure, atoms in shell 3 lie within 4.5 Å-5.5 Å of the surface, and atoms in shell 6 lie within 7.5 Å-8.5 Å of the surface. Each $C_{ii}(t)$ in Figure 4.8 shows an initial sub-ps decay followed by slower dynamics, as does the total correlation function $C(t)$ for aqueous solution in Figure 4.6. When considering each shell individually, without the influence of other shells, Figure 4.8 shows that there are more significant structural dynamics communicated to the heme-bound CO on the timescale of tens of ps in the outermost shell than in the inner shells. This is not surprising when considering that the outer shells of this protein are not only more likely to be charged and polar, but also less constrained and more free to move. The corresponding $C_{ii}(t)$ s in the static solvent (Figure 4.8b) show a similar fast initial decay as the liquid solvent, with the suppression of slower dynamics by the static solvent in all shells.

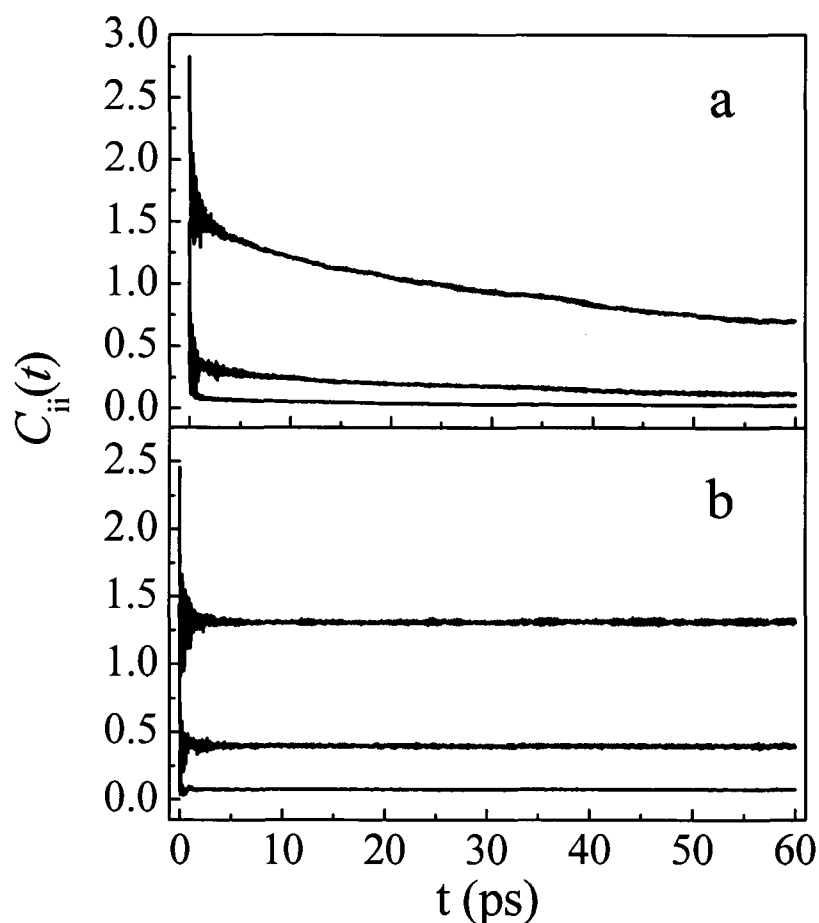


Figure 4.8 $C_{ii}(t)$ (rad/ps^2), the contribution from protein atoms in shell i to $C(t)$, as calculated from MD simulations of H64V for $i = 1$ (uppermost curve), $i = 3$ (middle curve), and $i = 6$ (lowest curve). The shell index increases from protein exterior to interior, as defined in the text. In panel (a), the protein is solvated by liquid water, and in (b), the protein interacts with a solvent of static water configurations, representing the effects of a glassy matrix.

$C_{ii}(0)$, the contribution of each shell to the equilibrium mean-squared fluctuation in the CO vibrational frequency for the liquid solvent calculations is shown by the circles in Figure 4.9a, and is seen to decrease from the relatively polar protein surface to the relatively nonpolar interior. While this plot indicates that the dynamics at the surface of the protein have the largest influence on the equilibrium CO frequency fluctuations, it is important to consider that nearly 44% of the total protein atoms are contained in this shell. Normalization of $C_{ii}(0)$ by the number of atoms in each shell (n_i) yields the squares plotted in Figure 4.9a. On a per atom basis, when considering each shell without the influence of other shells, the largest contribution to

$C(0)$ does not come from the protein surface but rather from shell 5, which is in the range of 6.5 to 7.5 Å from the surface.

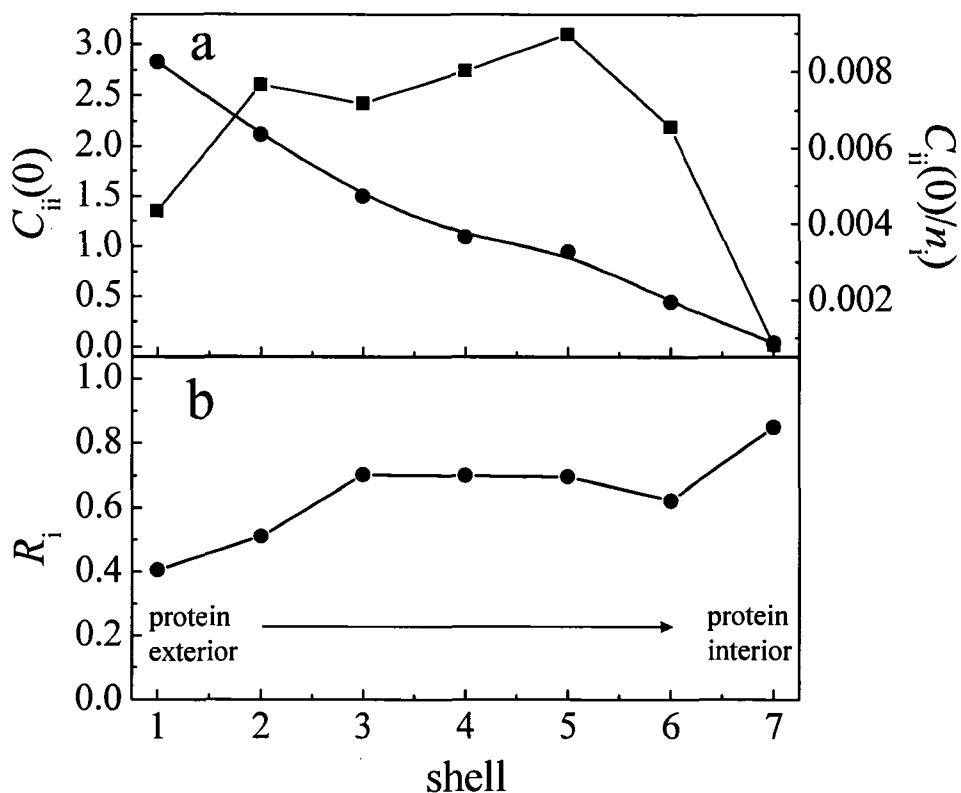


Figure 4.9 a) $C_{ii}(0)$ (rad/ps)², the contribution from protein atoms in shell i to the equilibrium mean-squared fluctuation of the CO vibrational frequency as calculated from MD simulations of H64V in liquid water at T=300 K. The shell index increases from protein exterior to interior, as defined in the text. Filled circles show $C_{ii}(0)$, and squares represent this quantity normalized by the number of atoms in the shell. b) The ratio of $C_{ii}(0)-C_{ii}(\infty)$ for H64V in a glassy solvent to the corresponding $C_{ii}(0)$ in liquid water, defined as R_i in Equation (4.3-1), is plotted for each shell of protein atoms.

To apply this same analysis to the glassy solvent case, we do not examine $[C_g(0)]_{ii}$, which includes fluctuations from both protein dynamics and static solvent configurations, but rather the ratio of the total decay in static solvent, $[C_g(0)]_{ii} - [C_g(\infty)]_{ii}$, which represents mean-squared frequency fluctuations arising from dynamics, to the corresponding decay in dynamic solvent.

$$R_i = \frac{[C_g(0)]_{ii} - [C_g(\infty)]_{ii}}{C_{ii}(0)} \quad (4.3-1)$$

Figure 4.9b plots R_i for each shell. The dependence of R_i on distance from the protein surface quantifies the spatial variation of the suppression of protein dynamics by the static solvent. The fact that $R_i < 1$ for all shells reflects that the dynamic contributions to the equilibrium mean-squared frequency fluctuations in the static solvent are less for all shells than in the liquid solvent. This supports our experimental evidence that fixing the protein surface topology influences structural fluctuations in the inner core of the protein. While R_i does not vary monotonically across the shells, the general trend in R_i in Figure 4.9b is an increase from the protein surface to the interior.

The simulations of Vitkup and coworkers⁷ demonstrated that the effect of a static solvent on wild type MbCO is to suppress atomic mobilities throughout the protein, with atomic mean squared displacements increasing slightly from the protein surface to the interior. Within our electric field model, fluctuations in the CO vibrational frequency arise from motions of atoms with partial charges. Therefore, the damping of atomic motions would be expected to lead to a suppression of frequency fluctuations. However, since the contribution of the motion of a particular atom to the electric field fluctuation depends on partial charge and distance from the CO as well as on its mobility, and since charges are not uniformly distributed throughout the protein, the spatial dependence of the suppression of contributions to CO frequency fluctuations by a glassy solvent is far from obvious. Figure 4.9 demonstrates that the spatial dependence of the damping of atomic displacements reported by Vitkup and coworkers⁷ is mirrored by the mean-squared frequency fluctuations of the heme-bound CO, which are probed by nonlinear spectroscopy.

Although Figure 4.9 illustrates correlations in electric field fluctuations within the individual shells, no direct connection exists between $C_{ii}(t)$ and the total $C(t)$ as a result of cross-correlations between electric field fluctuations at the CO induced by different shells. By computing the cross-correlation functions, $C_{ij}(t)$, we find that $C_{ij}(t)$ for any adjacent pair of shells is negative for all times studied, indicating significant cancellation of electric fields at the CO from different shells to produce the total field. Figure 4.10 illustrates the positive and negative cross-correlations ($C_{ij}(t)$) between electric field fluctuations from the outermost shell ($i = 1$) and four interior

shells ($j = 2, 3, 4,$ and 5) for the dynamic aqueous solvent. The initial values $C_{1j}(0)$ are shown to alternate in sign, although this is not the case for $C_{16}(0)$ and $C_{17}(0)$ (not shown). The corresponding cross-correlations for the static solvent (data not shown) closely resemble the results for the liquid solvent. The anti-correlated nature of the frequency fluctuations in adjacent shells shows that there is no simple relation between the total correlation function $C(t)$ and the autocorrelation functions associated with individual shells.

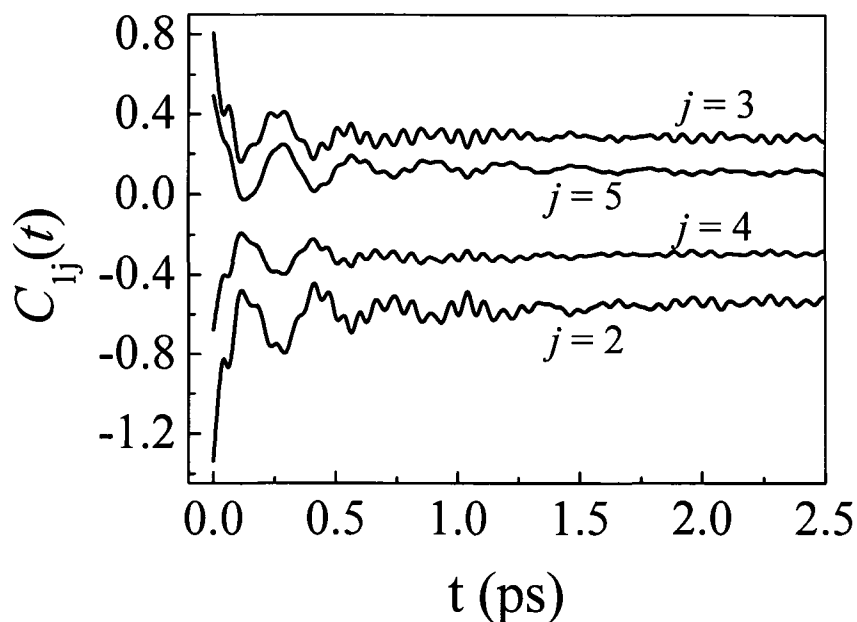


Figure 4.10 $C_{1j}(t)$ (rad/ps)², the cross-correlation functions of the contributions to the fluctuating CO frequency of protein shell 1 (outermost) and shells $j = 2, 3, 4,$ and 5 , as calculated from MD simulations of H64V in dynamic water solvent.

The results in Figure 4.7-Figure 4.10 together with the results of previous simulations of proteins in immobilized solvents,^{7,71} provide a molecular picture of the solvent effects on protein dynamics observed by the vibrational echo measurements. In dynamic solvents, the mean-squared atomic displacements are greatest at the protein surface and therefore contribute strongly to the mean-squared frequency fluctuations of the CO. Placing the simulated H64V into a static solvent suppresses the atomic displacements in all shells, and therefore suppresses the frequency fluctuations at the CO. However, the time-dependent electric fields at the CO from

adjacent shells are shown in Figure 4.10 to be anti-correlated, resulting in significant field cancellation. This anti-correlation of frequency fluctuations underscores the fact that the concerted influence of *all* shells on the CO frequency must be considered in order to understand their influence on the dynamics at the protein active site. As others have shown,⁷ and as we have confirmed here, it is instructive to dissect the simulated protein into distance-dependent shells to understand the effect of solvent dynamics on structural dynamics at various distances from the protein surface. However, when trying to understand these solvent effects on the dynamics at the active site, which defines the functional role of a protein or enzyme, a more complex picture must be considered.

Previous MD simulations of Mb in trehalose water mixtures^{72,73} have suggested that the effect of the trehalose on protein dynamics is similar to that observed in simulations of myoglobin in a static water solvent.⁷ The similarity between the FFCF extracted from experimental vibrational echo data on H64V in a trehalose glass and that calculated from the MD simulation of H64V in a static water solvent is consistent with this finding. A more quantitative analysis of the effect of the trehalose glass environment on the protein dynamics probed by the vibrational echo must await the calculation of vibrational echoes directly from a simulation of MbCO in a room temperature trehalose-water glass, a study which is reserved for future work.

In the context of bio-protection, the results presented here indicate that inhibiting movement of the hydration shell water molecules is an effective way to suppress longer timescale (tens of ps) structural dynamics at both the surface and inner core of a protein. In the preferential hydration model,^{8,16,20} trehalose forms few direct hydrogen bonds to the protein and functions primarily by concentrating and limiting the mobility of residual water at the protein surface. That the measured vibrational echo data for HbCO, H64V, and Ht-M61A in trehalose glasses and the simulated H64V in static solvent produce qualitatively similar FFCFs supports this model in which the trehalose functions as a bioprotectant by hindering displacements of the hydration shell water molecules at the protein surface.

4.4 VISCOSITY DEPENDENT PROTEIN DYNAMICS

4.4.1 Linear and Stimulated Vibrational Echo Spectroscopy

The viscosity dependent FT-IR spectra of CO bound to MbCO, HbCO, H64V, and M61A are shown in Figure 4.11a-d, respectively. Both MbCO and HbCO exist as an ensemble of structurally distinct, interconverting substates that give rise to multiple peaks in the FT-IR spectrum of the CO. In the case of MbCO, three spectroscopic substates commonly labeled as A₃, A₁, and A₀ (very small) can be observed at 1934, 1944, and 1968 cm⁻¹ respectively. In HbCO, two substates are observed at 1951 and 1968 cm⁻¹.

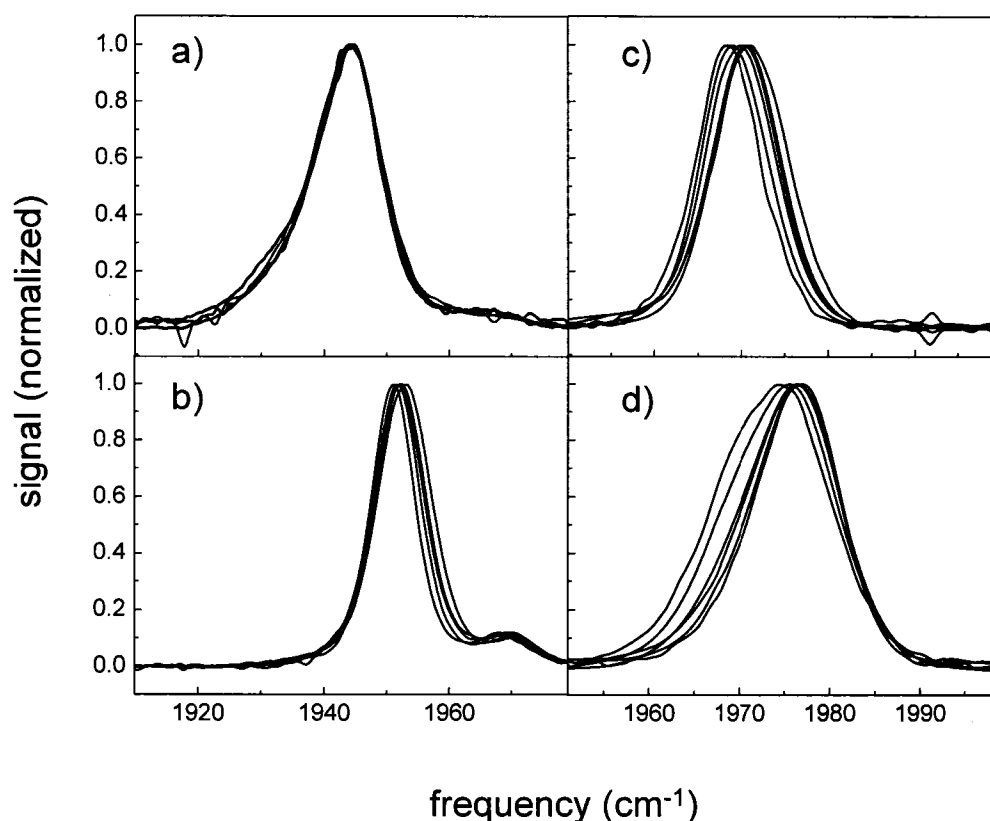


Figure 4.11 Viscosity dependent FT-IR spectra of the four proteins. All data have been background subtracted and normalized. As viscosity is increased, the FT-IR spectra shift to higher frequency by a few wavenumbers. Panels (a)-(d) show the spectra of MbCO, HbCO, H64V, and M61A respectively.

The linear absorption spectra of the proteins examined in this study are only mildly dependent on the solvent viscosity. Upon addition of fructose (and an increase

in the viscosity) the linear absorption spectra of all proteins except MbCO shift by a few wavenumbers to the blue. Of all four proteins, M61A exhibits the largest blue shift of 2.7 cm^{-1} upon encapsulation in a fructose film. As the viscosity is increased, the spectral linewidths of the CO stretch in MbCO and H64V do not increase appreciably within the spectral resolution of the FT-IR measurement, and the linewidth of the HbCO peak increases by $\sim 1.5 \text{ cm}^{-1}$. The linewidth of CO bound to M61A decreases with increasing viscosity and is 3 cm^{-1} narrower when the protein is encapsulated in a fructose glass relative to an aqueous environment. The linear absorption measurement is sensitive to protein structural fluctuations that occur on all timescales. Thus, an increase in the width of the CO band could either be indicative of increased protein structural inhomogeneity or faster structural dynamics. In M61A, increasing viscosity does not introduce additional structural configurations while reducing the percentage of the total linewidth that is due to dynamic processes (see below). Subsequently, the width of CO band in M61A decreases as viscosity is increased. The difference in FT-IR linewidth observed for M61A relative to HbCO and MbCO may be due to the protein's small size (11 kDa) or relatively solvent-exposed active site, which may permit different solvent-protein interactions.

The relative concentrations of the structural substates in MbCO and HbCO are generally sensitive to solution conditions.⁷⁴⁻⁷⁷ In protein-sugar films, the substate concentration is sensitive to the degree of film hydration and the type of saccharide used.^{46,72,78} A change in the substate ratio means that there is a change in the relative thermodynamic stability of the two substates or for very dry films it is possible that the sugar glass captures the system far from equilibrium. The ratio of the spectroscopic substates in MbCO and HbCO does not change even in the fructose sugar films, contrary to what has been observed in trehalose and sucrose.^{20,22,46} This observation may indicate that water preferentially hydrates the protein to a greater degree in fructose than in trehalose or sucrose glasses^{20,22} or that the fructose films retain more residual moisture than the disaccharides.

The linear absorption spectrum of heme-CO in proteins at room temperature is inhomogeneously broadened, obscuring the underlying protein dynamics.^{22,47,55,79}

Stimulated vibrational echo spectroscopy can look inside the inhomogeneously broadened absorption spectrum and reveal information about the fast dynamics of protein fluctuations.⁸⁰ Figure 4.12 displays the spectrally resolved vibrational echo decay curves of H64V taken at the center of the 0-1 transition frequency as a function of increasing viscosity at a fixed waiting time, $T_w = 2$ ps. All four proteins exhibit similar qualitative behavior. As the viscosity of the protein-fructose-water solution is increased the vibrational echo decays become slower and approach exponential decay functions as the viscosity approaches that of the sugar glass.

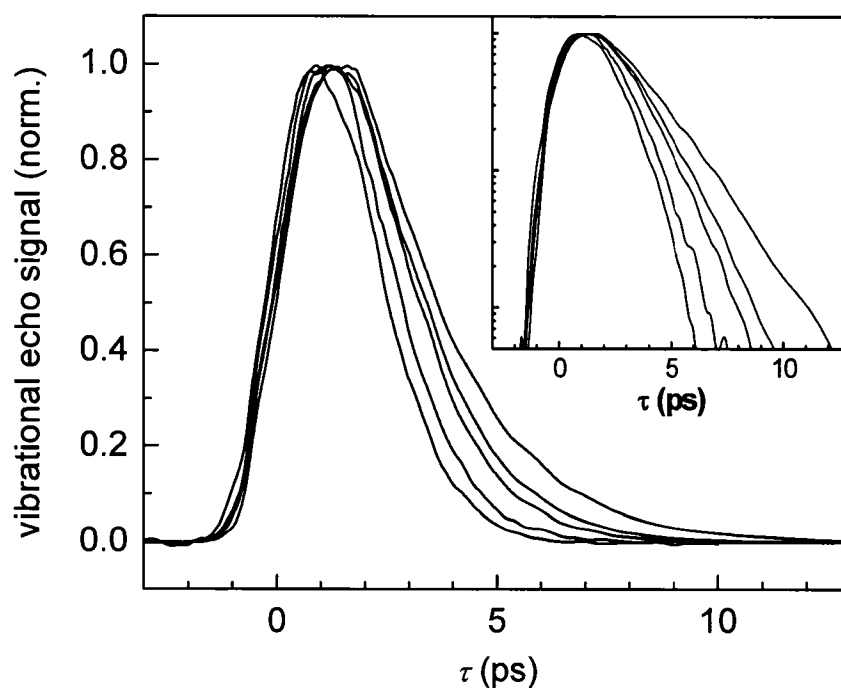


Figure 4.12 Normalized spectrally resolved vibrational echo decays acquired at $T_w = 2$ ps as a function of viscosity for H64V. As the viscosity is increased from aqueous (~ 3 cP) to a sugar-glass, the vibrational echo dephasing becomes slower and approaches a single exponential decay. The inset presents the same data on a semi-log plot.

For all four proteins, the vibrational echo decays slow down as a function of increasing viscosity and asymptotically approach an exponential decay in the fructose film (infinite viscosity). Fructose was chosen as a co-solvent because its concentration could be varied to continuously modulate the viscosity from several cP to $\sim 10,000$ cP and eventually to a sugar glass. To verify that the changes in the protein dynamics are related to the solution viscosity (as opposed to fructose-specific interactions) we

compared several data sets acquired at viscosities up to ~ 200 cP but where the co-additive was glycerol. The vibrational echo decays were identical regardless of whether fructose or glycerol was used to increase the viscosity. This observation is consistent with earlier observations that MbCO dynamics were sensitive to the solution viscosity regardless of whether ethylene glycol and glycerol is used as a co-additive.⁶⁰

The nearly exponential vibrational echo decays of heme-proteins encapsulated in a fructose glass are consistent with the behavior of proteins confined in other sugar glasses at room temperature and ethylene glycol and glycerol glasses observed at lower temperatures.^{22,60,61} The onset of single exponential vibrational echo decays is a signature of the separation of the protein dynamics into two limits: very fast processes which produce motionally narrowed Lorentzian line shapes and give rise to exponential vibrational echo decays, and very slow or static processes which do not evolve on the vibrational echo timescale and give rise to the Gaussian inhomogeneous distribution observed in the linear absorption spectrum. Previously, we have shown that the fastest protein dynamics that are sensed by the CO are essentially solvent independent and persist even when the protein is encased in a trehalose glass.²² Our current findings confirm that this is a reoccurring feature of protein dynamics in sugar glasses and that the identity of the protein or the sugar is not important. By continuously increasing the solution viscosity we are able to monitor the transition from the dephasing that occurs over a variety of timescales in aqueous solution to the mostly ultrafast fluctuations that give rise to approximately single exponential vibrational echo decays that were previously observed in trehalose glasses.

In stimulated (three-pulse) vibrational echo experiments, the dynamics that occur on timescales longer than those shown for a single vibrational echo decay (Figure 4.12), termed spectral diffusion, can be measured by varying the time delay between the second and third pulses, T_w . Although at each T_w the entire decay curve is measured, it is convenient to display the large number of data sets by plotting the vibrational echo peak shift^{55,81-83} as a function of T_w . The vibrational echo peak shift is the difference between the time of peak amplitude of the decay curve and zero

time.^{81,82} As T_w is increased more fluctuations that occur at longer times are observed. These additional fluctuations cause the vibrational echo to decay faster and its peak to shift towards the origin.^{55,81,82} A faster vibrational echo decay and smaller peak shift mean that a larger portion of the total possible structural configurations of the protein has been sampled. For long enough T_w , spectral diffusion is complete and the proteins have sampled all possible structures. In this limit, the Fourier transform of the vibrational echo is equal to the absorption line and the vibrational echo peak shift is zero. In the experiments conducted here, the long time limit is not reached because the maximum T_w is restricted by the CO vibrational lifetime.⁸⁴⁻⁸⁶

Figure 4.13 shows the vibrational echo peak shifts for H64V at several viscosities and in a fructose film. In the aqueous protein (Figure 4.13, filled squares), the protein samples ~50% of the full linewidth by a T_w of 16 ps. As viscosity is increased, the protein dynamics shift to slower timescales, as is evidenced by the larger initial peak shift amplitude and the reduction in the decay of the peak shift as a function of T_w . At very high viscosities, the protein is unable to sample a substantial portion of its dynamic linewidth within the experimental observation window. It is interesting to note that the spectral diffusion at ~20,000 cP is identical within experimental error to that of a fructose film (Figure 4.13, top two sets of data points). If the fast protein dynamics consisted only of a very fast motionally narrowed contribution to the vibrational echo decay with no spectral diffusion, then the peak shift would be independent of T_w . The mild slope of the upper most points and nearly-exponential vibrational echo decays show that there continues to be some spectral diffusion even in a fructose glass, which may indicate incomplete dehydration of the sugar-film. The decrease in the slope of these peak shift plots with increasing viscosity demonstrates that the spectral diffusion is significantly reduced relative to that of the aqueous protein. The vibrational echo dynamics of all four proteins exhibited the same decrease in spectral diffusion dynamics as viscosity is increased. Furthermore, all protein encapsulated in a fructose glass showed a mild T_w dependence, suggesting that the proteins still undergo limited structural evolution on the timescales

of several T_w . The decrease in spectral diffusion is caused by a decrease in sampling of distinct protein structures on a timescale out to ~ 5 times the longest T_w .⁸⁶

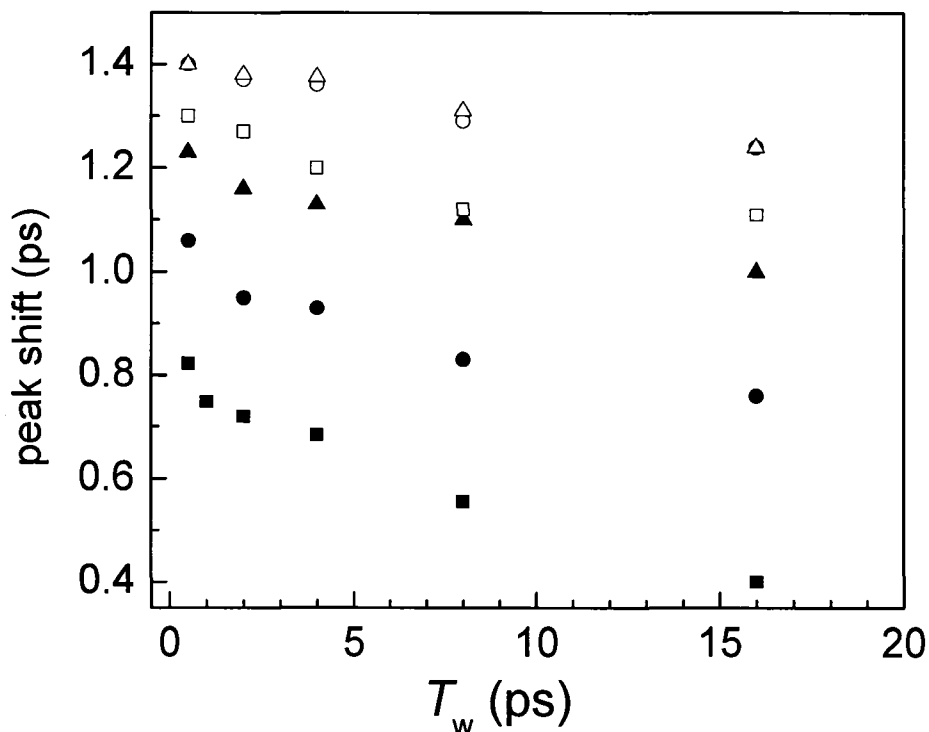


Figure 4.13 The spectrally resolved vibrational echo peak shift as a function of T_w for H64V as the viscosity is increased. The viscosities of the data are 3 cP (solid squares), 40 cP (solid circles), 660 cP (solid triangles), 6400 cP (open squares), 28,000 cP (open circles), and in a sugar glass (open triangles). The vibrational echo peak shift indicates that spectral diffusion becomes significantly slower, but does not completely vanish as the viscosity is increased.

The peak shift information can also be used to conveniently gauge the relative viscosity-dependent behavior of the proteins in this study. Figure 4.14 plots the peak shift of HbCO, H64V, and M61A at $T_w = 2$ ps as a function of viscosity. The peak shifts of the A_1 and A_3 states of MbCO are difficult to determine because of the high degree of spectral overlap between the two states and these peak shifts are omitted from the current discussion. As the viscosity is increased the amplitude of the peak shifts increase (reflecting a decrease in the spectral diffusion) and asymptotically approach the peak shifts of the proteins in the fructose glass (indicated by the dashed line). The amplitude of the H64V peak shift is larger than that of HbCO and M61A. However, the viscosity dependence is reflected by the rate of change of the peak shift

as a function of viscosity. The peak shift dependence on viscosity is nearly identical for all three proteins, and this observation remains consistent at all T_w s.

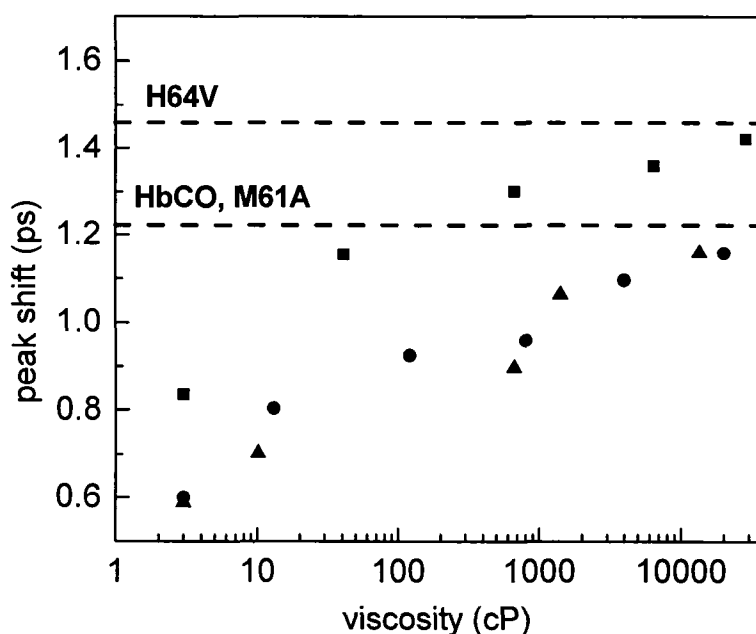


Figure 4.14 The spectrally resolved vibrational echo peak shift as a function of viscosity for $T_w = 2$ ps. The data are for the 0-1 transition frequencies of H64V (squares), M61A (triangles), and HbCO (circles). As viscosity is increased, the peak shift approaches the infinite viscosity asymptotic value (shown as dashed lines) of the fructose sugar-film. The viscosity dependence of the spectral diffusion (change in the peak shift with viscosity) is nearly identical for the three proteins.

4.4.2 Viscoelastic Model

The viscosity dependent vibrational dephasing data has been discussed above in terms of several qualitative observations about the viscosity dependence of the structural fluctuations of heme proteins. First, the protein structural dynamics, as sensed by the CO bound to the heme active site, are only mildly sensitive to the detailed structure of the protein. We examined four proteins of varying sizes from the relatively small ~11 kDa *Cyt. c* M61A mutant, to the ~16 kDa MbCO and H64V mutant, and the larger 64 kDa HbCO. Furthermore, the residue distal to the heme plane was different in three of the four proteins: alanine (M61A), histidine (MbCO, HbCO) and valine (H64V). Although each of the proteins exhibits different dephasing rates that are sensitive to the identity of the distal residue and proteins structural dynamics,^{22,55} the viscosity dependent change in these fluctuations remained nearly the

same for all four proteins. In each case, the dynamics are significantly slower in higher viscosity solvents and the longer timescale (<100 ps) fluctuations, observable as spectral diffusion, are nearly identical for the four proteins. Changing the solvent from fructose-water to glycerol water did not change the result, which demonstrates that the dominant influence on dynamics is indeed viscosity rather than the changing composition of the fructose-water mixture.

Second, we observed that the dephasing rates exhibit a weak viscosity dependence. These data presented in Figure 4.14 spans over five orders of magnitude in viscosity but the rates of spectral diffusion and vibrational dephasing change by approximately two orders of magnitude.

Both of these experimental observations are consistent with previously reported two-pulse vibrational echo measurements of the A_1 state MbCO as a function of viscosity and temperature.⁶⁰ A conceptually simple viscoelastic theory of protein-solvent interactions was used to discuss the earlier temperature and viscosity dependent experimental data of the A_1 state of MbCO.^{47,60,87} The main features of the viscoelastic model describing the relationship between viscosity dependent protein structural fluctuations and vibrational echo observables⁶⁰ will be briefly recapitulated and then tested with the isothermal viscosity dependent protein dynamics data presented in this study.

The CO group in heme proteins is located in the protein interior and does not interact with the bulk solvent directly. Rather, vibrational dephasing of the CO is well described by interactions between the CO dipole moment and time-dependent fluctuating electric fields that arise from structural dynamics of partially charged residues within the protein.^{24,54,88,89} Protein structural fluctuations are known to be strongly coupled to solvent dynamics.^{7,17} Protein structural fluctuations may involve transient reorganization of the solvent around the protein, a process that is increasingly hindered as viscosity is increased. Structural fluctuations, even those that involve the interior of the protein, can require surface topology changes of the protein. These surface topology changes are resisted by the solvent, and the resistance increases as the viscosity increases. In the viscoelastic model, the protein is treated as a sphere of

radius r_p embedded in a viscoelastic continuous solvent with a given viscosity, η . The model considers spherical fluctuations of the protein's volume; i.e., the protein is treated as a breathing sphere. This assumption is a reasonable approximation for the globular heme proteins. As a breathing sphere, the protein's fluctuations are fully characterized by its change in radius. The changes in the protein radius are coupled to changes in the electric field at the CO due to displacement of charged and polar groups within the protein. The protein is also treated as a continuous material with a bulk modulus K_p . The viscoelastic theory shows that changes in the proteins radius are essentially instantaneously translated into changes of the electric field sensed by the CO.

The coupling between the changes in the protein radius, $\delta r_p(t)$, and the fluctuating electric field, $\delta E(t)$, are described by a proportionality constant b ,

$$\delta E(t) = b \delta r_p(t) \quad (4.4-1)$$

Within these assumptions, the time-dependent frequency fluctuations of the CO transition frequency is described by

$$\delta\omega(t) = \frac{\delta\mu_{01} \delta E(t)}{\hbar} - \langle\omega\rangle \quad (4.4-2)$$

where $\delta\mu_{01}(t)$ is the change in the dipole moment of the CO upon excitation from the ground to the first excited state and $\delta\omega(t)$ is the deviation of the transition frequency from the ensemble averaged mean frequency $\langle\omega\rangle$.

The viscosity dependence primarily manifests itself through the slowest term of the FFCF. The viscoelastic theory shows⁶⁰ that the viscosity dependence of this term is given by

$$\Delta_2 = \frac{b \delta\mu_{01}}{\hbar\sqrt{4\pi}} \left(\frac{k_B T}{3K_p r_p} \right)^{1/2} \quad (4.4-3)$$

where k_B is Boltzmann's constant, T is the temperature, \hbar is Planck's constant, and the other parameters have been defined above. Note that within this model, Δ_2 is not viscosity dependent.

$$\tau_2 = \alpha \frac{\eta}{G_\infty} \quad (4.4-4)$$

with

$$\alpha = 1 + \frac{4G_\infty}{3K_p} \quad (4.4-5)$$

G_∞ is the short-time (infinite-frequency) shear modulus. The solvent's viscoelastic behavior is characterized by a decaying shear modulus $G(t)$. However, for sufficiently short times, $G(t)$ can be approximated as G_∞ . As an estimate $K_p \approx K_\infty$, and the Cauchy relation for simple solids is used,⁹⁰ $G_\infty = (3/5)K_\infty$. Therefore, $\alpha \approx 9/5$. The central result is that τ_2 is linearly dependent on viscosity while Δ_2 is independent of viscosity. Increasing the solvent viscosity reduces the ability of the radius of the protein to change at a given frequency. In the viscoelastic model, as the viscosity is increased, the characteristic time associated with the decay of the FFCF, τ_2 , becomes longer. Fluctuations that at low viscosity occurred within the time window of the experiment (0 – 100 ps) are pushed to longer times, slowing the rate of vibrational dephasing observed in the vibrational echo experiment.

Equation (4.4-4) suggests that at infinite viscosity, τ_2 would become infinitely long, and no dephasing would occur in the experimental time window. However, for sugar-glasses the solvent is completely fixed but the protein can still undergo internal structural fluctuations that do not significantly change the protein's surface topology. The molecular origin of the protein's internal structural fluctuations have been characterized in Section 4.3.²² The fluctuations that remain even at "infinite" viscosity are very fast small amplitude local motions that give rise to a motionally narrowed component of the FFCF. These fluctuations occur at all viscosities and do not contribute to the viscosity dependence. Therefore these viscosity independent fluctuations are subtracted from the total dephasing rate to accurately determine how vibrational dephasing depends on viscosity.

The non-exponential vibrational echo dephasing decay curve for a particular T_w can be characterized by a correlation time, $T_c(\eta)$ as

$$T_c(\eta) = \frac{1}{S_{\max}(\tau; \eta)} \int_{-\infty}^{\infty} S(\tau; \eta) d\tau \quad (4.4-6)$$

where $S(\tau; \eta)$ is the vibrational echo decay signal taken at the center of the CO transition frequency as a function of delay time τ and at a fixed waiting time T_w and viscosity η . For a purely exponential signal, the correlation time reduces to the exponential decay time constant. For non-exponential decaying signals, the correlation time provides a convenient measure of the characteristic vibrational echo decay timescale. To obtain a pure viscosity-dependent correlation time, the dephasing from viscosity-independent, i.e. fructose-glass, fluctuations are subtracted out. The reduced dephasing time, $T'_c(\eta)$, at finite viscosities is given by

$$\frac{1}{T'_c(\eta)} = \frac{1}{T_c(\eta)} - \frac{1}{T_c(\eta = \infty)} \quad (4.4-7)$$

where $T_c(\eta = \infty)$ is the dephasing time of the protein confined in a fructose glass. The viscoelastic model predicts that the reduced dephasing rate should scale as $\eta^{1/3}$, which is the result of the linear dependence of τ_2 on η .⁶⁰

The viscosity dependent reduced dephasing times for the A₁ state of MbCO are presented in Figure 4.15 on a log plot. The dephasing times obtained previously using two-pulse vibrational echo experiments⁶⁰ are shown as circles, and the data acquired here using stimulated vibrational echoes with $T_w = 2$ ps are given as squares. On a log plot, data that follows a power law appears as a straight line. The line in Figure 4.15 is a power law fit to the data with the two points at the lowest viscosities from the previous experiments omitted from the fit because of insufficient time resolution (~1 ps) in those experiments. The two highest viscosity points were taken at low temperature with the influence of temperature removed.⁶⁰ The fit yields an exponent of 0.26. The reduced correlation times from three-pulse vibrational echo experiments are in generally good agreement with the two-pulse vibrational echo experiments measured previously. It is noteworthy that the measured exponent, 0.26, is relatively close to but not in agreement with the 0.33 exponent predicted by the viscoelastic model.

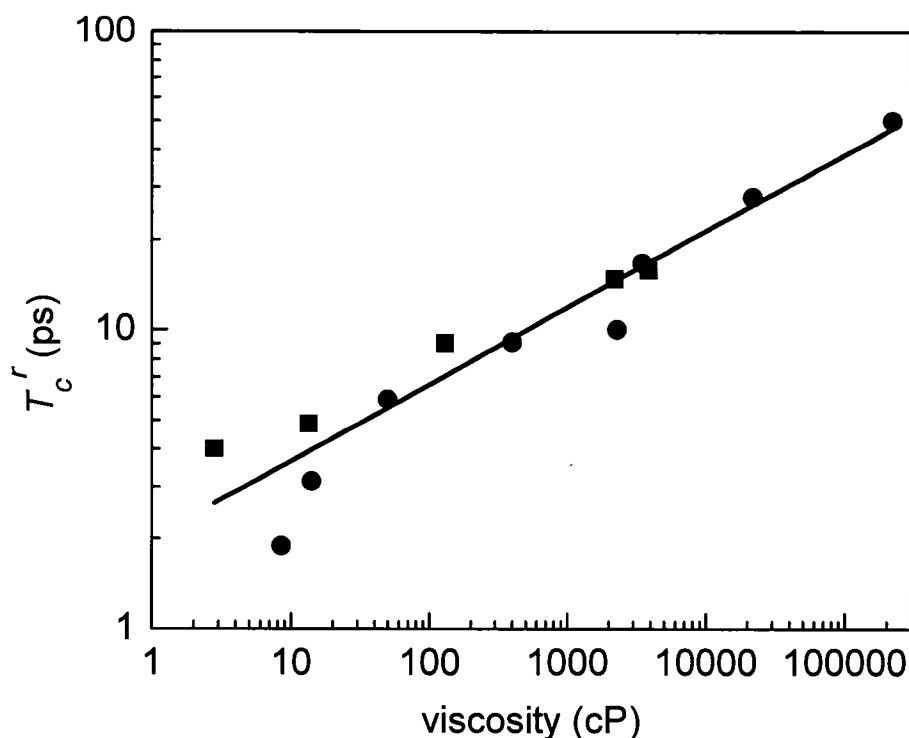


Figure 4.15 Logarithmic plot of the reduced correlation time as a function of viscosity measured for the A_1 state of MbCO using two-pulse (circles)⁶⁰ and three-pulse (squares) vibrational echo spectroscopy. The solid line is a fit of the aggregate data to a power-law model. The power-law exponent is 0.26.

The two-pulse vibrational echo is equivalent to the three-pulse vibrational echo experiments conducted here, but with $T_w = 0$. Therefore, the two-pulse vibrational echo can probe the fastest protein dynamics but is unable to observe spectral diffusion. In addition, the limited time resolution of the previous two-pulse experiments (~ 1 ps,) reduced their applicability to fast dynamics and low viscosities. The ~ 100 fs time resolution (~ 150 cm^{-1} spectral pulse width) available in the present study can probe fast dynamics and the lowest viscosities. In obtaining the A_1 reduced correlation times, the contribution from the partially overlapping A_3 state was removed using the same procedure that has been applied in other studies of MbCO.^{54,91} This procedure produced some uncertainty in the A_1 and A_3 peak shifts, and they were not included in Figure 4.14. However, $T_c^r(\eta)$ is an integral of the vibrational echo decay and was found to be insensitive to small changes in the shape of vibrational echo decay curves.

Figure 4.16 presents the reduced correlation times for the other three proteins studied, and the corresponding power law fits. The HbCO and M61A reduced correlation times have power law exponents of 0.1 and 0.13, respectively. These are substantially different from the 0.26 exponent found for the A₁ line of MbCO. The H64V gave a power law exponent of 0.21, close to that of MbCO and may be the same within experimental error. Although the actual dephasing times of H64V and MbCO are substantially different, their viscosity dependences are found to be very similar. It has been demonstrated previously that in aqueous solution H64V undergoes slower dephasing because of the removal of the distal histidine (see Chapter 3). However, the global structural fluctuations of the two proteins would be expected to be essentially the same. Since the viscosity dependence is a result of global structural fluctuations, the similarity of MbCO and H64V viscosity dependences is consistent with their having the same structural motions. In the case of myoglobin, a single point mutation in the protein interior (H64V) is not sufficient to significantly perturb the protein's structural stability or interactions with the solvent.

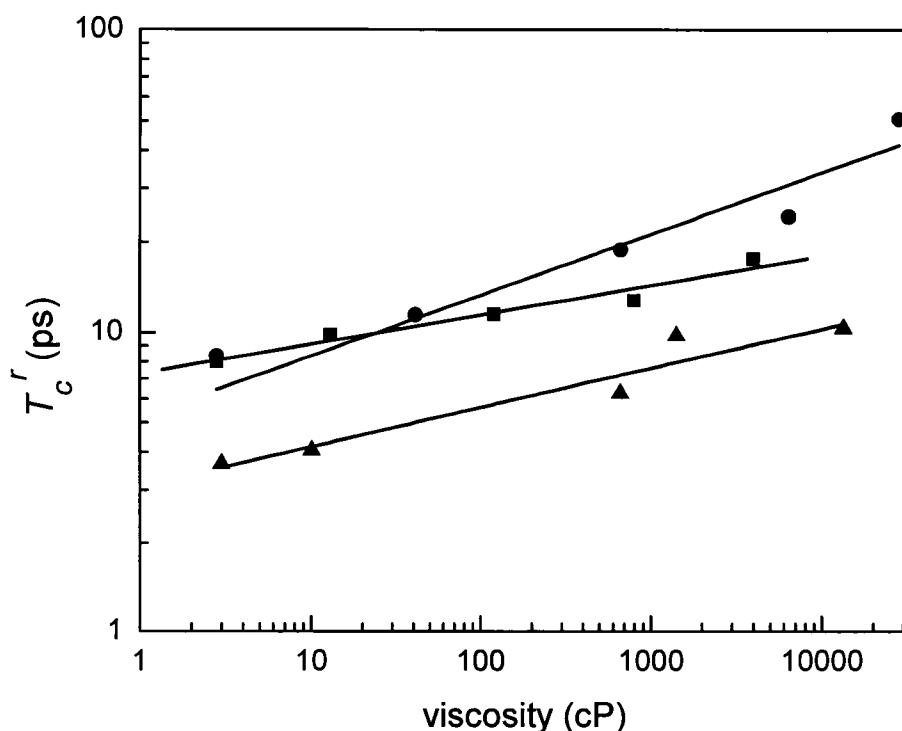


Figure 4.16 Logarithmic plots of the reduced correlation time for M61A (triangles), HbCO (squares) and H64V (circles). The lines represent power law fits given: M61A power law exponent 0.13; H64V power law exponent 0.2; and HbCO power law exponent of 0.1.

The results presented in Figure 4.16 show that the viscoelastic model's prediction of a 0.33 exponent over estimates the viscosity dependence of the protein dynamics. The model captures the fact that the viscosity dependence is mild, but the results show that there can be substantial deviations from the $\eta^{1/3}$ dependence. HbCO exhibits the weakest viscosity dependence. We conjecture that this may be related to the intra-protein cavity that can permits large scale protein deformations to persist even at the highest viscosities. Although the surface topology of HbCO is constrained by the solvent, the protein can continue to transiently occupy the intra-cavity region. This conjecture could be tested by studying the viscosity dependence of CO dephasing in HbCO with a small-molecule effector, such as bezafibrate (BZF), introduced into the protein cavity. M61A also displays weak viscosity dependence although not as weak as HbCO. Because M61A belongs to a different class of heme proteins than the other three proteins in this study, it is possible that the internal rigidity of this protein differs from the other proteins. As a result, the relevant structural dynamics are coupled differently to the surrounding solvent. This idea is supported in the detailed analysis presented below by the fact that the viscosity dependent dynamics in M61A are in general larger in amplitude and slower than those of the other three proteins studied.

The relationship between the vibrational dephasing rate and protein structural fluctuations is highly non-linear. A weak viscosity dependence of $T_C^r(\eta)$ may understate the underlying influences on protein structural dynamics that are caused by a change in viscosity. Structural rearrangements of protein residues cause time-dependent fluctuations in the transition frequency of the CO. The FFCF is a precise way to characterize these CO frequency fluctuations. Although protein structural fluctuations evolve over a continuum of timescales, the FFCF organizes these timescales into a finite set of fluctuation rates and relative amplitudes. The FFCF of each protein at a given viscosity was obtained by simultaneously fitting the linear absorption spectrum and a family of vibrational echo decays at several T_w s at the

spectral center frequency, as described in Section 4.2.5. The fits to the data used to extract the FFCFs for each protein are very good (see, for example, Figure 4.5).

In all four proteins at all viscosities, the FFCF was found to contain a fast (sub-100 fs) process that is motionally narrowed on the experimental timescales, and a slower (several ps) process that describes larger-amplitude protein fluctuations.²² The protein structural fluctuations that give rise to the fast exponential in the FFCF are identified as viscosity independent protein fluctuations that persist even for proteins in sugar-glasses. We have earlier elucidated the nature of these fluctuations through a combination of vibrational echo experiments and MD simulations.²² These fluctuations can be pictured as uncorrelated small scale displacements of protein atoms and small groups from their equilibrium positions without significant deformations in the overall protein structure. These processes are nearly decoupled from the solvent environment and are thus independent of solution viscosity. They will contribute a viscosity independent term to the FFCF. The viscosity independent contribution to the FFCF was obtained by fitting the vibrational echo data for the proteins encased in a fructose film. The sub-100 fs exponential dominates the FFCF. After the viscosity independent part of the FFCF was obtained from the fructose-glass samples, it was not allowed to vary when fitting the protein dynamics at all subsequent viscosities. This procedure allows us to evaluate a reduced FFCF that reflects only the viscosity dependent contribution to the total protein dynamics (in analogy to $T'_C(\eta)$).

Figure 4.17a and b display the magnitude, $\Delta_2(\eta)$, and timescales, $\tau_2(\eta)$ of the FFCF (Equation (4.2-1)). The motionally narrow term in the FFCF, $\Delta_1^2 \exp(-t/\tau_1)$, is independent of viscosity. The data is presented for HbCO, M61A and H64V. The error-bars indicate typical uncertainties in the fit values. The uncertainty in the timescales of the protein fluctuations increases at higher viscosities because the viscosity dependent part of the FFCF contributes significantly less to the overall vibrational echo signal than the viscosity independent component. As viscosity is increased, the magnitude of the protein fluctuations (Δ_2) decreases while the characteristic timescale of these processes (τ_2) gets longer. The vibrational echo detects structural evolution on timescales shorter than ~ 100 ps; slower process will

appear as if they are static in these experiments. The decrease in the magnitude of Δ_2 and shift of these fluctuations to longer times is consistent with an overall redistribution of the continuum of protein dynamics to longer timescales. All three proteins show a monotonic decrease in Δ_2 (the amplitude of the observed viscosity dependent fluctuations) that could be well described by a weak power law with an exponent of 0.1 ± 0.01 . H64V and M61A also exhibit a mild, monotonic lengthening of the timescale of frequency fluctuation. In the case of HbCO, the timescale of fluctuations, τ_2 , is unchanged between ~ 10 -1000 cP, within the relatively large experimental uncertainty. This is consistent with HbCO dynamics being the least sensitive to viscosity. Vibrational echo experiments examining the effects of confinement in a nanoscopic water environment of MbCO and HbCO showed that HbCO dynamics were influenced substantially less than the MbCO dynamics (see below).⁸³

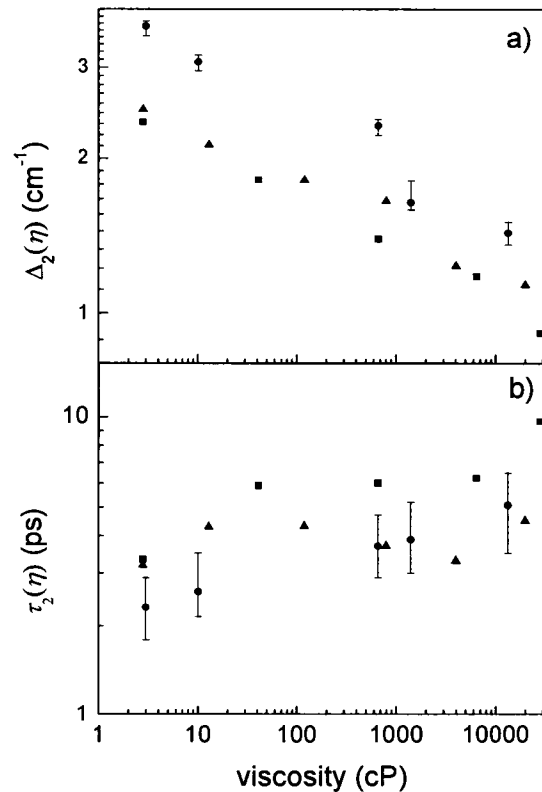


Figure 4.17 The viscosity dependent contribution to the FFCF for HbCO (triangles), H64V (squares), and M61A (circles). (a) The amplitude of the frequency perturbations Δ_2 and (b) the corresponding timescales over which these fluctuations evolve, τ_2 . The error bars indicate typical uncertainties in the fits. The data are presented on logarithmic scales.

In the viscoelastic model describing the influence on the vibrational echo observables of the viscosity dependence of protein structural fluctuation, the magnitude of frequency fluctuations (Δ_2) in the FFCF is not dependent on solution viscosity (see Equation (4.4-3)), but the characteristic timescale of the fluctuations, τ_2 , scales linearly with viscosity (see Equation (4.4-4)).^{60,87} These predictions are in disagreement with the experimentally determined FFCFs components, Δ_2 and τ_2 shown in Figure 4.17. It was found that in the three proteins in which the components of the FFCF were determined, the Δ_2 s varied with viscosity in all three. τ_2 has a much weaker than linear dependence, and for HbCO may be viscosity independent. Although the viscoelastic model does not reproduce the quantitative trends observed in the experiments, it properly predicts that the viscosity dependence of the protein dynamics should be very weak. There were a number of simplifying assumptions in the current form of the viscoelastic model. The protein was taken to be a uniform breathing sphere characterized only by K_p , the bulk modulus of the solvent was ignored, and the infinite viscosity approximation to the shear modulus was employed. It is possible that an improved viscoelastic theory would more accurately capture the experimental results.

4.5 DYNAMICS IN A NANOSCOPIC WATER POOL

4.5.1 *Vibrational Echo Experiments*

The linear absorption spectra for wild type MbCO and HbCO in a sol-gel nanopore are indistinguishable from that of the aqueous protein samples. Changing the R -value (see Table 4.1) over the range of 15 to 39 and 15 to 27 for MbCO and HbCO, respectively, does not affect the FT-IR spectra for either protein (data not shown). The Gaussian shape of the spectral bands in both proteins suggests that these transitions are inhomogeneously broadened, which would obscure any dynamical information contained in the linear spectra. Vibrational stimulated echo experiments described below reveal the underlying dynamical differences that exist for these proteins between aqueous and sol-gel glass environments on the ultrafast timescale.

Figure 4.18 displays vibrational echo data taken with $T_w = 0.5$ ps for MbCO encapsulated in a sol-gel glass ($R = 15$, dashed line) and in aqueous solution (solid line). For clarity, a single T_w is presented in Figure 4.18. The data demonstrate that the vibrational echo decay for the sol-gel sample is significantly slower than for the aqueous sample. Within the dynamic Stark effect model described previously, this is the result of slower modulations of the net electric field generated by the entire protein and surrounding solvent at the heme-bound CO.

Increasing the R -value for the sol-gel preparation has been reported to decrease the pore diameter by increasing the degree of silica cross-linking.^{25,45,92,93} However, the vibrational echo decays for MbCO sol-gel samples at all R -values listed in Table 4.1 are the same (only $R = 15$ data are shown). As discussed below, the changes observed in the protein dynamics can be accounted for by a change in the “effective viscosity” of the water in the sol-gel pore. It has been demonstrated by direct experiments on water in reverse micelles⁹⁴⁻⁹⁶ that water dynamics are very sensitive to confinement on nanoscopic length scales, and vary in a manner that resembles an increase in effective viscosity with a decrease in pore size. As discussed in Section 4.4, protein dynamics are known to be sensitive to the viscosity of the surrounding solvent.^{22,60} Therefore, to explain the independence of structural dynamics on the pore size, it is highly unlikely that the protein dynamics are simply insensitive to the size of the surrounding pore. As discussed further below, the likely explanation is that the sol-gel matrix is templated around the protein and, while the average “empty” pore diameter may change with R -value, the size of pores formed around proteins is dictated by the size of the protein and is independent of R .^{27,28,31,34,97}

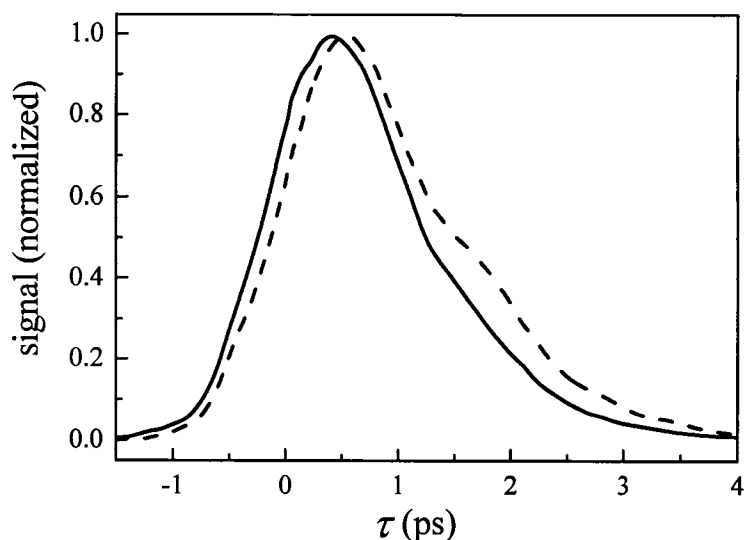


Figure 4.18 Spectrally-resolved vibrational echo decays at $T_w = 0.5$ ps for CO bound to aqueous (solid line) and sol-gel encapsulated MbCO (dashed line) at 1945 cm^{-1} .

The vibrational echo decays at $T_w = 0.5$ are shown for aqueous and sol-gel encapsulated HbCO in Figure 4.19. Although the change is not as dramatic as MbCO, the dephasing rate is noticeably slower for proteins encapsulated in sol-gel glasses. Studies on HbCO over many decades of viscosities in a single solvent environment demonstrated that HbCO does indeed have a measurable, albeit weak, viscosity dependence. That the sol-gel environment has a weaker influence on the HbCO structural dynamics, as sensed by the heme-bound CO, may be due to the quaternary level of structural organization in this protein. Having only tertiary structure, the entire surface area of MbCO is in contact with the solvent or silica pore walls. In contrast, HbCO is a tetramer of tertiary subunits, each of which is structurally similar to MbCO. Therefore, each heme-containing subunit is partially “solvated” by the other three subunits and should be less sensitive to the properties of the surrounding solvent. Sottini and coworkers have also noted that proteins with a larger surface-to-volume ratio are expected to experience a greater degree of friction from their surrounding solvent environment.⁹⁸ Previous vibrational echo studies confirm the weaker dynamic response of HbCO to the viscosity of the surrounding environment.^{55,74,79,98}

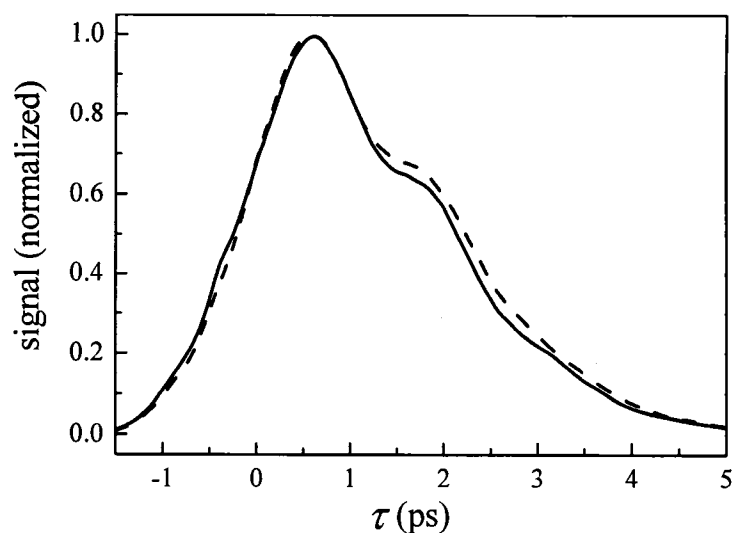


Figure 4.19 Spectrally-resolved vibrational echo decays at $T_w = 0.5$ ps for CO bound to aqueous (solid line) and sol-gel encapsulated HbCO (dashed line) at 1951 cm^{-1} .

The vibrational echo peak shifts for MbCO are shown in Figure 4.20a as a function of T_w . The peak shift values for sol-gel encapsulated MbCO ($R = 15$, circles) are consistently larger than those for the aqueous protein (squares). Figure 4.20b displays the vibrational echo peak shifts for HbCO, which are also greater for the sol-gel encapsulated proteins than those for the aqueous protein solution. These figures show that the impact of sol-gel encapsulation, as measured by the magnitude of the vibrational echo peak shift, is greater at all T_w s for MbCO than for HbCO compared to the proteins in aqueous solutions. At each T_w , both proteins in aqueous solution have sampled a greater fraction of the inhomogeneously broadened spectral line, and therefore a greater fraction of accessible structures, than the sol-gel encapsulated samples. The T_w dependent results are consistent with the faster dephasing shown for the aqueous proteins relative to their sol-gel encapsulated forms in Figure 4.18 and Figure 4.19. The R -values used to prepare the sol-gels were found to have no significant effect on the T_w dependent vibrational echo decays for either protein (data not shown).

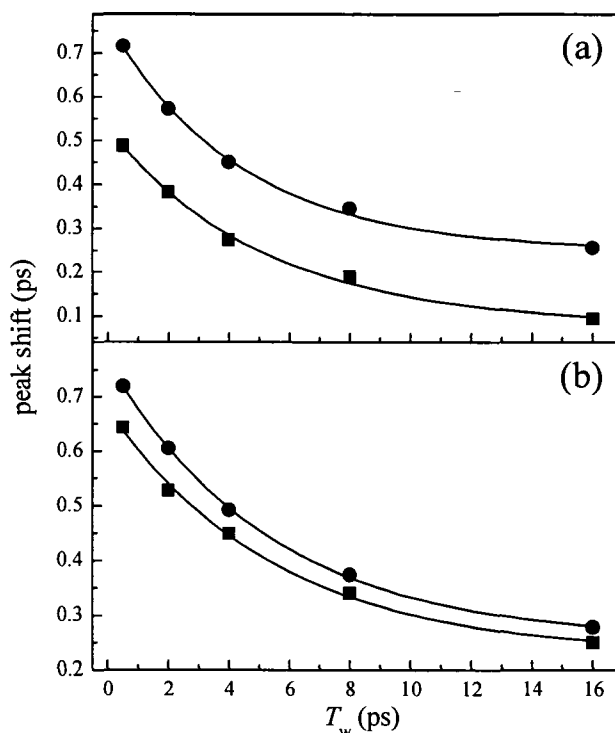


Figure 4.20 Vibrational echo peak shifts as a function of T_w for a) MbCO and b) HbCO in aqueous and sol-gel encapsulated environments. In both frames, the filled squares represent the aqueous protein data and the filled circles represent the sol-gel encapsulated protein peak shifts. The solid lines represent single exponential fits to the data with time constants of a) 5.2 ± 0.7 and 4.4 ± 0.4 ps for aqueous and sol-gel encapsulated MbCO and b) 5.6 ± 0.7 and 5.4 ± 0.2 ps for aqueous and sol-gel encapsulated HbCO, respectively.

To compare the shapes of the proteins' vibrational echo peak shift curves, the aqueous and sol-gel encapsulated MbCO data were fit as single exponential decays plus a constant with time constants of 5.2 ± 0.7 ps and 4.4 ± 0.4 ps, respectively. For the aqueous and sol-gel encapsulated HbCO, single exponential decay time constants of 5.6 ± 0.7 ps and 5.4 ± 0.2 ps, respectively, were obtained. The constant offsets for all vibrational echo peak shift plots are indicative of the quasi-static frequency fluctuations that occur on timescales that are longer than several lifetimes. Therefore, within error, the rates at which the vibrational echo decay peaks are shifting towards the origin for MbCO and HbCO are the same for each protein in aqueous and sol-gel encapsulated environments. This demonstrates that the protein dynamics, as sensed by the heme-bound CO, that occur on timescales longer than a few ps are virtually unaffected by the sol-gel encapsulation; the primary influence of the sol-gel matrix on

the dynamics in both proteins occurs within the time range of a single vibrational echo decay (several ps). Therefore, the ultrafast structural dynamics of both MbCO and HbCO are affected in a similar manner by surrounding environment: The vibrational dephasing rate is decreased (timescale of ~ 100 fs to several ps) while spectral diffusion remains approximately the same (timescale of tens of ps).

That the fast dynamics of both proteins are sensitive to the sol-gel pore environment while the tens of ps dynamics are unaffected is a dynamical trend that is consistent with a viscosity effect at relatively low viscosities. In this context, the results shown above can be compared to data taken on MbCO and HbCO, in aqueous/fructose solutions in which the concentration of fructose was increased to increase the viscosity (see Section 4.4). The quantitative description of the viscosity dependence of HbCO and the A_1 state of MbCO, manifested in their viscosity dependent FFCFs, allows the calculation of vibrational echo decays for aqueous solutions with any viscosity. The FFCF parameters calculated at discrete viscosity points vary smoothly, which allows FFCF parameters at other viscosities to be obtained by interpolation. In Figure 4.21, the measured vibrational echo decays for aqueous and sol-gel encapsulated MbCO at $T_w = 0.5$ ps (reproduced from Figure 4.18) are overlaid with calculated vibrational echo data for the protein in 2.5 cP (aqueous solution with the protein) and 45 cP solutions. It is clear that the echo decays calculated at these viscosities are in good agreement with those measured for aqueous and sol-gel encapsulated MbCO. This demonstrates that the effective viscosity experienced by MbCO in the sol-gel matrix is ~ 20 times greater than the protein in aqueous solution. In contrast, only a 2-fold increase (1.5 cP to 3 cP) in effective viscosity is produced by sol-gel encapsulation of HbCO at $T_w = 0.5$ ps (Figure 4.21b).

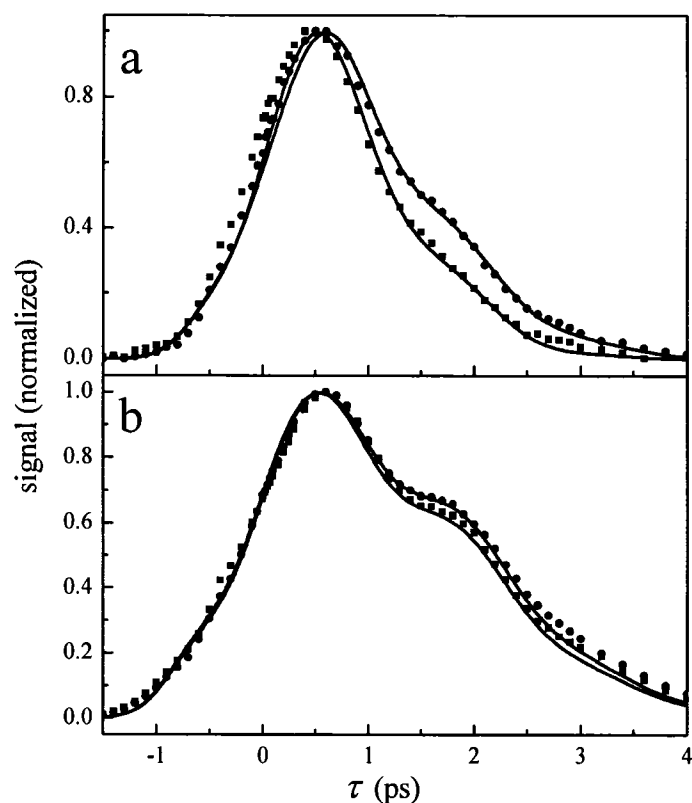


Figure 4.21 a) Spectrally-resolved vibrational echo decays at $T_w = 0.5$ ps for aqueous (squares) and sol-gel encapsulated MbCO (circles) at 1945 cm^{-1} . The overlaid solid lines are calculated vibrational echo decays at $T_w = 0.5$ ps in aqueous solvent viscosities of 2.5 and 45 cP to match the experimental aqueous and sol-gel data. b) Spectrally-resolved vibrational echo decays at $T_w = 0.5$ ps for aqueous (squares) and sol-gel encapsulated HbCO (circles) at 1951 cm^{-1} . The overlaid solid lines are calculated vibrational echo decays at $T_w = 0.5$ ps in aqueous solvent viscosities of 1.5 and 3 cP to match the experimental aqueous and sol-gel data.

The absence of an R -dependence (pore size dependence) in the measured vibrational dephasing and spectral diffusion is consistent with templating of the silica matrix around the protein and the production of a thin layer of surrounding water during the sol-gel encapsulation process. In this manner, the pore dimension is determined at the gelation point by the size of the protein, and is unaffected by the R -value used to prepare the silica matrix. Rotational anisotropy measurements of water confined to nanoscopic pores in reverse micelles can be used to obtain a rough approximation of the thickness of the water layer that surrounds the proteins in sol-gel glasses.⁹⁴ The Debye-Einstein-Stokes equation⁹⁹ predicts that the rotational correlation time (τ) is directly proportional to the viscosity (η) of the solution. Since

the effective η is known to increase with decreasing confinement length,⁹⁴ these results imply that MbCO is surrounded by a thinner layer of water than HbCO. Using the rotational correlation times reported by Tan and coworkers,⁹⁴ it is estimated that water confined to a length dimension of less than ~ 2 nm is required to obtain the 45 cP aqueous environments estimated for the water surrounding sol-gel encapsulated MbCO. Although this approximation ignores the protein interactions with the silica pore walls and treats the water layer thickness as the diameter of a sphere, it is not unreasonable to expect that silica polycondensation that is template-directed by a nanoscopic protein would produce interstitial solvent space of these dimensions. Using the same procedure, it is estimated that sol-gel encapsulated HbCO is surrounded by a layer of water that is ~ 5 nm thick. These distances are rough estimates because the comparisons to AOT reverse micelles⁹⁴ ignore the differences in the interfacial structure of AOT (ionic) and the sol-gels (not ionic).

It is surprising that, within the approximations used above, the dephasing dynamics of sol-gel encapsulated HbCO reflect a surrounding water layer that is ~ 3 times thicker than that of MbCO. One possible explanation for this phenomenon is that the folded structure of HbCO becomes partially denatured during the encapsulation process. This would result in an increased protein volume at the point of silica templating. It has been estimated that the radius of gyration for a protein can change by as much as 50% upon folding from a denatured state.¹⁰⁰⁻¹⁰² As the silica matrix crosslinks and generates water through polycondensation, the protein refolds into a more compact structure, which increases the thickness of the surrounding water layer. The water pool is generated by the silica polycondensation reactions as well as the hydrophobic collapse that expels water from the hydrophobic regions of the folding protein. Although the conditions used to prepare the sol-gel encapsulated proteins in this study minimize the denaturing conditions, both encapsulated proteins are initially prepared in a low pH solvent amidst a process that generates methanol. It has been noted that myoglobin has a higher stability toward denaturation than hemoglobin,¹⁰³ and is therefore feasible that HbCO partially denatures and refolds while MbCO remains compact during the encapsulation procedure. It is important to

note that the IR spectra, which are very sensitive to structure, indicate that the proteins prepared in sol-gel glasses were in their correctly folded states at the point of data collection.

In addition to an increased viscosity for the surrounding solvent, it is reasonable to expect that the proteins in this study have some degree of interaction with the pore walls. As noted above, the hindered rotation of proteins in silica sol-gel pores results from substantial interactions between the protein exterior and the hydrophilic pore walls.^{97,104,105} Nonetheless, the stimulated vibrational echo data shown above for MbCO and HbCO encapsulated in sol-gel glasses are *not* representative of proteins whose surfaces are completely immobilized by a glassy matrix. Vibrational echo spectroscopy and molecular dynamics simulations for several heme proteins in trehalose glasses have demonstrated that nearly all of the structural dynamics slower than a few hundred fs are effectively turned off when the protein surface is fixed.²² Furthermore, the linear IR spectra showed static frequency shifts and increased inhomogeneous broadening indicative of locking the proteins into many structural configurations. In contrast, the steady-state and vibrational echo data in silica sol-gel glasses reveal proteins in an environment that is similar to an aqueous environment with an increased viscosity. The distinction between protein dynamics in sol-gel and trehalose glasses has been noted previously by Abruzzetti and coworkers,⁴² and is evidence that, while some pore wall interactions prevent global macromolecular rotation, a large fraction of the protein surface remains in contact with the nanoscopic water surrounding the protein in the pore.

Finally, although the protein dynamics in sol-gel glasses are very different from a protein encased in a trehalose glass, it is notable that the mechanism by which the structural fluctuations are damped in these two systems may not be completely dissimilar. The protein immobilizing effect of a trehalose glass has been shown to occur by an indirect mechanism in which the trehalose matrix constrains a thin layer of water at the surface of the encapsulated protein.^{8,16,20,22} The drastic reduction in fast dynamics in a trehalose glass²² is perhaps an extreme example of the dynamic effect

observed in the vibrational echo measurements for a protein in a sol-gel pore surrounded by a substantially thicker layer of confined water.

Recently MD simulations on H64V attempted to unambiguously determine the molecular origin of the measured structural dynamics in sol-gel confinement.¹⁰⁶ The sol-gel pore was modeled by a pool of dynamic water around the protein molecule surrounded by a disordered layer of static water (analogous to the static water simulations described in Section 4.3.3). The FFCF was computed for several cases with increasing amounts of dynamic water. The simulations point to a striking observation: only a few hydration layers of water (~1000 molecules) are necessary to completely recover the aqueous protein dynamics. Taken in conjunction with the experimental results for MbCO and HbCO, we conclude that sol-gel pore formation confines MbCO drastically, with just a ~2 aqueous solvation layers around the protein. In contrast, sol-gels templated around HbCO maintain several layers of water around the protein.

4.6 HEMOGLOBIN IN HUMAN ERYTHROCYTES

After characterizing the influence of the nanoscopic environment on protein dynamics in sol-gel glasses and as a function of viscosity, we decided to measure the influence of molecular crowding on protein dynamics in human red blood cells (erythrocytes). Hemoglobin is the principal component of human erythrocytes, and occupies the bulk of the cell volume. It was expected that the degree of molecular confinement due to the high hemoglobin concentrations would impact the magnitude of protein structural fluctuations.

A seemingly insurmountable experimental challenge in measuring the dynamics of human erythrocytes is the significant light scattering of the 5 μm vibrational echo input pulses by the ~6 - 8 μm erythrocytes. Below, we detail a strategy that used the phase sensitivity of the vibrational echo signal to significantly reduce the noise due to scattered light.

4.6.1 Strategy for Removing Scattered Light

The effect of this scattered light on the vibrational echo signal as a function of τ (the delay between the first two pulses in the vibrational echo pulse sequence) is shown in Figure 4.22 by the solid curve. To obtain spectral resolution of the signal, the vibrational echo pulse is dispersed by a monochromator. By spectrally resolving the vibrational echo, analysis is simplified and additional information is obtained.^{54,56} Furthermore, it is possible to greatly reduce the influence of higher order (5th order) non-linear effects on the vibrational echo signal.¹⁰⁷ The monochromator reduces the amount of scattered light because the detector only sees the light at the detection wavelength. The scattered light contribution to the detected signal is dependent on τ . Light entering the monochromator is temporally stretched (to ~ 10 ps), resulting in overlap of the scattered light and the vibrational echo wave packet over a wide range of τ delays. The electric field of the scattered light interferes with the electric field of the vibrational echo. As the delay between the first two excitation pulses is scanned, the phase of the vibrational echo electric field is advanced relative to the fixed scattered light electric fields from the second and third pulses. The result is alternating constructive and destructive interference between the vibrational echo and the scattered light. The interference produces the amplitude variations in the solid curve in Figure 4.22.

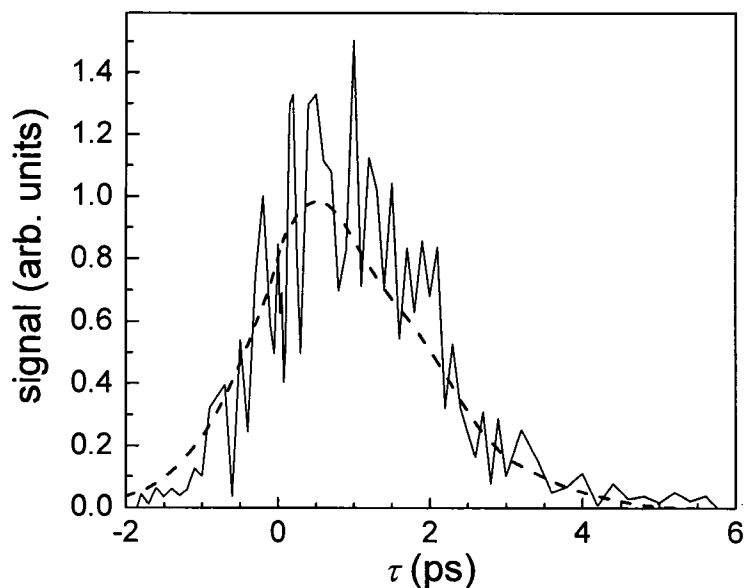


Figure 4.22 Spectrally resolved stimulated vibrational echo decays at 1951 cm^{-1} from HbCO in erythrocytes. The solid curve is data taken in the standard manner and displays strong modulations caused by the heterodyned interference of scattered light with the vibrational echo signal. The dashed curve shows the vibrational echo signal collected using the new “fibrillation” method described in the text.

The variations in the solid curve in Figure 4.22 are not noise in the usual sense. The solid curve is the average of many scans. As long as the path lengths do not change, the phase relationships between the vibrational echo electric field and the scattered light electric fields are fixed. Because of the massive light scattering produced by the erythrocytes, some scattered light is collinear with the vibrational echo and cannot be completely eliminated by spatial filtering. To obtain a feel for the severity of the problem consider the following example. If the intensity of the vibrational echo pulse is 100 times larger than the scattered light, then at the electric field level the ratio is only 10 to 1. The cross term responsible for the modulation is $2ES$, where E is the vibrational echo electric field, and S is the scattered light electric field. Because the two electric fields go in and out of phase, the $2ES$ cross term swings positive and negative, doubling the amplitude of the modulation. Therefore, if the scattered light is 1% of the vibrational echo in intensity, a 40% modulation will occur.

Because the first pulse initiates the dephasing of the CO stretching vibration, the rephased vibrational ensemble (after the third pulse) that gives rise to the vibrational echo signal is inherently phase-locked to the first pulse. Therefore, the vibrational echo signal is not modulated by scattered light from the first pulse. The phase relationship between the first pulse and the vibrational echo electric field provides a method for eliminating the swings in the data, making it possible to average the scattered light contribution to zero. To remove the modulations, a piezo-electric translator (PZT) is used to vary the distance traveled by pulse 1 by changing the position of a retroreflector along the optical axis. The PZT scans the distance by 1/2 wavelength (2.5 μm). The scanning is done asynchronously with the laser repetition rate. The scan varies the phase of pulse 1, and therefore the vibrational echo pulse, by 180°. At each point in the τ scan delay, many shots are collected and averaged. Because the vibrational echo electric field varies in phase asynchronously with respect to the fixed phases of the scattered light electric fields, the interference induced variations are averaged out. We refer to this procedure as fibrillation. Fibrillation reduces the time resolution of the experiment by the time required for light to travel 1/2 wavelength, in this case, 8.5 fs. In the current experiments, the reduction in resolution is negligible. The dashed line in Figure 4.22 is the vibrational echo data taken with fibrillation. It is clear that coherent scattered light interference has been eliminated. Vibrational echo experiments with fibrillation of non-scattering aqueous samples were performed and there were no noticeable differences in the decays. The fibrillation method is important because it makes it possible to perform vibrational echo experiments on highly scattering samples.

4.6.2 Hemoglobin Dynamics in an Erythrocyte

It has been established that the hemoglobin concentration (in heme; four times the protein concentration) inside the erythrocyte is 21 mM (33.5 g/dL).¹⁰⁸⁻¹¹¹ Increasing the concentration of a protein in aqueous solution increases the solution's viscosity. Reported viscosities inside erythrocytes range from 10 cP to 15 cP.^{108,112,113} However, these results are from indirect measurements that infer the protein's

viscosity by measuring the relaxation time of a stretched cellular membrane¹¹³ or on solutions prepared without removal of large aggregates and particulates.¹¹⁴ Section 4.4 outlined that the HbCO dephasing dynamics were sensitive to the solution viscosities. Therefore, in comparing the dephasing dynamics of HbCO in erythrocytes and in solution it is necessary to consider the viscosity of the medium.

Hemoglobin occupies nearly 70 percent of the volume of an erythrocyte, dominating the internal cellular viscosity. In order to obtain the viscosity inside a red blood cell, studies were performed on aqueous hemoglobin solutions at a variety of concentrations. Before viscosity measurements were made, the solutions were centrifuged and passed through 0.45 μm filters to remove particulates. The concentration was then precisely determined by visible absorption spectroscopy on the met form of the protein. Figure 4.23 shows a plot of hemoglobin concentration (in heme) versus measured viscosity (circles). It is important to note that the measured viscosity for aqueous hemoglobin solutions is higher than reported cellular viscosities at concentrations below the known cytoplasmic hemoglobin concentration. Using this method, the highest solution concentration that could be achieved was 17 mM. To determine the viscosity inside of an erythrocyte, an extrapolation to higher concentrations was needed.

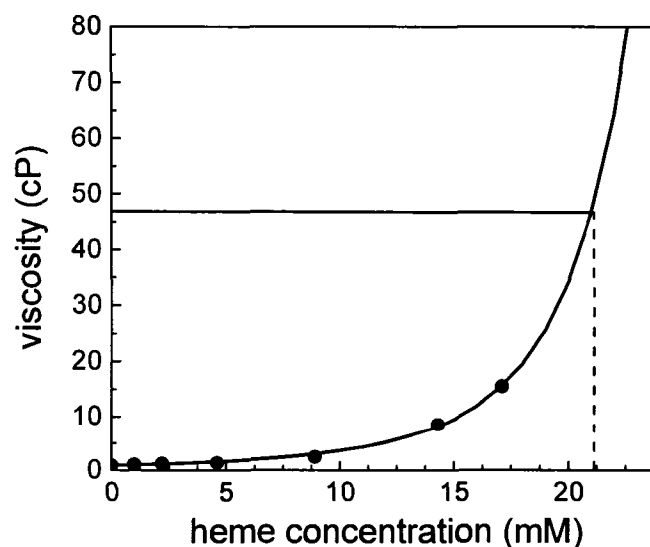


Figure 4.23 Measured Hb solution viscosity (circles) vs. concentration at 298 K. The solid curve is a fit to the experimental data (see text). The lines show that the viscosity is ~ 46 cP at 21 mM in heme (5 mM hemoglobin) concentration found inside red blood cells.

A model by Mooney,¹¹⁵ which is an extension of the Einstein viscosity model for hard spheres,¹¹⁶ was used with empirical parameters to predict the viscosity inside an erythrocyte. The functional form of the model is given in below

$$\eta = a_0 e^{\left(\frac{a_2 c}{1 - a_1 a_2 c}\right)} \quad (4.6-1)$$

where η is the predicted viscosity, c is the concentration, a_0 is the intrinsic solvent viscosity (0.8909 cP at 25° C for water), and the inverse packing fraction and the hydration shell radius of the protein are represented by a_1 and a_2 , respectively. The model was fit to the experimentally measured viscosities in Figure 4.23 (solid curve) with a_1 and a_2 as adjustable parameters. The fit is very good. The fit was extrapolated to the erythrocyte hemoglobin concentration of 21 mM (dashed line), yielding a viscosity of 46 ± 6 cP.

Figure 4.24 shows the vibrational echo decay curves for high concentration aqueous (17 mmol/L, solid curve) and intracellular (4 mmol/L, dot-dashed curve) HbCO. The data in Figure 4.24 (left panel) display an oscillation as evidenced by the shoulder at ~ 1.8 ps and a “flattening” at ~ 3.4 ps. The oscillation occurs at the frequency of the HbCO vibrational anharmonicity (25 cm^{-1}),^{79,107,117} and is the result of an accidental degeneracy beat (ADB).^{118,119} The ADB mechanism has been described in detail^{118,119} and requires the overlap of the 0-1 transition of one substate with the 1-2 transition of a second substate. In HbCO, the 1-2 transition of the CIV substate (1944 cm^{-1}) overlaps the 0-1 transition of the CIII substate (see Fig. 1 and Fig. 2b of Ref. 24). The relative amplitudes of the two absorption bands determine the magnitude of the beat. Because the relative amplitude in aqueous solution is 10:1, the beat is relatively small. However, in the erythrocyte, the relative amplitudes of the CIII and CIV absorption bands are 100:1, the beat is much smaller, and barely discernable

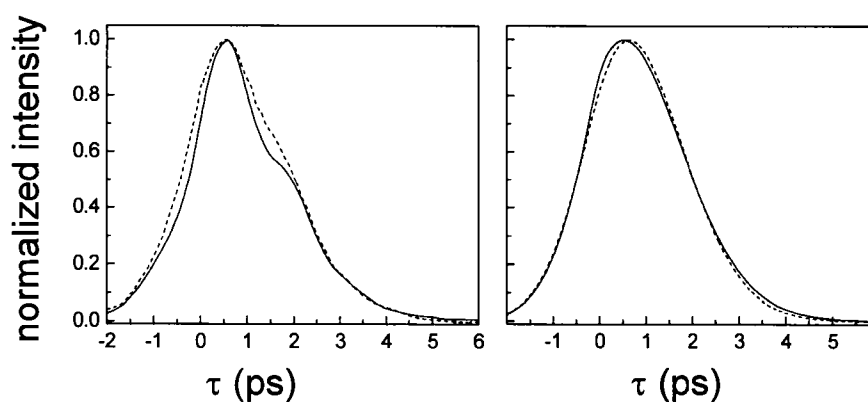


Figure 4.24 Vibrational echo decays of aqueous HbCO (solid curve) and cytoplasmic HbCO (dashed curve) at $T_w = 2$ ps. The larger amplitude beat on the aqueous data in the left panel makes the decay look faster than the cytoplasmic decay. Right panel: The calculated decays for aqueous HbCO (solid curve) and cytoplasmic HbCO (dashed curve) with the contribution from the blue substate that causes beats removed. Within experimental error, the decays are indistinguishable demonstrating that the aqueous and cytoplasmic HbCO dynamics are identical.

The difference in the magnitudes of the beats for the aqueous and cytoplasmic samples prevents direct comparison of the vibrational echo decay curves. To extract decays from the data so that the HbCO dynamics can be compared, the ADBs must be removed. The method for beat removal is based on calculating the non-linear signal using diagrammatic perturbation theory and has been described extensively elsewhere.⁶⁶ The calculated decays of the aqueous (solid curve) and cytoplasmic HbCO (dashed curve) with the beats removed from the calculations are shown in Figure 4.24 (right panel). Within experimental error and the small uncertainty introduced by having to fit the data and remove the beats, the curves show nearly perfect agreement. The agreement demonstrates that the protein structural fluctuations sensed by the CO ligand bound at the active site are the same in aqueous and cytoplasmic hemoglobin over the picoseconds timescale of the experiments. Increasing the time between the second and third pulses increases the timescale of the experiment. Experiments conducted with the delay between the second and third pulses extended to 16 ps showed no discernable differences between the cytoplasmic HbCO and the aqueous HbCO dynamics.

4.7 CONCLUDING REMARKS

Proteins are complex macromolecules that undergo structurally significant fluctuations with timescales spanning many orders of magnitude. The 2D-IR vibrational echo experiments and MD simulations presented in this chapter systematically probed the structural fluctuations of several proteins in several different types of confinement. The ultrafast infrared vibrational echo measurements of HbCO, H64V and *Ht*-M61A in aqueous and trehalose matrix environments have revealed some universal aspects of solvent-protein dynamics. Compared to aqueous protein solutions, vibrational dephasing of the heme-bound CO is significantly reduced for all three proteins embedded in trehalose glasses. Nonetheless, confinement in a room temperature glass is insufficient to completely turn off all protein dynamics. The fact that locking the exterior surface of the protein affects the observed CO dynamics indicates that the bound CO ligand is either directly or indirectly sensitive to changes in protein structure that occur nanometers away from the active site. MD simulations of H64V were carried out to generate an atomistic description of vibrational dephasing in aqueous and static environments. With experiment and simulation in agreement, we were able to determine that the suppression of long timescale frequency fluctuations (spectral diffusion) is the result of a damping of atomic displacements throughout the protein structure, and is not isolated to structural dynamics that occur only at the protein surface.

To extend our understanding of the influence of the surrounding medium on protein structural dynamics, four heme proteins with three different distal residues were studied in solutions with viscosities that ranged over ~ 5 orders of magnitude. In all cases it was found that the viscosity dependence was relatively weak over the time window examined in the experiments, ~ 100 fs to ~ 100 ps. The protein dynamics can be divided into two classes. One type is ultrafast very local fluctuations that do not depend on viscosity and remain at high viscosities and even persist in sugar glasses. The other type is slower larger amplitude fluctuations that require protein surface topology changes; these are affected by viscosity. Increasing viscosity reduces the presence of these larger amplitude fluctuations and lengthens the characteristic

timescale of the fluctuations in the time window investigated. These results indicate that the fast fluctuations are slowed and shifted to longer timescales. The changes with viscosity are quite similar for the proteins studied although the details of the actual fluctuation dynamics vary among the proteins. In the context of the vibrational echo experiments, increasing the viscosity shifts the fluctuations to longer timescales, thereby moving them outside of the experimental observation window where they contribute to the inhomogeneous broadening component of the total lineshape. The vibrational echo results presented here give a detailed view of how structural dynamics are influenced by changes in viscosity. These results can serve as quantitative experimental data to test simulations and our overall understanding of protein dynamics.

Building on the extensive 2D-IR data collected for proteins as a function of viscosity, we approached the issue of proteins confined within nanoscopic water cavities inside sol-gel glasses. Unlike proteins encapsulated in trehalose glasses, the majority of the fast structural dynamics sensed by the heme-bound CO ligands in aqueous solution continue to be active for MbCO and HbCO in the sol-gel glasses. The experimental results and MD simulations support an environment in which the silica pore walls confine a nanoscopic layer of water around the protein, which in turn affects the dynamics of the encapsulated protein. Although the solvent confinement is less extreme in the sol-gel pores (i.e. the layer of water is thicker) than in trehalose glasses, the mechanism of dynamic inhibition through a constrained layer of water is a feature common to both systems. The results may suggest a certain mechanistic generality for fine-tuning protein structural fluctuations through molecular crowding, and underscore the relevance of protein encapsulation in silica sol-gel glasses to the understanding of protein behavior in crowded physiological environments. In this regard, it is an important and challenging goal for future studies to characterize and understand the effect of varying thicknesses of confined solvent on protein structure and dynamics.

4.8 REFERENCES

- (1) Halling, P. J. *Curr. Opin. Chem. Biol.* **2000**, *4*, 74.
- (2) Klibanov, A. M. *Nature* **2001**, *409*, 241.
- (3) Das, T. K.; Khan, I.; Rousseau, D. L.; Friedman, J. M. *Journal of the American Chemical Society* **1998**, *120*, 10268.
- (4) Khan, I.; Shannon, C. F.; Dantsker, D.; Friedman, A. J.; Perez-Gonzalez-de-Apodaca, J.; Friedman, J. M. *Biochemistry* **2000**, *39*, 16099.
- (5) Yamanaka, S. A.; Nishida, F.; Ellerby, L. M.; Nishida, C. R.; Dunn, B.; Valentine, J. S.; Zink, J. I. *Chem. Mater.* **1992**, *4*, 495.
- (6) Martinek, K.; Levashov, A. V.; Klyachko, N.; Khmel'nitski, Y. L.; Berezin, I. V. *Eur. J. Biochem.* **1986**, *155*, 453.
- (7) Vitkup, D.; Ringe, D.; Petsko, G. A.; Karplus, M. *Nature Struct. Bio.* **2000**, *7*, 34.
- (8) Fenimore, P. W.; Frauenfelder, H.; McMahon, B. H.; Young, R. D. *Proc. Natl. Acad. Sci. USA* **2004**, *101*, 14408.
- (9) Crowe, J. H.; Crowe, L. M. *Nature Biotechnology* **2000**, *18*, 145.
- (10) Kilburn, D.; Townrow, S.; Meunier, V.; Richardson, R.; Alam, A.; Ubbink, J. *Nature Materials* **2006**, *5*, 632.
- (11) Crowe, J. H.; Crowe, L. M. *Science* **1984**, *223*, 701.
- (12) Sola-Penna, M.; Meyer-Fernandez, J. R. *Arch. Biochem. Biophys.* **1998**, *360*, 10.
- (13) Carpenter, J. F.; Crowe, J. H. *Biochemistry* **1989**, *28*, 3916.
- (14) Ballone, P.; Marchi, M.; Branca, C.; Magazu, S. *J. Phys. Chem. B* **2000**, *104*, 6313.
- (15) Belton, P. S.; Gil, A. M. *Biopolymers* **1994**, *34*, 957.
- (16) Cottone, G.; Ciccotti, G.; Cordone, L. *J. Chem. Phys.* **2002**, *117*, 9862.
- (17) Walser, R.; Gunsteren, W. F. *Proteins: Structure, Function, and Genetics* **2001**, *42*, 414.
- (18) Caliskan, G.; Mechtani, D.; Roh, J. H.; Kisliuk, A.; Sokolov, A. P.; Azzam, S.; Cicerone, M. T.; Lin-Gibson, S.; Peral, I. *J. Chem. Phys.* **2004**, *121*, 1978.
- (19) Chen, T.; Fowler, A.; Toner, M. *Cryobiology* **2000**, *40*, 277.
- (20) Cottone, G.; Giuffrida, S.; Ciccotti, G.; Cordone, L. *Proteins: Structure, Function, and Bioinformatics* **2005**, *59*, 291.
- (21) Bren, K. L.; Gray, H. B.; Banci, L.; Bertini, I.; Turano, P. *J. Am. Chem. Soc.* **1995**, *117*, 8067.
- (22) Massari, A. M.; Finkelstein, I. J.; McClain, B. L.; Goj, A.; Wen, X.; Bren, K. L.; Loring, R. F.; Fayer, M. D. *J. Am. Chem. Soc.* **2005**, *127*, 14279.
- (23) Bren, K. L.; Kellogg, J. A.; Kaur, R.; Wen, X. *Inorganic Chemistry* **2004**, *43*, 7934.
- (24) Rector, K. D.; Rella, C. W.; Kwok, A. S.; Hill, J. R.; Sligar, S. G.; Chien, E. Y. P.; Dlott, D. D.; Fayer, M. D. *J. Phys. Chem. B.* **1997**, *101*, 1468.
- (25) Brinker, C. J.; Scherer, G. W. *Sol-gel Science: The Physics and Chemistry of Sol-gel Processing*; Academic Press: San Diego, 1990.

- (26) Ellerby, L. M.; Nishida, C. R.; Nishida, F.; Yamanaka, S. A.; Dunn, B.; Valentine, J. S.; Zink, J. I. *Science* **1992**, *255*, 1113.
- (27) Gill, I. *Chem. Mater.* **2001**, *13*, 3404.
- (28) Jin, W.; Brennan, J. D. *Analytica Chimica Acta* **2002**, *461*, 1.
- (29) Miller, J. M.; Dunn, B.; Valentine, J. S.; Zink, J. I. *J. Non-Cryst. Sol.* **1996**, *202*, 279.
- (30) Lloyd, C. R.; Eyring, E. M. *Langmuir* **2000**, *16*, 9092.
- (31) Dunn, B.; Miller, J. M.; Dave, B. C.; Valentine, J. S.; Zink, J. I. *Acta Materialia* **1998**, *46*, 737.
- (32) Williams, A. K.; Hupp, J. T. *Journal of the American Chemical Society* **1998**, *120*, 4366.
- (33) Ping, G.; Yuan, J. M.; Sun, Z. F.; Wei, Y. *J. Molec. Recog.* **2004**, *17*, 433.
- (34) Lan, E. H.; Dave, B. C.; Fukuto, J. M.; Dunn, B.; Zink, J. I.; Valentine, J. S. *J. Mater. Chem.* **1999**, *9*, 45.
- (35) Bruno, S.; Bonaccio, M.; Bettati, S.; Rivetti, C.; Viappiani, C.; Abbruzzetti, S.; Mozzarelli, A. *Protein Science* **2001**, *10*, 2401.
- (36) Eggers, D. K.; Valentine, J. S. *Protein Science* **2001**, *10*, 250.
- (37) Bettati, S.; Mozzarelli, A. *Journal of Biological Chemistry* **1997**, *272*, 32050.
- (38) Shibayama, N. *Journal of Molecular Biology* **1999**, *285*, 1383.
- (39) McIninch, J. K.; Kantrowitz, E. R. *Biochim. Biophys. Acta - Prot. Struct. Molec. Enzym.* **2001**, *1547*, 320.
- (40) Samuni, U.; Dantsker, D.; Khan, I.; Friedman, A. J.; Peterson, E.; Friedman, J. M. *Journal of Biological Chemistry* **2002**, *277*, 25783.
- (41) Viappiani, C.; Bettati, S.; Bruno, S.; Ronda, L.; Abbruzzetti, S.; Mozzarelli, A.; Eaton, W. A. *Proceedings of the National Academy of Sciences of the United States of America* **2004**, *101*, 14414.
- (42) Abbruzzetti, S.; Viappiani, C.; Bruno, S.; Mozzarelli, A. *Chem. Phys. Lett.* **2001**, *346*, 430.
- (43) Samuni, U.; Juszczak, L.; Dantsker, D.; Khan, I.; Friedman, A. J.; Perez-Gonzalez-De-Apodaca, J.; Bruno, S.; Hui, H. L.; Colby, J. E.; Karasik, E.; Kwiatkowski, L. D.; Mozzarelli, A.; Noble, R.; Friedman, J. M. *Biochemistry* **2003**, *42*, 8272.
- (44) Schiro, G.; Cammarata, M.; Levantino, M.; Cupane, A. *Biophys. Chem.* **2005**, *114*, 27.
- (45) Winter, R.; Hua, D. W.; Song, X.; Mantulin, W.; Jonas, J. *Journal of Physical Chemistry* **1990**, *94*, 2706.
- (46) Librizzi, F.; Viappiani, C.; Abbruzzetti, S.; Cordone, L. *J. Chem. Phys.* **2002**, *116*, 1193.
- (47) Berg, M. A.; Rector, K. D.; Fayer, M. D. *J. Chem. Phys.* **2000**, *113*, 3233.
- (48) Kubo, R. A stochastic theory of line-shape and relaxation. In *Fluctuation, Relaxation and Resonance in Magnetic Systems*; Ter Haar, D., Ed.; Oliver and Boyd: London, 1961.
- (49) Kubo, R. In *Fluctuation, Relaxation, and Resonance in Magnetic Systems*; Haar, D. T., Ed.; Oliver and Boyd: London, 1962.
- (50) Schmidt, J.; Sundlass, N.; Skinner, J. *Chem. Phys. Lett.* **2003**, *378*, 559.

- (51) Mayer, E. *J. Am. Chem. Soc.* **1994**, *116*, 10571.
- (52) Jorgensen, W. L.; Chandrasekhar, J.; Madura, J. D.; Impey, R. W.; Klein, M. L. *J. Chem. Phys.* **1983**, *79*, 926.
- (53) Elber, R.; Roitberg, A.; Simmerling, C.; Goldstein, R.; Li, H.; Verkhivker, G.; Keaser, C.; Zhang, J.; Ulitsky, A. *Comput. Phys. Commun.* **1994**, *91*, 159.
- (54) Merchant, K. A.; Noid, W. G.; Akiyama, R.; Finkelstein, I.; Goun, A.; McClain, B. L.; Loring, R. F.; Fayer, M. D. *J. Am. Chem. Soc.* **2003**, *125*, 13804.
- (55) Finkelstein, I. J.; Goj, A.; McClain, B. L.; Massari, A. M.; Merchant, K. A.; Loring, R. F.; Fayer, M. D. *J. Phys. Chem. B* **2005**, *109*, 16959.
- (56) Merchant, K. A.; Noid, W. G.; Thompson, D. E.; Akiyama, R.; Loring, R. F.; Fayer, M. D. *J. Phys. Chem. B* **2003**, *107*, 4.
- (57) Potter, W. T.; Hazzard, J. H.; Kawanishi, S.; Caughey, W. S. *Biochem. Biophys. Res. Comm.* **1983**, *116*, 719.
- (58) Hong, M. K.; Braunstein, D.; Cowen, B. R.; Frauenfelder, H.; Iben, I. E. T.; Mourant, J. R.; Ormos, P.; Scholl, R.; Schulte, A.; Steinbach, P. J.; Xie, A.; Young, R. D. *Biophys. J.* **1990**, *58*, 429.
- (59) Young, R. D.; Frauenfelder, H.; Johnson, J. B.; Lamb, D. C.; Nienhaus, G. U.; Philipp, R.; Scholl, R. *Chem. Phys.* **1991**, *158*, 315.
- (60) Rector, K. D.; Jiang, J.; Berg, M.; Fayer, M. D. *J. Phys. Chem. B* **2001**, *105*, 1081.
- (61) Rector, K. D.; Engholm, J. R.; Rella, C. W.; Hill, J. R.; Dlott, D. D.; Fayer, M. D. *J. Phys. Chem. A* **1999**, *103*, 2381.
- (62) Eichler, H. J. *Laser-Induced Dynamic Gratings*; Springer-Verlag: Berlin, 1986.
- (63) Fourkas, J. T.; Fayer, M. D. *Accounts of Chemical Research* **1992**, *25*, 227.
- (64) Dlott, D. D.; Fayer, M. D.; Hill, J. R.; Rella, C. W.; Suslick, K. S.; Ziegler, C. J. *J. Am. Chem. Soc.* **1996**, *118*, 7853.
- (65) Owrutsky, J. C.; Li, M.; Locke, B.; Hochstrasser, R. M. *J. Phys. Chem.* **1995**, *99*, 4842.
- (66) Mukamel, S. *Principles of Nonlinear Optical Spectroscopy*; Oxford University Press: New York, 1995.
- (67) Angell, C. A.; Ngai, K. L.; McKenna, G. B.; McMillan, P. F.; Martin, S. W. *J. Appl. Phys.* **2000**, *88*, 3113.
- (68) Green, J. L.; Fan, J.; Angell, C. A. *J. Phys. Chem.* **1994**, *98*, 13780.
- (69) Ngai, K. L.; Paluch, M. *J. Chem. Phys.* **2004**, *120*, 857.
- (70) Fenimore, P. W.; Frauenfelder, H.; McMahan, B. H.; Parak, F. G. *Proc. Natl. Acad. Sci. USA* **2002**, *99*, 16047.
- (71) Tarek, M.; Tobias, D. J. *Phys. Rev. Lett* **2002**, *88*, Art. No. 138101.
- (72) Cordone, L.; Galajda, P.; Vitrano, E.; Gassman, A.; Ostermann, A.; Parak, F. *Eur. Biophys. J.* **1998**, *27*, 173.
- (73) Cottone, G.; Cordone, L.; Ciccotti, G. *Biophysical Journal* **2001**, *80*, 931.
- (74) McClain, B. L.; Finkelstein, I. J.; Fayer, M. D. *J. Am. Chem. Soc.* **2004**, *126*, 15702.
- (75) Müller, J. D.; McMahan, B. H.; Chen, E. Y. T.; Sligar, S. G.; Nienhaus, G. U. *Biophys. J.* **1999**, *77*, 1036.

- (76) Andrews, B. K.; Romo, T.; Clarage, J. B.; Pettitt, B. M.; Phillips, G. N., Jr. *Structure* **1998**, *6*, 587.
- (77) Potter, W. T.; Hazzard, J. H.; Choc, M. G.; Tucker, M. P.; Caughey, W. S. *Biochemistry* **1990**, *29*, 6283.
- (78) Gottfried, D. S.; Peterson, E. S.; Sheikh, A. G.; Wang, J. Q.; Yang, M.; Friedman, J. M. *Journal of Physical Chemistry* **1996**, *100*, 12034.
- (79) Rector, K. D.; Thompson, D. E.; Merchant, K.; Fayer, M. D. *Chem. Phys. Lett.* **2000**, *316*, 122.
- (80) Fayer, M. D. *Ann. Rev. Phys. Chem.* **2001**, *52*, 315.
- (81) Piryatinski, A.; Skinner, J. L. *J. Phys. Chem. B* **2002**, *106*, 8055.
- (82) Joo, T. H.; Jia, Y. W.; Yu, J. Y.; Lang, M. J.; Fleming, G. R. *J. Chem. Phys.* **1996**, *104*, 6089.
- (83) Massari, A. M.; Finkelstein, I. J.; Fayer, M. D. *J. Am. Chem. Soc.* **2006**, *128*, 3990.
- (84) Walsh, C. A.; Berg, M.; Narasimhan, L. R.; Fayer, M. D. *Chem. Phys. Lett.* **1986**, *130*, 6.
- (85) Berg, M.; Walsh, C. A.; Narasimhan, L. R.; Littau, K. A.; Fayer, M. D. *J. Chem. Phys.* **1988**, *88*, 1564.
- (86) Bai, Y. S.; Fayer, M. D. *Phys. Rev. B* **1989**, *39*, 11066.
- (87) Berg, M. A.; Hubble, H. W. *Chem. Phys.* **1998**, *233*, 257.
- (88) Rella, C. W.; Rector, K. D.; Kwok, A. S.; Hill, J. R.; Schwettman, H. A.; Dlott, D. D.; Fayer, M. D. *J. Phys. Chem.* **1996**, *100*, 15620.
- (89) Williams, R. B.; Loring, R. F.; Fayer, M. D. *J. Phys. Chem. B* **2001**, *105*, 4068.
- (90) Zwanzig, R.; Mountain, R. D. *Journal of Chemical Physics* **1965**, *43*, 4464.
- (91) Merchant, K. A.; Thompson, D. E.; Xu, Q.-H.; Williams, R. B.; Loring, R. F.; Fayer, M. D. *Biophys. J.* **2002**, *82*, 3277.
- (92) Wasiucionek, M.; Breiter, M. W. *J. Non-Cryst. Sol.* **1997**, *220*, 52.
- (93) Lenza, R. F. S.; Vasconcelos, W. L. *J. Non-Cryst. Sol.* **2000**, *273*, 164.
- (94) Tan, H.-S.; Piletic, I. R.; Fayer, M. D. *J. Chem. Phys.* **2005**, *122*, 174501.
- (95) Tan, H.-S.; Piletic, I. R.; Riter, R. E.; Levinger, N. E.; Fayer, M. D. *Phys. Rev. Lett.* **2005**, *94*, 057405.
- (96) Piletic, I. R.; Tan, H.-S.; Fayer, M. D. *J. Phys. Chem. B* **2005**, *109*, 21273.
- (97) Gottfried, D. S.; Kagan, A.; Hoffman, B. M.; Friedman, J. M. *J. Phys. Chem. B* **1999**, *103*, 2803.
- (98) Sottini, S.; Viappiani, C.; Ronda, L.; Bettati, S.; Mozzarelli, A. *J. Phys. Chem. B* **2004**, *108*, 8475.
- (99) Debye, P. J. W. *Polar molecules*; Dover Publications: New York, 1945.
- (100) Kohn, J. E.; Millett, I. S.; Jacob, J.; Zagrovic, B.; Dillon, T. M.; Cingel, N.; Dothager, R. S.; Seifert, S.; Thiyagarajan, P.; Sosnick, T. R.; Hasan, M. Z.; Pande, V. S.; Ruczinski, I.; Doniach, S.; Plaxco, K. W. *Proceedings of the National Academy of Sciences of the United States of America* **2004**, *101*, 12491.
- (101) Uzawa, T.; Akiyama, S.; Kimura, T.; Takahashi, S.; Ishimori, K.; Morishima, I.; Fujisawa, T. *Proceedings of the National Academy of Sciences of the United States of America* **2004**, *101*, 1171.

- (102) Baker, D. *Nature* **2000**, 405, 39.
- (103) Konishi, Y.; Feng, R. *Biochemistry* **1994**, 33, 9706.
- (104) Flora, K. K.; Brennan, J. D. *Chem. Mater.* **2001**, 13, 4170.
- (105) Gonnelli, M.; Strambini, G. B. *Biophys. Chem.* **2003**, 104, 155.
- (106) Goj, A.; Loring, R. F. *Submitted* **2007**.
- (107) Finkelstein, I. J.; McClain, B. L.; Fayer, M. D. *J. Chem. Phys.* **2004**, 121, 877.
- (108) Hasinoff, B. B. *Biophys. Chem.* **1981**, 13, 173.
- (109) Lew, V. L.; Raftos, J. E.; Sorette, M.; Bookchin, R. M.; Mohandas, N. *Blood* **1995**, 86, 334.
- (110) Wegner, G.; Kucera, W. *Biomed. BioChim. Acta* **1989**, 48, 561.
- (111) Franco, R. S.; Barker, R. L. *J. Lab. Clin. Med.* **1989**, 113, 58.
- (112) Kelemen, C.; Chien, S.; Artmann, G. M. *Biophys. J.* **2001**, 80, 2622.
- (113) Hochmuth, R. M.; Buxbaum, K. L.; Evans, E. A. *Biophys. J.* **1980**, 29, 177.
- (114) Kelemen, C., Hemoglobin Concentrations.
- (115) Mooney, M. *J. Colloid Sci.* **1951**, 6, 162.
- (116) Einstein, A. *Investigations on the Theory of Brownian Movement*; Dover: New York, 1956.
- (117) Rector, K. D.; Kwok, A. S.; Ferrante, C.; Tokmakoff, A.; Rella, C. W.; Fayer, M. D. *J. Chem. Phys.* **1997**, 106, 10027.
- (118) Merchant, K. A.; Thompson, D. E.; Fayer, M. D. *Phys. Rev. Lett.* **2001**, 86, 3899.
- (119) Merchant, K. A.; Thompson, D. E.; Fayer, M. D. *Phys. Rev. A* **2002**, 65, 023817.

CHAPTER 5: PROTEIN-SUBSTRATE INTERACTIONS

5.1 INTRODUCTION

Enzyme-substrate binding is a dynamic process that is intimately coupled to protein structural fluctuations.^{1,2} High-throughput screening methods have identified enzymes that bind structurally diverse inhibitors within their active sites, often with binding affinities exceeding those of the biologically derived substrate.^{3,4} Such experimental observations illuminate our understanding of protein-substrate interactions, underscoring that static protein structure information alone is insufficient to describe the diverse influences of ligand binding at an active site.^{2,5} A complete description of protein-ligand interactions requires information on the modification of protein dynamics, if any, when a ligand binds. In addition to increasing our understanding of how enzymes function, a thorough description of the relationship between protein dynamics and substrate binding will improve ligand docking algorithms and may ultimately lead to discoveries of novel classes of drugs and inhibitors for biomedical protein targets.

Proteins are rapidly interconverting within an ensemble of similar conformations.⁶⁻¹¹ A subset of these rapidly interconverting states may be favorable for binding a given substrate. A different subset of conformations may accommodate a structurally heterologous ligand. Although conceptually appealing, this mechanism is difficult to probe experimentally as it requires sensitivity to protein structural dynamics on fast timescales. The questions addressed here are whether substrate binding influences protein dynamics and whether different substrates binding to the same protein produce distinct changes in protein dynamics?

In this work, we employ 2D-IR vibrational echo spectroscopy to examine the equilibrium structural fluctuations of horseradish peroxidase (HRP) in the absence and presence of small molecule substrates with dissociation constants spanning three orders of magnitude. HRP is a type III peroxidase family glycoprotein that oxidizes a variety of organic molecules in the presence of hydrogen peroxide as the oxidizing

agent.¹² HRP has proven to be amenable to protein engineering and has been of intense interest in bio-industrial and enantiospecific catalysis applications.^{4,13,14}

The active site of HRP is comprised of a solvent exposed iron heme prosthetic group that participates in the enzymatic catalysis cycle.^{4,14} The heme can bind carbon monoxide (CO), which has been frequently exploited as an site specific reporter of protein structure^{9,15-18} and dynamics.^{9,19-21} The time dependence of the CO transition frequency is a spectroscopic reporter of protein structural fluctuations.^{9,18,21} Within the dynamic Stark effect model, structural fluctuations of groups within the protein generate a time-dependent electric field at the heme active site.^{9,18,21} The CO transition frequency is exquisitely sensitive to electric fields.^{17,20,22} Therefore, CO frequency fluctuations are sensitive to global as well as local protein structural evolution.

The small molecule substrates used in this study are benzhydroxamic acid analogs that have been investigated as a general class of tightly binding inhibitors for HRP and other peroxidases^{4,23} (see Figure 5.1). A wealth of structural,²⁴⁻²⁷ biochemical,^{13,14,28,29} and spectroscopic evidence^{19,20,30,31} has identified His42 and Arg38 as the key HRP residues in modulating substrate binding and enzymatic activity. These distal heme residues are highly conserved in the peroxidase family.⁴ Substrates and intermediates in the catalytic reaction of HRP interact with the distal residues via an extensive hydrogen bonding network within the active site (see figure 2).^{24,32} Substrates such as benzhydroxamic acid can participate strongly with this intrinsic hydrogen bond network, showing the strongest binding affinities. The substrates selected for this study incorporate key structural modifications that tune their propensity for making hydrogen bonds within the active site and modulate the dissociation constants from ferric HRP between $K_d = 4300 - 0.16 \mu\text{M}$.¹⁴

Aqueous HRP in the free form (without substrate) adopts two distinct spectroscopic states and, as shown below, has structural dynamics on the < 1 ps and 20 ps timescales. Upon substrate binding, HRP occupies a single structural state. The protein dynamics, as reported by the CO transition frequency fluctuations measured with the 2D-IR experiments, decrease in amplitude and slow down significantly. The

protein dynamics of HRP are compared to myoglobin-CO (MbCO) and a mutant H64V (the distal histidine is replaced by valine) that exhibits a similar reduction in observed dynamics relative to MbCO. The results are used to comment on the possible role of the biologically derived substrates in reordering the protein active site to facilitate downstream events in the enzymatic pathway.

5.2 MATERIALS AND METHODS

Horseshoe peroxidase type VIA (isoenzyme C) and horse heart myoglobin were purchased as lyophilized powder from Sigma-Aldrich. Benzhydrazide (BZH), benzhydroxamic acid (BHA), benzamide (BZA), N-methylbenzamide (NMBZA), and D₂O were purchased from Aldrich. All reagents were of the highest available quality and used without further purification. 2-Naphthohydroxamic (2-NHA) acid was synthesized according to published protocols²³, re-crystallized twice, and deemed pure by ¹H-NMR. CO forms of HRP and Mb were prepared according to previously published protocols.⁹ Typical absorption at the peak of the CO stretch band was ~0.1 absorbance units above the protein and D₂O background, which is typically ~0.4.

5.3 DYNAMICS OF HRP IN THE FREE AND SUBSTRATE-BOUND STATES

5.3.1 *Linear Spectra*

The background subtracted and normalized linear absorption spectra of free and inhibitor-bound HRP-CO in D₂O are presented in Figure 5.1. At pD 7.4, free HRP occupies two spectroscopically distinct structural conformations, with CO absorption bands centered at 1903 cm⁻¹ and 1934 cm⁻¹ (Figure 5.1a).^{33,34} The x-ray crystal structure of HRP-CO shows an extensive hydrogen bond network at the active site that incorporates the CO, His42, Arg38, and a disordered water molecule in the heme cavity (see Figure 5.2).²⁴ Resonance Raman spectra of the distal histidine imidazolium³⁵ and other experimental data³⁴ suggest that in the red state the CO is nearly normal to the heme plane and oriented such that it has a strong interaction with the distal histidine and a weaker one with the distal arginine. In the blue state, the Fe-C-O linkage, although linear, is somewhat bent relative to the heme normal, allowing

the CO to have a strong interaction with the distal arginine and a weaker one with the distal histidine. Resonance Raman evidence indicates that the crystal structure of the heme pocket shown in Figure 5.2 resembles the blue spectroscopic state.³⁵ This structural assignment of the blue state is reinforced by pH titration studies of HRP. Deprotonation of His42 at pH = 8.7 is correlated with a total disappearance of the red state in HRP, indicating that CO in red state participates in hydrogen bonding with a hydrogen on the distal histidine.³⁵

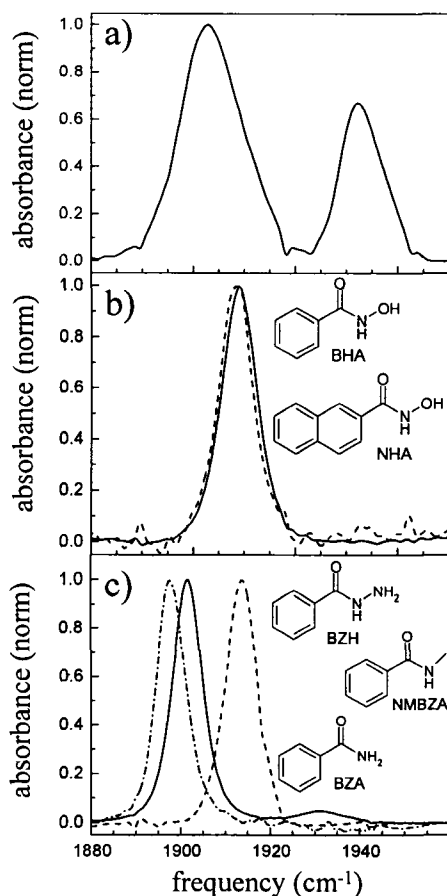


Figure 5.1 Normalized FT-IR spectra of the CO stretching mode bound to HRP in the (a) free form and when complexed to (b) 2-NHA (dashed), BHA (solid) (c) NMBZA (dashed), BZA (dash-dot) and BZH (solid). Structures and abbreviations of the horseradish peroxidase substrates used in this study are shown in the appropriate panels.

Figure 5.1b shows the background subtracted linear spectra of HRP ligated with BHA (solid curve) and 2-NHA (dashed curve). Figure 5.1c displays the linear spectra of HRP-NMBZA, HRP-BZA, and HRP-BZH complexes. Upon substrate

binding, the CO band becomes a single, essentially Gaussian peak centered between 1898-1915 cm^{-1} .^{33,34} The ligated HRP spectra are spread around the frequency of the unligated HRP red state and are significantly lower in frequency than the blue unligated state. The CO band peak positions and widths are summarized in Table 5.1. A change in the transition frequency of the type observed here is almost certainly caused by a rearrangement of the distal cavity structure.^{9,17,20} For example, in MbCO it is well documented that the three spectroscopically distinct substates, A₀, A₁, and A₃ arise from distinct configurations of the distal histidine.^{9,36}

	$\nu_{\text{CO}} (\text{cm}^{-1})$	FWHM (cm^{-1})
HRP blue	1932.7	9.0
HRP red	1903.7	13
2-NHA	1908.3	7.3
BHA	1909	7.3
BZH	1913.3	9.0
NMBZA	1898	6.9
BZA	1901.5	8.6

Table 5.1 Linear spectra of free and substrate bound HRP.

Substrate binding in HRP is enthalpically stabilized, largely by the strong substrate carbonyl-Arg38 hydrogen bond.¹⁴ The HRP mutant R38L does not bind BHA.³⁷ BHA and 2-NHA are well matched to form hydrogen bonds with Arg38, His42, and Pro139, and have very high binding affinities ($K_d = 2.5$ and $0.16 \mu\text{M}$, respectively) to the ferric protein.^{14,32} The substrates BZA, NMBZA, and BZH are less well suited to making hydrogen bonds within the active site and have dissociation constants of $K_d = 4300, 360, 110 \mu\text{M}$, respectively.

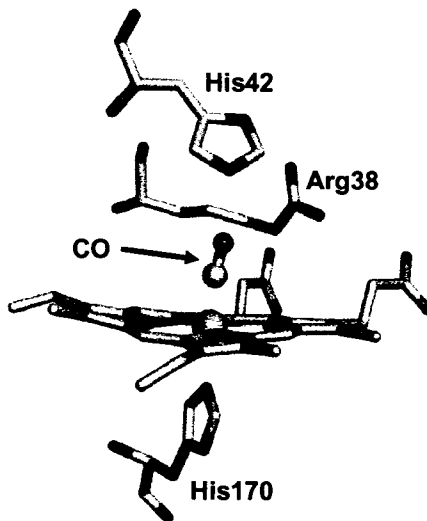


Figure 5.2 Crystal structure of the active site of free HRP taken from the Protein Data Bank (1W4Y). His170 tethers the heme group in the active site. The residues Arg38, His42 and a disordered water molecule define the distal active site structure and hydrogen bonding network. Possible hydrogen bonding interactions are shown as dashed green lines.

5.3.2 2D-IR Spectroscopy

The absorption frequencies of substrate bound-HRP do not report the time dependent protein structural fluctuations.²⁰ 2D-IR vibrational echo spectroscopy provides a dynamic spectrum that is sensitive to structural fluctuations of HRP and can be used to investigate how these dynamics are influenced by the binding of different substrates. Vibrational correlation spectra of HRP in the free form for a series of increasing T_w are presented in Figure 5.3 as contour plots with 10% intervals. (The data have much finer contours used in analysis.) The ω_r frequency axis is associated with the first interaction with the radiation field (first IR pulse), and the ω_m frequency axis is associated with the third interaction with the radiation field (third IR pulse), which is the emission frequency of the vibrational echo pulse. Two positive bands (red) along the diagonal at $(\omega_r, \omega_m) = (1903 \text{ cm}^{-1}, 1903 \text{ cm}^{-1})$ and $(1932 \text{ cm}^{-1}, 1932 \text{ cm}^{-1})$ arise from the 0 to 1 vibrational transitions of the CO stretch of the red and blue states of HRP, respectively. The negative peaks (blue) arise from the 1 to 2 transitions

and are displaced from the diagonal bands by a CO vibrational anharmonicity of ~ 25 cm^{-1} .³⁸ These negative going bands are directly below their corresponding positive going 0-1 bands. The dynamical information obtained from the 1-2 bands is the same as that obtained from the 0-1 bands, therefore only the 0-1 bands are analyzed below.

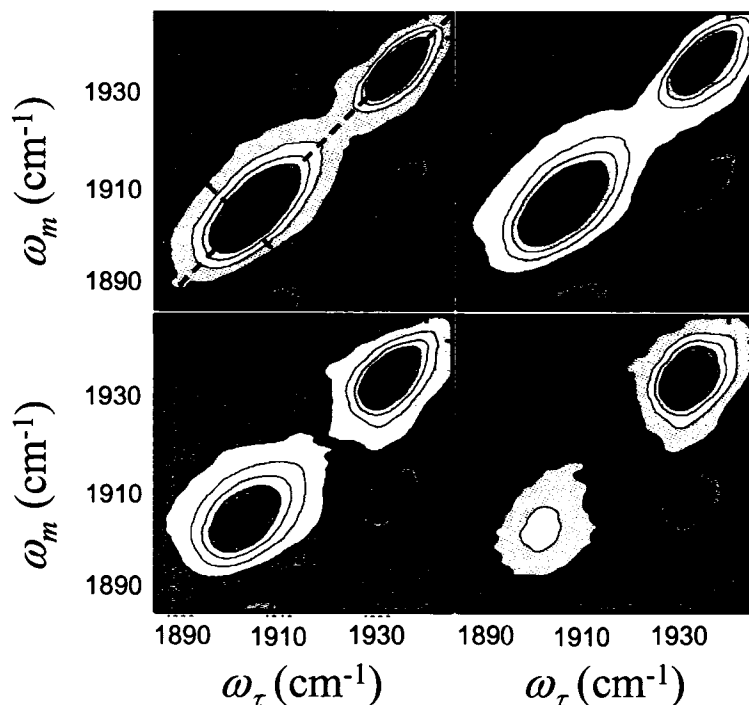


Figure 5.3 2D-IR spectra of free HRP as a function of increasing T_w . Each contour corresponds to a 10% signal change. The red peaks report on ground state dynamics and blue peaks display excited state dynamics. The dashed lines illustrate the diagonal and anti-diagonal slices through the data for calculating the eccentricity parameter. See the text for further details.

As can be seen in Figure 5.3, both the relative amplitudes and the shapes of the 0-1 bands (bands on the diagonal) change with increasing T_w . At early T_w , the amplitudes of the two states are determined by the strengths of their transition dipole moments and concentrations. Vibrational energy relaxation to the ground vibrational state reduces the amplitudes of both bands at longer T_w s. IR pump-probe experiments were used to measure the vibrational lifetimes of the red and blue states, which were determined to be 8 ps and 12 ps, respectively. Therefore, although the red state has a higher equilibrium concentration, the band at $(\omega_b, \omega_m) = (1903 \text{ cm}^{-1}, 1903 \text{ cm}^{-1})$

decays significantly faster than the blue band and the ratio of the peak amplitudes changes with increasing T_w .

The change in shape of the bands as T_w is increased reflects protein structural dynamics. The vibrational echo pulse sequence used to collect 2D-IR spectra displays inhomogeneous broadening along the diagonal and dynamic broadening along the anti-diagonal (shown as dashed lines in Figure 5.3).³⁹ At short T_w the 2D dynamic line shape has significant inhomogeneous broadening, which manifests itself as elongation along the diagonal. As T_w is increased, the experiment picks up longer time scale protein dynamics that increases the anti-diagonal width and decreases the diagonal width, but to a lesser extent than the anti-diagonal. In the long time limit, all protein fluctuations contribute to the 2D spectrum, which would lead to a 2D-IR shape with equal diagonal and anti-diagonal linewidths.

The eccentricity (see Chapter 2) is a convenient way to succinctly summarize protein dynamics contained in the 2D-IR spectra. The eccentricity, ε , is defined as $\varepsilon(T_w) = \sqrt{1 - \sigma_{AD}^2(T_w) / \sigma_D^2(T_w)}$, where σ_{AD} and σ_D are the band widths along the anti-diagonal and diagonal slices, respectively (see dashed lines in the upper left panel of Figure 5.3). This definition for the eccentricity displays several convenient limits. In the case of large inhomogeneous broadening, $\sigma_{AD} \ll \sigma_D$, and $\varepsilon \rightarrow 1$. At longer T_w s, slower timescale protein dynamics contribute to the anti-diagonal width, causing the eccentricity to decay to zero. In the long time limit in which all protein structures have been sampled, $\varepsilon \rightarrow 0$. The full 2D spectral shapes are used in fitting the data.

The T_w dependent eccentricities of free and substrate-bound HRP are presented in Figure 5.4. Curves through the data are obtained from 2D-IR calculations employing a dynamic Stark effect model of protein dynamics that is described below. In Figure 5.4a, the eccentricities of the red and blue spectroscopic states of free HRP are shown as squares and circles, respectively. Both states have nearly identical initial eccentricities, indicating a similar ratio of dynamic to inhomogeneous broadening at very short T_w . The eccentricity of the red state decays faster than of the blue state, and reaches ~ 0.5 at the longest experimentally accessible T_w . Neither the red state nor the

blue states have sampled all structural configurations on the time scale of the experiment.

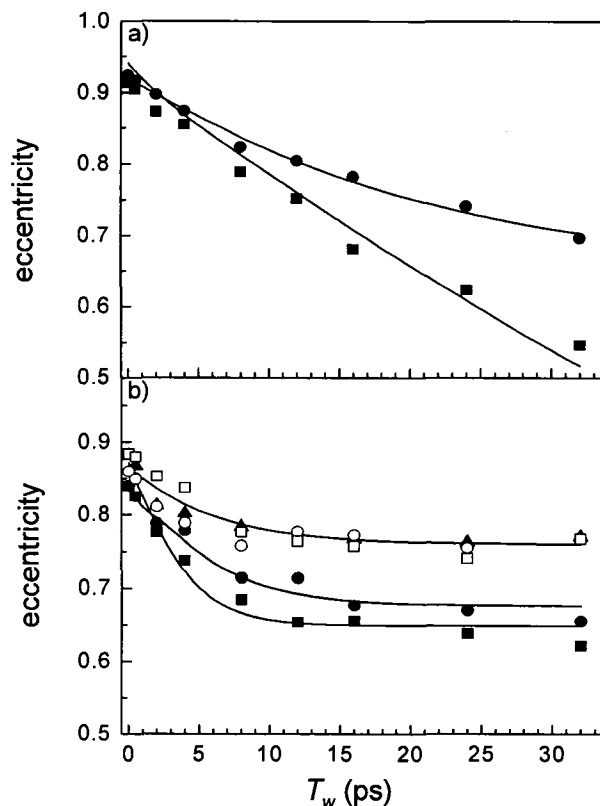


Figure 5.4 a) T_w dependent eccentricities of the blue (circles) and red (square) states of free HRP. b) Eccentricities of HRP ligated with 2-NHA (solid squares), BHA (solid circles), BZA (open squares), BZH (open circles) and NMBZA (triangles). The solid lines are derived from simultaneously fitting the linear and 2D-IR data to determine the FFCFs.

Figure 5.4b presents the T_w -dependent eccentricities of HRP complexed with the five substrates. Introducing the substrate into the protein active site fundamentally changes the nature of the dynamics as is evident in the qualitative differences between the T_w dependent eccentricities in Figure 5.4a and Figure 5.4b. Substrate binding shifts dynamics to longer time scales. With a bound substrate, the eccentricity decays on the timescale of a few picoseconds at early T_w s, but plateaus after $T_w = \sim 10$ ps, becoming nearly T_w independent. In the cases of BHA and 2-NHA bound to HRP, the eccentricities may continue to decrease, but on timescales that are very slow particularly compared to the free HRP red state. Dynamics in HRP complexed with

NMBZA are significantly constrained, and the eccentricity stops changing at a relatively large value of ~ 0.75 . A large T_w independent eccentricity indicates that a significant fraction of the total CO line width undergoes frequency fluctuations on timescales that are much slower than the experimental observation window. Figure 5.4 demonstrates qualitatively that substrate binding to HRP significantly slows the short time scale structural dynamics of the protein and shifts a significant fraction of the fluctuations to much longer time scales.

5.3.3 Underlying Protein Dynamics

A quantitative description of the amplitudes and timescales of CO frequency fluctuations is provided by the frequency-frequency correlation function (FFCF).^{9,18,21} Within standard approximations, both the linear absorption spectrum and the 2D-IR vibrational echo spectra at all T_w are simultaneously described by the FFCF.⁴⁰ A multi-exponential form of the FFCF, $C(t)$, conveniently organizes a distribution of protein fluctuation time scales and has been found to reproduce the influence of structural dynamics on the CO frequency in other heme proteins.^{8,9,41} A bi-exponential plus a constant FFCF, $C(t) = \Delta_1^2 e^{-t/\tau_1} + \Delta_2^2 e^{-t/\tau_2} + \Delta_3^2$, was sufficient to describe most of the observed protein dynamics in HRP. The static component in $C(t)$, Δ_3 , is the contribution to the CO frequency distribution that occurs from protein structures that interconvert slower than the observable experimental timescales. The 2D-IR experiment is sensitive to dynamics that occur out to several T_w ,⁴² which corresponds to ~ 100 ps in the experiments presented below. Structural fluctuations slower than ~ 100 ps appear static to the experiment and are described by Δ_3 . The Δ_3 term can be viewed as multiplied by another exponential but as far as the experiment is concerned in all but one case discussed below, $\tau_3 = \infty$. Δ_i is the amplitude of frequency fluctuations (in units of angular frequency) resulting from structural evolution with a characteristic time τ_i . For $\Delta_i^{-1}\tau_i \ll 1$ for a given exponential term, this component of the FFCF is motionally narrowed.^{41,43} A motionally narrowed term in $C(t)$ contributes a T_w independent symmetric 2D Lorentzian line with a width

$\Gamma^* = \pi \Delta^2 \tau$ to the total 2D-IR spectrum. For a motionally narrowed component, Δ and τ cannot be determined independently, but rather Γ^* can be obtained. The fastest protein fluctuations can contribute a motionally narrowed exponential to the FFCF and arise from very fast local motions of small groups, analogous to low frequency vibrations, that do not significantly modify the enzyme topology. These fluctuations have been observed in experiments and simulations of several similar heme-CO protein (see Chapter 4).^{8,41}

FFCFs were extracted from the experimental data via an iterative fitting algorithm. The FFCF obtained from analysis of the data using response theory calculations⁴⁰ was deemed correct when it could be used to simultaneously calculate 2D-IR spectra that accurately reproduced the experimental correlation plots at all T_w , the linear absorption spectrum, and the T_w dependence of the eccentricity parameter. In all cases, the data and calculations were in excellent agreement. Notably, the dynamics of the red state of free HRP could not be adequately modeled by a bi-exponential FFCF. The static term in the FFCF was replaced with a third exponential that has a 21 ps⁻¹ time constant.

The parameters defining the experimentally derived FFCFs for free HRP and HRP with the five substrates bound are presented in Table 5.2. Each of the FFCFs has a motionally narrowed component characterized by the Lorentzian line width (Γ^*) that contributes to the total 2D-IR linewidth but does not contribute to the T_w dependence. The FFCF of the red state of free HRP is different from all of the other spectroscopic lines. In addition to the motionally narrowed component, two additional timescales, $\tau_2 = 1.5$ ps and $\tau_3 = 21$ ps, are observed for the red state. This τ_3 is the decay time constant in the exponential factor that formally multiplies the Δ_3^2 term but is not shown because τ_3 is infinite for all of the other systems. The results indicate that the full range of structures that give rise to the red state absorption spectrum have been sampled by ~ 100 ps. The blue state of free HRP is well described by a single 15 ps exponential, but lacks a short timescale component (aside from the motionally narrowed term that is common to all of the systems). In the blue state a relatively

large set of CO frequency fluctuations occur on timescales slower than ~ 100 ps⁴² and necessitate a static term in the FFCF ($\tau_3 = \infty$).

	Γ^* (cm ⁻¹)	Δ_2 (cm ⁻¹)	τ_2 (ps)	Δ_3 (cm ⁻¹)	τ_3 (ps)
HRP blue	1.4	3.2	15	2.4	∞
HRP red	0.76	3.1	1.5	5.6	21
2-NHA	0.62	3.2	2.6	1.8	∞
BHA	1.4	2.3	4.4	1.9	∞
BZA	1.4	2.8	4.5	2.7	∞
BZH	1.6	2.6	2.6	2.7	∞
NMBZA	1.3	1.7	5.4	2.0	∞

Table 5.2 FFCFs derived from linear and 2D-IR experimental data.

In comparing the behavior of free vs. substrate bound HRP, the question arises as to the nature of the structural fluctuations that give rise to the observed dynamics. The influence of BHA binding on HRP-CO dynamics has been studied by Kaposi and co-workers both experimentally and via MD simulations.^{16,20} The two spectroscopic states of free HRP were modeled by changing the protonation state of the distal histidine. In the protonated state (taken to be the red peak in the simulations), Arg38 was relatively far from the CO and exhibited large RMSD fluctuations. In the deprotonated case (blue state), Arg38 was significantly closer to the CO. Introducing BHA into the active site re-oriented Arg38 towards the substrate, shortened the Arg38-CO distance slightly, and reduced the RMSD fluctuations of both the distal histidine and arginine.

Our results are in good qualitative agreement with the simulations. It is clear from the FFCF parameters given in Table 5.2 that the dynamics of HRP with a bound substrate are very different than the red state of free HRP. The free blue state and red state have a 15 ps and 21 ps component, respectively. In contrast, the FFCFs for HRP with bound substrates have a slowest component of ~ 2 ps to ~ 5 ps in the observation time window. The linear absorption spectra of HRP with bound substrates are more similar to the red state of free HRP than to the blue state. The red state 1.5 ps fast component is followed by a slow component of 21 ps that takes the FFCF essentially to zero by ~ 100 ps, completing the dynamics. None of the HRP-substrate systems

show a component of their FFCFs that reflects full structural sampling by 100 ps. All of the HRP-substrate systems have substantial structural dynamics too slow to be in the experimentally accessible window, which are manifested as the constant term in the FFCF (see Table 5.2). In comparison to the red state of free HRP, substrate binding significantly reduces the protein fluctuations. The red state 1.5 ps component becomes two or three times as long and the 21 ps component becomes too slow to measure. When the protein binds a substrate, the active site structure exhibits a single spectroscopic state in which fluctuations of the distal arginine are strongly constrained. The small fraction of the dynamics that occur within the experimental window for HRP-substrate systems indicates that the dynamics of the distal histidine are also severely constrained. Our results are consistent with the suggestion that loss of dynamic freedom by Arg38 is responsible for much of the entropic loss upon substrate binding.¹⁴

Further insights into the changes in HRP dynamics upon ligand binding can be obtained by comparison to MbCO. The active site of HRP is relatively large, can bind a diverse array of substrate molecules, and contains a distal histidine and arginine. The active site of myoglobin cannot accommodate substrates and does not have a distal arginine, but it also contains a distal histidine and a heme that binds CO. A wealth of experiments and simulations has underscored the pivotal role of the distal histidine in modulating the CO frequency in myoglobin. The H64V mutant (the distal histidine is replaced by a non-polar valine) displays significantly decreased vibrational dephasing because of the elimination of this polar group.^{9,18} It is instructive to compare the dynamics of free HRP to that of wild-type myoglobin and substrate-bound HRP with H64V.

The eccentricities of wild type horse heart MbCO (squares) and H64V (circles) are presented in Figure 5.5 as a function of T_w . MbCO can adopt three distinct spectroscopic states that arise from different structural configurations of the distal histidine relative to the CO.^{9,15} The data shown in Figure 5.5 is for the A_1 band of MbCO, the main band in the absorption spectrum. In the A_1 state, it has been shown that the distal histidine does not form a hydrogen bond with the CO.⁹ The

eccentricities of H64V are obtained from an FFCF derived from previous homodyne vibrational echo experiments.¹⁸ The lines are fits to the HRP-NMBZA (top curve) and free HRP (lower curve) experimental eccentricities that were discussed above but have been offset along the vertical axis to account for different initial values of the HRP and myoglobin data (different motionally narrowed components). It is apparent from Figure 5.5 that despite differences in the structure and function of HRP and Mb, the proteins display qualitatively similar trends in how the CO frequency is modulated by protein structural fluctuations. The dynamics of the red state of free HRP are very similar to those of the wild type MbCO and are still evolving even at the longest experimentally accessible timescales. Introducing NMBZA into the active site of HRP reduces the rate and amplitude of protein dynamics in a fashion analogous to that of removing the distal histidine in MbCO.

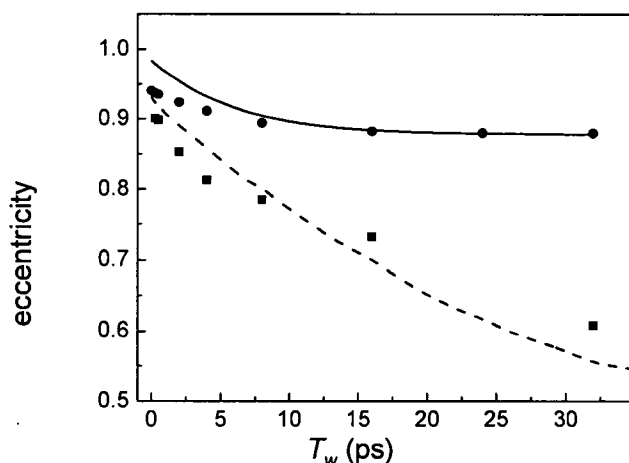


Figure 5.5 The eccentricities of the A1 state of wild type MbCO (squares) and the mutant H64V (circles). The curves are calculated eccentricities of HRP-NMBZA (top curve) and red state free-HRP (lower curve), offset to overlap with the myoglobin data.

In H64V, the distal histidine has been removed, and the rate and magnitude of the vibrational dephasing on the experimental time scales are reduced accordingly. Based on the similarity between the MbCO data and the HRP red state data shown in Figure 5.5, it is reasonable to assume that a substantial contribution to the vibrational dephasing comes from the fluctuations of the distal histidine and the distal arginine. The 2D-IR experiment is sensitive to time-dependent electric fields around the CO, so the striking similarity in HRP-substrate and H64V dynamics highlights that substrate

binding in HRP renders the distal residues nearly static on the 2D-IR experimental timescale. The clear conclusion to be drawn is that substrate binding locks up the distal ligands, constraining the structural fluctuations in the active site. The result is that the time scale of the fluctuations is pushed out to long times (> 100ps).

5.4 CONCLUDING REMARKS

The 2D-IR vibrational echo experiments demonstrate that unligated HRP has a dynamically “loose” red state in which motions of the distal ligands contribute substantially to vibrational dephasing. Upon substrate binding, both the amplitudes and timescales of CO frequency fluctuations decrease markedly.

It is striking that the protein dynamics are significantly *decreased* when additional potential sources of CO frequency perturbations are introduced into the active site. The distal residues participate in every step of the enzymatic cycle of HRP and the results presented here indicate that substrate binding reorganizes and dynamically constrains these residues. Based on the observation that substrates in the HRP active site significantly decreases structural fluctuations of the distal residues, we suggest that the protein may exploit this feature of substrate binding to catalyze further steps in the enzymatic pathway. Thus, upon recognition of biologically occurring substrates, the protein active site is not only reorganized structurally but also dynamically, priming the enzyme to sample the portion of the conformational energy landscape that may lead to subsequent steps in the reaction. In the enzymatic cycle of HRP, substrate binding occurs after H₂O₂ enters the active site and binds at the heme. The distal histidine serves as a general proton source and the distal arginine stabilizes reactive intermediates.⁴ Thus, both residues must be favorably positioned to facilitate downstream events in the enzymatic cycle, a process that may be afforded by the dynamic quenching observed upon substrate binding.²⁰

5.5 REFERENCES

- (1) Jimenez, R.; Salazar, G.; Yin, J.; Joo, T.; Romesberg, F. E. *Proc. Natl. Acad. Sci. USA* **2004**, *101*, 3803.
- (2) Ma, B.; Shatsky, M.; Wolfson, H. J.; Nussinov, R. *Protein Sci.* **2002**, *11*, 184.
- (3) Vazquez-Laslop, N.; Zheleznova, E. E.; Markham, P. N.; Brennan, R. G.; Neyfakh, A. A. *Biochem. Soc. Trans.* **2000**, *28*, 517.
- (4) Veitch, N. C.; Smith, A. T. *Adv. Inorg. Chem.* **2000**, *51*, 107.
- (5) Halperin, I.; Ma, B.; Wolfson, H.; Nussinov, R. *Proteins* **2002**, *47*, 409.
- (6) Fenimore, P. W.; Frauenfelder, H.; McMahon, B. H.; Parak, F. G. *Proc. Natl. Acad. Sci. USA* **2002**, *99*, 16047.
- (7) Frauenfelder, H.; McMahon, B. H.; Austin, R. H.; Chu, K.; Groves, J. T. *Proc. Natl. Acad. Sci. USA* **2001**, *98*, 2370.
- (8) Massari, A. M.; Finkelstein, I. J.; Fayer, M. D. *J. Am. Chem. Soc.* **2006**, *128*, 3990.
- (9) Merchant, K. A.; Noid, W. G.; Akiyama, R.; Finkelstein, I.; Goun, A.; McClain, B. L.; Loring, R. F.; Fayer, M. D. *J. Am. Chem. Soc.* **2003**, *125*, 13804.
- (10) Mukherjee, P.; Kass, I.; Arkin, I. T.; Zanni, M. T. *Proc. Natl. Acad. Sci. USA* **2006**, *103*, 3528.
- (11) Chung, H. S.; Khalil, M.; Smith, A. W.; Ganim, Z.; Tokmakoff, A. *Proc. Natl. Acad. Sci. USA* **2005**, *102*, 612.
- (12) Veitch, N. C. *Phytochemistry* **2004**, *65*, 249.
- (13) Smith, A. T.; Veitch, N. C. *Curr. Opin. Chem. Biol.* **1998**, *2*, 269.
- (14) Aitken, S. M.; Turnbull, J. L.; Percival, M. D.; English, A. M. *Biochemistry* **2001**, *40*, 13980.
- (15) Spiro, T. G.; Wasbotten, I. H. *J. Inorg. Biochem.* **2005**, *99*, 34.
- (16) Kaposi, A. D.; Vanderkooi, J. M.; Stavrov, S. S. *Biophys. J.* **2006**, *91*, 4191.
- (17) Dalosto, S. D.; Prabhu, N. V.; Vanderkooi, J. M.; Sharp, K. A. *J. Phys. Chem. B* **2003**, *107*, 1884.
- (18) Finkelstein, I. J.; Goj, A.; McClain, B. L.; Massari, A. M.; Merchant, K. A.; Loring, R. F.; Fayer, M. D. *J. Phys. Chem. B* **2005**, *109*, 16959.
- (19) Khajepour, M.; Troxler, T.; Vanderkooi, J. M. *Biochemistry* **2003**, *42*, 2672.
- (20) Kaposi, A. D.; Prabhu, N. V.; Dalosto, S. D.; Sharp, K. A.; Wright, W. W.; Stavrov, S. S.; Vanderkooi, J. M. *Biophys. Chem.* **2003**, *106*, 1.
- (21) Williams, R. B.; Loring, R. F.; Fayer, M. D. *J. Phys. Chem. B* **2001**, *105*, 4068.
- (22) Park, E.; Andrews, S.; Boxer, S. G. *J. Phys. Chem.* **1999**, *103*, 9813.
- (23) Summers, J. B.; Mazdiyasni, H.; Holms, J. H.; Ratajczyk, J. D.; Dyer, R. D.; Carter, G. W. *J. Med. Chem.* **1987**, *30*, 574.
- (24) Carlsson, G. H.; Nicholls, P.; Svistunenko, D.; Berglund, G. I.; Hajdu, J. *Biochemistry* **2005**, *44*, 635.
- (25) Meno, K.; Jennings, S.; Smith, A. T.; Henriksen, A.; Gajhede, M. *Acta Crystallogr. D* **2002**, *58*, 1803.
- (26) Gajhede, M.; Schuller, D. J.; Henriksen, A.; Smith, A. T.; Poulos, T. L. *Nat. Struct. Biol.* **1997**, *4*, 1032.

- (27) Henriksen, A.; Gajhede, M.; Baker, P.; Smith, A. T.; Burke, J. F. *Acta Crystallogr. D* **1995**, *51*, 121.
- (28) Howes, B. D.; Heering, H. A.; Roberts, T. O.; Schneider-Belhadadd, F.; Smith, A. T.; Smulevich, G. *Biopolymers* **2001**, *62*, 261.
- (29) Howes, B. D.; Rodriguez-Lopez, J. N.; Smith, A. T.; Smulevich, G. *Biochemistry* **1997**, *36*, 1532.
- (30) Smulevich, G.; Feis, A.; Indiani, C.; Becucci, M.; Marzocchi, M. P. *J. Biol. Inorg. Chem.* **1999**, *4*, 39.
- (31) Kaposi, A. D.; Fidy, J.; Manas, E. S.; Vanderkooi, J. M.; Wright, W. W. *Biochim. Biophys. Acta* **1999**, *1435*, 41.
- (32) Henriksen, A.; Schuller, D. J.; Meno, K.; Welinder, K. G.; Smith, A. T.; Gajhede, M. *Biochemistry* **1998**, *37*, 8054.
- (33) Holzbaur, I. E.; English, A. M.; Ismail, A. A. *J. Am. Chem. Soc.* **1996**, *118*, 3354.
- (34) Ingledew, W. J.; Rich, P. R. *Biochem. Soc. Trans.* **2005**, *33*, 886.
- (35) Hashimoto, S.; Takeuchi, H. *Biochemistry* **2006**, *45*, 9660.
- (36) Johnson, J. B.; Lamb, D. C.; Frauenfelder, H.; Müller, J. D.; McMahon, B.; Nienhaus, G. U.; Young, R. D. *Biophys. J.* **1996**, *71*, 1563.
- (37) Smulevich, G.; Paoli, M.; Burke, J. F.; Sanders, S. A.; Thorneley, R. N.; Smith, A. T. *Biochemistry* **1994**, *33*, 7398.
- (38) Rector, K. D.; Kwok, A. S.; Ferrante, C.; Tokmakoff, A.; Rella, C. W.; Fayer, M. D. *J. Chem. Phys.* **1997**, *106*, 10027.
- (39) Roberts, S. T.; Loparo, J. J.; Tokmakoff, A. *J. Chem. Phys.* **2006**, *125*, 084502.
- (40) Mukamel, S. *Principles of Nonlinear Optical Spectroscopy*; Oxford University Press: New York, 1995.
- (41) Massari, A. M.; Finkelstein, I. J.; McClain, B. L.; Goj, A.; Wen, X.; Bren, K. L.; Loring, R. F.; Fayer, M. D. *J. Am. Chem. Soc.* **2005**, *127*, 14279.
- (42) Bai, Y. S.; Fayer, M. D. *Phys. Rev. B.* **1989**, *39*, 11066.
- (43) Schmidt, J.; Sundlass, N.; Skinner, J. *Chem. Phys. Lett.* **2003**, *378*, 559.